THE CAPTURE OF MAGNETIC INELASTIC DARK MATTER IN THE SUN.

THE CAPTURE OF MAGNETIC INELASTIC DARK MATTER IN THE SUN.

By

MATTHEW MCCREADIE, MPhys

A Thesis
Submitted to the School of Graduate Studies
in Partial Fulfillment of the Requirements
for the Degree
Master of Science

McMaster University

MASTER OF SCIENCE (2012)
(Physics)

McMaster University
Hamilton, Ontario

TITLE: The Capture Of Magnetic Inelastic Dark Matter In The Sun.

AUTHOR: Matthew McCreadie, MPhys (Cardiff University)

SUPERVISOR: Itay Yavin

NUMBER OF PAGES: x, 94

Abstract

We consider the phenomenology of the Magnetic Inelastic Dark Matter model, specifically its capture and subsequent annihilation in the Sun. By using the most recent data from the IceCube and Super-Kamiokande neutrino detection experiments, we are able to put limits on the dipole moment of this WIMP candidate for masses ranging from 100 GeV to 10 TeV with a mass-splitting ranging from 0 to 200 keV. Limits are placed on a 100 GeV WIMP with magnetic dipole interactions as low as $2.6 \times 10^{-6} \mu_N$ for an inelastic parameter of 100 keV.

Contents

List of Figures

Chapter 1

Introduction

The nature of dark matter is one of the most intriguing mysteries in physics. One of our best candidates to explain its properties is the WIMP, or Weakly Interacting Massive Particle. These particles would be produced by thermal processes in the early universe, and freeze-out at their present density as the universe cooled. They are posited to have interactions at approximately the weak scale and masses ranging from a few eV to hundreds of TeV or beyond.

So far our attempts to probe the nature of these WIMPs beyond their gravitational properties have provided, at best, conflicting hints as to their mass and interactions. In an attempt to reconcile these hints with the strong bounds place on dark datter particles by experiment, many models have been suggested. Of these models, Magnetic Inelastic Dark Matter is among the most appealing. It has a strong theoretical motivation[68], an appealing simple form[23], and is able to explain more than one of the clues seen by experimenters into the nature of Dark Matter[23, 72].

If we are ever going to detect Dark Matter through anything other than its gravitational effects, it must have some coupling to the Standard Model. If it couples to $U(1)$, that is, electromagnetism, there is a heirarchy of operators through which it can do so. As charged dark matter is ruled out down to a very small millicharge, and monopoles are also very strongly ruled out[24] the next viable operator is a magnetic dipole. This can easily arise in models where the WIMP is coupled to some heavier particle which couples to $U(1)$[72]. In these models, it is easy to generate two dark matter states, one with a higher mass than the other. The dipole operator is naturally off-diagonal, meaning that it mediates between two states. In this case, it will mediate between the two mass states. If this is the only operator governing the interaction, the coupling with electromagentism is therefore exclusively inelastic.

Given such a coupling, it is inevitable that when these particles pass through the Sun some of them scatter. In this scattering process they lose energy, and some will become gravitationally bound to the Sun[63]. After this process has occured, the particles continue to scatter, losing energy each time, until the lose sufficient energy to be in thermal equilibrium with the nuclei in the Sun. At

this stage, all the dark matter will be located within the 'thermal radius' of the Sun. After sufficient time, enough dark matter will be concentrated within this thermal radius for annihilation to occur.

In this work, we attempt to constrain this model by examining this process of capture in the Sun, subsequent annihilation and the detection of its annihilation products via the neutrino detectors Super-Kamiokande and IceCube. We find that we can put very strong bounds on this type of Dark Matter in a somewhat model independent way.

Chapter 2 of this work presents a brief review of the evidence for Dark Matter, what we know of its properties and how it can be detected before introducing the motivation for Magnetic Inelastic Dark Matter. Chapter 3 discusses the properties of dipole Dark Matter, how such an interaction might arise and how it might give rise to inelastic scattering. Chapter 4 deals with the idea of WIMP capture in the Sun in general and in the inelastic case specifically and Chapter 5 deals with the interactions that allow such capture to occur. Chapter 6 deals with the specifics of nuclear scattering, namely form factors, and how they effect capture. Chapter 7 presents the putative annihilation channels through which we might detect WIMPs in the Sun. Chapters 8,9 and 10 discuss the specifics of the calculation, with Chapter 8 covering the uncertainties present in such a calculation, Chapter 9 presenting the properties of the detectors being considered and the calculations necessary to get from a capture rate to an observable quantity and Chapter 10 quoting the results obtained.

Chapter 2

Dark Matter

2.1 Evidence for Dark Matter

Dark Matter is one of the most fascinating and biggest problems in physics today. The evidence for it comes from sources as wide ranging as individual galaxies to the microwave background of the entire universe. The ongoing search for evidence of its composition utilizes cutting edge physics and technology. This chapter will briefly cover the evidence for dark matter and what this tells us about its composition, before moving on to discuss a specific model for dark matter in the next section.

2.1.1 The Coma Cluster

In 1933, the first evidence of Dark Matter was seen by a Swiss astronomer named F. Zwicky . Zwicky studied a cluster of ∼100 bright galaxies known as the Coma Cluster located 99 Mpc from the Sun. By observing the galaxies' doppler shift, he was able to calculate the velocity dispersion of eight of the galaxies within the cluster [79] [76] [32] . He then applied the virial theorem to these galaxies, in order to discover the cluster mass. The virial theorem states that, in equilibrium, the average kinetic energy is equal to one half of the total potential energy ($\langle T\rangle = \frac{1}{2}\langle U\rangle$). If one assumes that the only interaction present is the gravity, the virial theorem becomes a relation between average velocity and mass. In this way, Zwicky calculated that the total mass of the cluster was $M_{cluster} \approx 4.5 \times 10^{13} M_{\odot}$ This was a very surprising result, as observational astronomy using standard light-to-mass ratios put the mass of the cluster at less than 2% of this value.[76] Even taking into account the mass of the unkown (at the time) intracluster gas, there was a large amount of mass that was, for some reason, non-luminous. He coined the term 'dark matter' to describe this non-luminous mass.

2.1.2 Galactic Rotation Curves

Despite other cluster observations by (among others) Smith (1936) and some work on galactic rotation by Babcock (1939) [77] it was almost four decades for Zwicky's 'Dark Matter' to be fully confirmed by external observations. In 1970, Vera Rubin and W. Kent Ford, Jr. published a survey of 67 objects in the Andromeda galaxy [65]. They studied the orbital velocities of these objects as a function of the distance from the galactic center. By balancing the centripetal force with the force of gravity, the orbital velocity becomes an important probe of the galactic mass profile. The rotational velocity of the consituents of a galaxy at a radius r from the galactic center is given by

$$\frac{v(r)^2}{r} = G\frac{M(r)}{r^2}, \tag{2.1}$$

where v is the rotational velocity at a distance r from the galactic center, $M(r)$ is the mass contained within a sphere of radius r and G is the gravitational constant.

If the mass distribution followed the light distribution, that is, almost entirely concentrated within a central region called the galactic bulge, the rotational velocity would fall off like $\frac{1}{\sqrt{r}}$ outside this region. However, Rubin found that this was not the case. Rather, she found that the velocities remained constant with increasing distance from the galactic center. This implies that mass of the galaxy is not concentrated in the galactic center, but instead increases linearly with distance. Once again, we see mass present without any light. In order to explain this observation, a sphere of invisible matter was hypothesized and the 'dark matter halo' concept was born. A dark matter halo is a sphere of dark matter surrounding a galaxy, centered on the galactic center. This hypothetical object explains the broad features of the astronomical evidence for dark matter, and so will be used as a working model throughout this thesis.

2.1.3 Further evidence from astronomy

General relativity predicts that matter bends light. Large concentrations of mass can therefore focus light, much like a lens. This 'gravitational lensing' can be used to reconstruct the concentration of dark matter which lies between Earth and a distant light source (for example a bright galaxy). This technique has been used to map dark matter distributions, most notably the Bullet Cluster [35].

In 2006 a group of researchers from Arizona, Sanford, Florida and Cambridge studied the two primary galaxy clusters of the Bullet Cluster, which had previously collided with each other at very high velocity. Clowe et al. observed the resulting x-ray emissions and by calculating the gravitational lensing, showed that both clusters had the predicted spherical dark matter halos, whose mass outweighed the luminous matter in the cluster by a factor of ~ 50[35].

They were also able to show that the gas which permeates both clusters lagged behind the main galaxies, showing that it was slowed by collisions during the merger. The dark matter was not

slowed in this way, and so must not interact with matter (both dark and baryonic) very strongly. This observation is an important one for putting constraints on the properties of dark matter. Not only do we know it exists, but we can start to say things about what it is.

2.1.4 Cosmological evidence

Since 1948 [31] , scientists have known that early universe photons should leave behind background radiation detectable in the current epoch. This Cosmic Microwave Background (CMB) was discovered (by accident) in 1965 [60] by Penzias and Wilson. The anisotropies present in this background radiation are a powerful probe of the make-up of the universe. The anisotropies seen in the CMB can be used as a measure of the energy density of the early universe. Specifically the ratio of baryonic matter, non-baryonic dark matter and so-called 'dark energy'. The latest measurements from the Planck satellite reveal that 26.8% of the energy density of the early universe was dark matter, compared to only 4.9% baryonic matter [3]. This powerful result provides further evidence which suggests that the non-luminous matter seen as early as 1933 is non-baryonic in nature, and that it was present in the early universe.

2.2 Dark Matter Composition

While evidence for the existence of a non-luminous component has only increased over the years, its nature is still very much in question. While some questions have already been answered above, namely that dark-matter is primarily non-baryonic, that it does not interact very strongly, etc., there are still many questions to be discussed. Among the most important of these questions are whether dark matter is relativistic (hot) or non-relativistic (cold), whether it consists of a new fundamental particle, or of some composite objects. If it is some new particle, how does it interact with baryonic matter? Does it couple to some dark gauge fields like much of the rest of matter couple to gauge fields?

2.2.1 Hot v. Cold Dark Matter

One convenient way of discussing the potential properties of dark matter is to discuss two extreme cases: 'Hot' dark matter (HDM) and 'cold' dark matter (CDM). The first of these candidates consists of dark matter particles of a mass less than O(10)eV. These were "hot" in the early universe, in the sense that they were still in thermal equilibrium at the time of the QCD confinement condition, which occured when the temperature of the universe was $\sim 100 MeV$. These particles must, by virtue of special relativity, move at very high velocities (known as relativistic velocities) [64] . Cold dark matter, on the other hand, has considerably higher mass, and decouples much earlier than the heavier canditade. These particles move at considerably slower velocities. The most significant difference between these two candidates is their effect on the formation of structure in the early universe. Due

to its relativistic nature, any small scale structures present in the early universe would be quickly smoothed out as the low mass particles spread from their point of creation at relativistic velocities. On the other hand, cold dark matter can preserve such structures, and even condense new structures as the particles' gravitational interaction is strong enough relative to its velocity to notably effect its motion. Between these two extremes is "warm" dark matter, which is heavy enough to decouple before QCD confinement, but light enough that its motion still washes out structure significantly.

Models in which the majority or entirity of the dark matter population is hot or warm dark matter predict that super clusters form much sooner than is observed, and galaxies form much later than observed[64]. They also predict a level of anisotropy in the CMB not seen by either Planck or WMAP [41] . This rules out hot or warm dark matter as the dominant form of dark matter in the universe. Instead, we have a universe of either entirely cold dark matter, or a mixed universe which contains primarily cold dark matter with a small fraction of hot dark matter[12].

2.2.2 WIMPs v. MaCHOs

The introduction of an entirely new type of matter, one which has not been detected by any traditional means, is a big leap for physicists to take. In order to try to avoid this, and explain some of the astronomical observations of non-luminous matter, several scientists [16] suggested that the extra mass was in the form of massive compact halo objects (so-called MaCHOs). These would be baryonic in nature and consist of stellar or planetary masses that are not sufficiently dense to ignite nuclear fusion, and hence are not burning.

The appeal of not having to resort to an undiscovered matter type to explain observations is obvious, and the initial excitement about this option grew in the early 1990s when microlensing techniques began identifying MaCHOs within the Milky Way [8]. However, it has since become clear that these objects do not contain sufficient mass to explain all the dark matter in our galaxy. In addition studies of the CMB put the fraction of non-baryonic matter in the universe at 26.8%, which provides further evidence of non-baryonic dark matter [39] .

Finally, there are some non-particle alternatives to the missing matter problem. Chief among these is Modified Newtonian Dynamics (MOND), a theory which consists of modifying Newtonian gravity to explain the observed rotation curves. Unfortunately, it is difficult to create a theory of this kind that matches generalized observations. Please see [9] and references therein for more information.

2.2.3 The WIMP miracle

The most widely studied class of candidates for this new kind of matter is known as a Weakly Interacting Massive Particle. This class is defined by two simple properties, firstly that it is 'massive', and hence non-relativistic, and secondly that it interacts with standard model particles with approximately the same strength as the weak interaction. The first of these properties is dictated by

the need for cold dark matter as discussed above. The masses studied range from ∼keV to ∼1000 TeV and beyond. The second property comes from the so-called 'WIMP miracle' which is discussed in this section.

In the early universe, any potential particulate dark matter candidate would be in thermal equilibrium with the surrounding baryonic matter. If this dark matter particle has an interaction with standard model particles, it would be constantly created and destroyed in interactions like figure 2.1. As the universe expands, the temperature drops, lowering the average energy of a particle. When

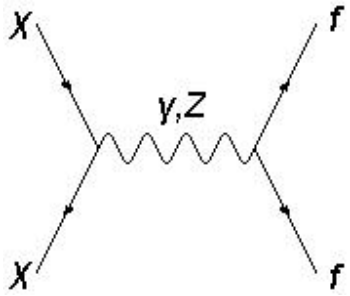

Figure 2.1: The annihilation of two dark matter particles via a photon or Z-boson to a fermion-antifermion pair.

the average energy of the standard model particles drops below the dark matter particles' mass very few dark matter particles will be created, as only those standard model particles at the upper end of the temperature distribution will have sufficient energy to generate them. However, dark matter will still be able to annihilate into lower mass standard model particles. At this point, the amount of dark matter begins to drop exponentially. As the number of dark matter particles decrease and the universe continues to expand, the likelihood of one dark matter particle encountering another one and annihilating decreases. It continues to decrease until the rate of expansion is higher than the rate of annihilation. At this point, the chance of an annihilation occuring is virtually zero meaning that the dark matter density is now fixed. This is known as 'freeze-out'[46].

The amount of dark matter left at freeze-out can be determined by solving the Boltzmann equation. The solution shows that the relic density, $\Omega_{DM} \propto \frac{1}{\langle \sigma v \rangle}$, where $\langle \sigma v \rangle$ is the thermally averaged cross section for two dark matter particles to annihilate into standard model particles. Here, Ω_{DM} is the density of dark matter in units of the critical density. It is given by $\Omega_{DM} = \frac{\rho_{DM}}{\rho_c}$ where ρ_{DM} is the energy density of dark matter and ρ_c is the "critical density", defined as the energy density for which the universe is geometrically flat. It is given by $\rho_c = \frac{3H^2}{8\pi G}$ where H is the Hubble constant and G is the gravitational constant[46]. It is here that the WIMP miracle appears. If one inserts the observed dark matter density into the above formula, the cross-section that it gives corresponds to that predicted for particles with electroweak scale interactions. Thus, a massive particle with weak scale interactions fits with all the observations so far catelogued. For this reason WIMPs are one of the most well-motivated dark matter candidates currently studied, and the one that this paper

focusses on [20].

2.3 The Methods and Status of Direct Detection Experiments

A particle which interacts with the standard model should be detectable, either directly through its interactions, or indirectly through the products of those interactions. The former case is known as direct detection, the latter indirect detection.

While direct detection experiments vary greatly in size and construction, the principal behind them is identical: given that WIMPs are present in the Solar System, and given that they have some (albeit small) interaction with matter, there is a non-zero chance of a WIMP scattering off a given nucleus. This nucleus will necessarily recoil, and detecting this recoil allows us to detect the WIMP and measure some of its properties. While this simple principle is the basis for all direct detection, the methods of maximizing the chances of interaction, and the methods of detecting the recoil vary from detector to detector. What follows is a brief review of the most prominent direct detection experiments, their set up and the current status of their results.

2.3.1 Detector types

A useful way of discussing the different detectors is to categorize them by their detection method, that is, the way they measure the nuclear recoil. Most detectors use at least two different detection methods in order to maximize their ability to distinguish signal from background.

When a nucleus recoils, it absorbs some energy. The nucleus must then dissipate the energy through the material in some other way. There are three main methods of energy dissipation: scintillation, ionization and phonon emission. Nuclei dissipate their energy through some combination of the above methods, depending on the material out of which the detector is constructed.

Categorizing the detectors in this field by their detection method gives a diagram as shown in figure 2.2. In order to give an overview of the field, we will give a brief review about the following detectors: CDMS, XENON, CoGeNT, and DAMA. Each of these experiments has contributed significantly to the field of direct detection, and some of them even claim to have made a detection. For a more complete review of the field, please see one of the several excellent reviews on the subject [54, 66, 6].

2.3.2 CDMS

The Cold Dark Matter Search (CDMS) experiment is a collaboration located in an underground mine in Minnesota. Its target is protected by 2090 meters water equivalent rock overburden. This

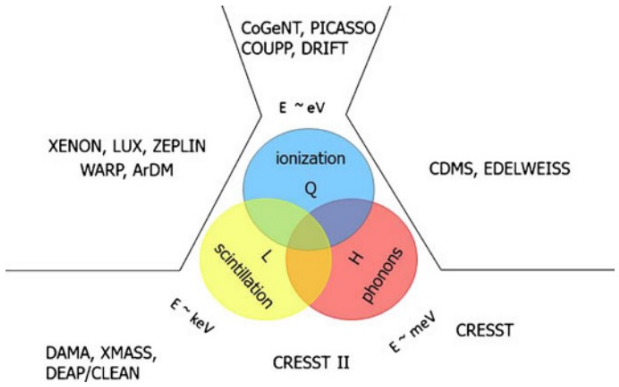

Figure 2.2: The three main direct detection methods and the experiments that utilize them. Figure from *Mahapatra, Pramana Journal Of Physics, 79, 5, 2012.*

means that in order for anything to scatter off the target material, it must first pass through the equivalent of ∼2000 meters of water. This is so that particles with a higher cross-section with regular matter (electrons for example) will be stopped in the rock and will not contribute to the background of the experiment.

The target material of the detector consists of 19 germanium and 11 silicon detectors which detect recoil events using simultaneous measurements of ionization and phonons. Ionization occurs when the scattering event causes the atom which participated in the event to lose an electron. When an electric field is passed across the detector, this electron, freed by the energy of the recoil, is accelerated towards electrodes placed at either end of the detector, giving a measurment of the ionization energy.

Phonons are quasiparticles which represent a quantized vibration in the detector material. They can be detected using thin-film superconductors, which can also give a measurment of the energy of the recoil. By combining these two measurements and comparing them, the CDMS collaboration can distinguish between nuclear recoil and electron recoil very accurately [5] . This, combined with the energy measurements from both sources, allow the collaboration to distinguish background events from WIMP scattering events.

In 2009, CDMS made a surprising announcement: two candidate events had been seen. In analysing their 2007-2008 data set they found two event records which showed characteristics consistent with those of WIMPs.[5] . As of writing, the two events do not have sufficient statistical significance to be labelled a discovery and, in fact, recent liklihood analysis indicate that these events are more likely to be leakage events than WIMP events, but we cannot completely discount them.

Even without taking these hints into account, CDMS has considerably constrained the parameter space in which WIMPs could exist, with most recent results placing strong constraints at the

90% certainty level for WIMP masses between 5-100 GeV. Their latest results [4] put an upper limit on the dark matter cross-section (the effective area available for scattering off nuclei) of $\sim 10^{-40}$ for WIMPs of mass 10 GeV.

2.3.3 XENON

XENON is located in the Gran Sasso mountain in central Italy. It consists of a liquid xenon core with 178 photomultiplier tubes at either end of the detector. It has a total detector mass of 34 kg. Similarly to CDMS, the XENON collaboration uses a combination of two detection methods to distinguish signal from background. Like CDMS, XENON uses the ratio between ionization and another signal to split electron from neutron recoil events. Unlike CDMS, the second detection method is that of scintillation. Scintillation occurs as part of the interaction process when an excited state of the Xenon relaxes into an unexcited state, emitting radiation. More details on this process can be found in [10].

In addition to allowing the collaboration to separate electron from nuclear recoil events, this experimental set up allows for the event to be reconstructed. This is acheived by measuring the amount of time between the initial scintillation signal (which arives directly following the event) and a second scintillation signal caused by the electron released in the ionizing process accelerating through the detector material. This allows determination of the location in one dimension, with the other two coordinates given by the pattern of detector hits. This means that cuts can be made which take into account the location of the event, for example, vetoing interactions which occur near the surface of the detector, as these are unlikely to be WIMP interactions.

XENON's advantage lies in the fact that both the ratio of ionization and scintillation signals and also their time separation allows for the discrimination of signal, and also liquid xenon's high mass and purity make it an excellent target material. It has had great success at limiting the WIMP-nucleon cross-section especially in the mass range between ∼20 and ∼1000 GeV. The current run of the experiment, known as XENON100, came online in 2008 with a target mass of 62 kg. In March 2013, they published the results of 225 days of data gathering. This dataset improved their cross-section limits by an order of magnitude, placing limits on $O(10)$ GeV dark matter cross-sections lower than 10^{-44} cm^2. XENON100 boasts the lowest background of any currently running Dark Matter experiment[11].

A similar experiment, LUX, began operation in April of 2013. It has a larger target mass than XENON100 with 250kg of actively monitored xenon. Despite only having released 85.3 days of data, they have acheived impressive results, improving limits greatly for WIMP masses between 10 and 100 GeV [14]. The results of this experiment can be seen below in figure 2.3.

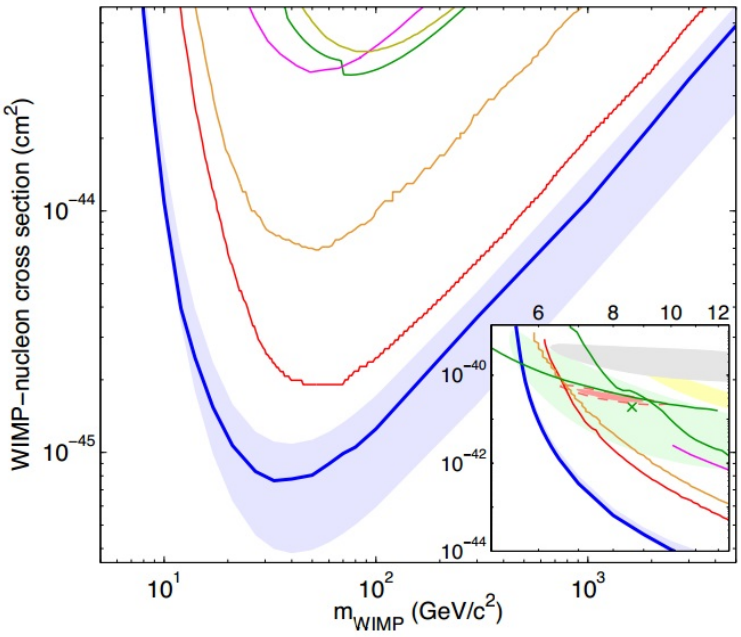

Figure 2.3: 90% C.L. limits placed on the WIMP cross-section by the following experiments: LUX (blue) with 1σ fluctuations shaded, EDELWEISS II (dark yellow), CDMSII (green), ZEPELIN-III (magenta), XENON100 (orange for 100 live days, red for 225 live days). The inset includes CDMSII (green) and regions of interest for DAMA/LIBRA (grey shaded) (see section 2.3.5 for more information), CoGeNT (red shaded), CDMSII silicon detectors (green shaded) and CRESST (yellow shaded). Figure from *LUX collaboration, arXiv: 1310.8214[14].*

2.3.4 CoGeNT

The CoGeNT detector, located just meters from CDMS in the same mine, only utilizes one form of detection. It's target material is high-purity germanium, and uses its ionization to detect scattering events. It uses pulse shape discrimination in order to distinguish nuclear from electron recoil. It also uses active sheilding in the form of a muon detector. An event which also triggers the muon detector is vetoed, as it is likely to be caused by the muon that was detected. A similar process is used to veto events whose data has been corrupted by incident photon scattering.

Although CoGeNT's vetos are not as powerful as XENON's or CDMS', meaning that their signal to background ratio is lower, CoGeNT has a lower threshold, making it sensitive to lower mass WIMPs, and allowing them to place excellent limits on dark matter particles with mass in the 5 - 10 GeV range.

In 2010, CoGeNT released a paper which claimed to see evidence of dark matter in the 7-11 GeV range. According to the collaborations, these events fit with the previous detection of two events at CDMS, a putative signal at CRESST and also the DAMA annual modulation signal (see the next section for discussion of this signal). However, these signals are far excluded by recent results from

XENON100 and LUX [1].

2.3.5 DAMA

Finally, we will discuss the DAMA/Libra experiment. This is unique among the experiments discussed here, in that it makes very little attempt to veto background events. Instead, they accept all scintillator data, and attempt to take advantage of the predicted temporal variation in WIMP events to isolate the signal. If we assume that the dark matter halo is non-rotating with respect to the galactic center, the Earth will have some motion relative to it at all times. Firstly, the Galactic Disk will be moving relative to the dark matter halo, causing an effective "WIMP wind" throughout the solar system. In addition to this, the Earth's motion around the Sun, and hence relative to the WIMP wind causes seasonal variations in the effective speed of the WIMP wind, and hence the liklihood of interaction. During the time when the Earth is travelling in the same direction as the WIMP wind, the flow of WIMPs is slower relative to the Earth, and therefore fewer WIMPs will pass through any detector, conversely, there should be more WIMP interactions during the time when the Earth is moving against the WIMP wind [66].

The DAMA collaboration seeks to exploit this fact by searching for annual modulations in their data. Since the early 2000s, DAMA has claimed to see such a modulation. Their most recent publications claim a certainty level of 9.3σ. One of the enduring mysteries in the current studies of Dark Matter is the presence of this modulation. While it is, itself, in good agreement with the predictions of many WIMP models, standard interactions that would produce this level of modulation are heavily ruled out by limits set by CDMS and XENON (among other experiments). Discovering the source of this discrepancy is one of the major motivations for working on non-standard models of Dark Matter [18].

2.4 Indirect Dark Matter Detection

While direct dark matter detection is a powerful tool in our search for dark matter, it is not our only one. In the Standard Model, each particle has an anti-matter equivalent. When the two meet, an annihilation occurs, producing energy in the form of new particles. If we assume, as above, that WIMPs interact with the Standard Model in some way, we are naturally led to the conclusion that at least some of their annihilations result in Standard Model products. As with the Standard Model particles, WIMP annihilations require a Dark Matter particle and its antimatter equivalent. Annihilations therefore require either that anti-WIMPs are present in equivalent numbers to WIMPs, or that WIMPs are their own anti-particles (that is, WIMPs are majorana particles). For this work we assume that the latter case is true. For more information on placing limits on asymmetric dark matter (dark matter who's anti-particle is absent), please see Petraki and Volkas' review on the subject [62].

Even with abundant Dark Matter anti-particles, such annihilations must be rare in the universe in general as Dark Matter is sparsely distributed. However, when WIMPs are highly concentrated, their annihilations become more frequent. If the annihilations are sufficiently frequent, the annihilation products may be detectable from Earth. The challenge then becomes finding a situation where dak matter is dense enough for this to occur. One of these places is the interior of a star [49]. This option is the main topic of this thesis.

Another option is the center of the galaxy. Here, dark matter should be sufficiently concentrated for annihilation products to be detectable, provided these products can reach Earth without being either intercepted or having their course altered such that pinpointing their origin is impossible. The best option for this kind of detection is photons[34] .

The FERMI large area telescope detects gamma rays across the entire sky. In recent years, much attention has been drawn to the discovery by Christoph Weniger in the FERMI/LAT's data of a 'line' eminating from the galactic center. This represents an excess of photons at an energy of 135 GeV. If we interpret this data as being a dark matter signal, it would represents the annihilation of two WIMPs of mass 135 GeV annihilating and producing two photons in opposite directions[73] . The status of this signal is uncertain though, as the FERMI collaboration points out a couple of worrying facts about this data. First, they note that the peak is not as smooth as would be expected from WIMP annihilation. Secondly, they point out several other features of similar significance at other energies and other places in the sky, which would tend to downplay the importance of this single feature[7] . More data will be needed in order to determine whether this feature is, in fact, a WIMP signal, if it is an instrumentation effect or if it is another phenomenon entirely.

The method of indirect detection is a powerful one. Firstly, it expands our reach beyond Earth-bound experiments, allowing us to look at places where Dark Matter is extremely highly concentrated for a signal. Secondly, it allows us to place constraints on the fundamental properties of WIMPs, their mass and their interactions with the Standard Model. However, many difficulties arise in practice. The locations where the annihilations are expected to be most frequent (the center of stars, the galactic center) have high matter densities, and many competing signals. The annihilation products of the dark matter will be altered and diffused on their way to the Earth, making detection a challenge. However, strong bounds have been put on WIMP annihilation by the Fermi/Lat collaboration, [33] by AMS-02 [47] , which looks for excesses in positron, anti-proton or gamma-ray fluxes and by neutrino searches directed at the Sun (see chapter 4 for more information).

2.5 Motivation for Magnetic Inelastic Dark Matter

As mentioned above, one of the greatest challenges in building a dark matter model today is reconciling the limits placed by CDMS and other direct detection experiments with the annual modulation seen my DAMA. The key to this problem is recognizing the crucial differences between

the experimental methods of the various collaborations. In examining the setups of each of the experiments we see that DAMA distinguishes itself from the other detectors in two important ways: Firstly, the target material of DAMA, iodine, is considerably heavier than that employed by CDMS (germanium). Secondly, iodine also posseses a large nuclear magnetic moment. This second fact suggests building models with dominantly magnetic interactions. The simplest of these models is the dipole interaction [23]. This model is outlined below.

The difference in mass suggests a different approach, one which alters the kinematics of the interaction. There are not many ways in which to do this, but one which has been suggested in the past to create two dark matter states, with a mass splitting between them. There are then two kinds of interaction, an inelastic one in which the WIMP scatters against the nucleus and some of the energy goes into creating this new, excited, state and a highly surpressed (or even forbidden) elastic interaction in which the new WIMP state is not present.

In the case where the elastic interaction is completely supressed, WIMPs can only scatter via an inelastic interaction. In order to undergo an inelastic transition, the incoming state must have sufficient center of mass energy to overcome the inelastic splitting, that is, the mass difference between the two states. The kinetic inergy in the center of mass frame depends on both the WIMP mass and the mass of the nucleus via the reduced mass of the system. A lower mass nucleus will lower the center of mass energy of the interaction, thus for low mass targets, there will not be sufficient energy to overcome the mass-splitting, and collision will not occur. Hence, a WIMP model with inelastic splittings favours high mass targets, and therefore has the possibility of reconciling DAMA's modulation with other collaborations' limits.

Chapter 3

Magnetic Dipole Interactions

As discussed above, dipole interactions are a simple, yet intriguing possibility for dark matter. In this section, we will define precisely what we mean when we refer to Magnetic Dipole Dark Matter, and how this model might arise.

3.1 Definition of Magnetic Dipole Interaction

Classically, a magnetic dipole is the second term in the multipole expansion of a magnetic field. The first term is the magnetic monopole term. Particles with magnetic monopoles were argued for by Dirac in 1931 and have been searched for ever since. Limits from cosmic rays and accelerators currently rule out magnetic monopoles lighter than $\sim$ 800 GeV [24] , and even at this mass, they could not be sufficiently numerous to account for all of Dark Matter.

The next term in the expansion is the magnetic dipole. It can be thought of as being caused by the seperation of the two poles of a magnet. As magnets in nature always come with equal sources and sinks, there is no overall magnetic charge. However, when these points are seperated in space, placing the object in a magnetic (or electric) field causes a torque on the object as the two poles of the magnet are pushed in different directions. Classical magnetic dipole moment is defined as a vector which points in the direction of the poles' separation.

$$\mathbf{m} = p\mathbf{r} \tag{3.1}$$

where p is the strength of the magnetic poles and $\mathbf{r}$ is a vector pointing in the direction of their separation, from the negative to the positive charge. The SI units for magnetic dipole moment are $J \cdot T^{-1}$.

In Quantum Field Theory, interactions between particles are described by "anharmonic" terms in the Lagrangian. These are term in the interacting fields that dictate the strength and nature of

the interaction. The magnetic dipole interaction appears in the Lagrangian through the term

$$\frac{1}{2}\bar{\chi}\mu_\chi\sigma^{\alpha\beta}F_{\alpha\beta}\chi. \tag{3.2}$$

The WIMPs are represented by the fields χ and $\bar{\chi}$ (note, for the inelastic case the second instance of the field ($\bar{\chi}$) must be the excited case) while the electromagnetic field, and hence the photon, is represented by $F_{\alpha\beta}$. More technically $F_{\alpha\beta}$ is called the electromagnetic tensor. It is a rank-2 tensor whose components are built from the electric and magnetic fields. The presence of the two WIMP fields and the electromagnetic tensor means that this term describes an interaction between two WIMPs and a photon. The other components of the term describe the nature of the interaction. Finally, the dark matter dipole strength is denoted μ_χ. It determines the strength of the interaction, just as the electric charge determines the strength of an electron's interaction with a photon. Finally, $\sigma^{\alpha\beta}$ describes the nature of the dipole interaction. It is a matrix built from Dirac matrices, $\gamma^{0\ldots3}$ as follows $\sigma^{\alpha\beta} = \frac{i}{2}\left[\gamma^\alpha, \gamma^\beta\right] = \frac{i}{2}\left(\gamma^\alpha\gamma^\beta + \gamma^\beta\gamma^\alpha\right)$. For more information on Dirac matrices and proof that this operator represents a dipole operator please see Zee's Quantum Field Theory in a Nutshell pg 194[78]. .

One of the key features of this operator is its chirality. Mathematically, this is due to the operator's off-diagonal components. Physically it means that this term in the lagrangian "flips" the chirality of the particles involved. That is, if a left-handed particle scatters off an object via this operator, it will leave the interaction a right handed particle. It means that the operator changes the state of the particles involved in the interaction.

3.2 Dipoles in nature

Dipoles are common in nature: all the non-neutrino fermions possess dipole moments. While these behave in similar ways phenomenologically, they arise from different sources. In this section we will briefly discuss the ways in which these interactions arise and their properties. Before we discuss this, we require a brief discussion of the two different types of dipole moment, electric and magnetic. The primary difference between the two is that, at zero velocity, a particle with an electric dipole will react to an electric field whereas one with a magnetic dipole will react to a magnetic field. As the particle increases its velocity, a static electric field becomes moving electric field in the reference frame of the particle. This generates a magnetic field, and hence a moving particle with a magnetic dipole can interact with a "pure" electric field and vice versa. Both dipoles arise classically from similar physical situation: a seperation of charge (positive and negative electric charge for the electric dipole, two magnetic poles for the magnetic), and are expressed via similar quantum operators. For the magnetic dipole the interaction term is given in equation (3.2) and the electric dipole's term is created by adding the "fifth" Dirac matrix γ^5 after the dipole operator in (3.2).

In this work, we do not consider the possibility that dark matter interacts via an electric dipole.

Because the electric charge of atomic nuclei are always considerably larger than their magnetic fields, a WIMP with an electric dipole moment (EDM) has a considerably higher chance of interacting in a direct detection experiment than one with a magnetic dipole moment. For this reason, the constraints on EDM Dark Matter are much more severe, and hence the phenomenology is less interesting.

3.2.1 Electron Dipole Moment

The electron has both a magnetic and an electric dipole moment. The magnetic dipole arises classically from the fact that it has an electric charge and spin. A rotating electric charge creates a magnetic dipole, and hence a detectable dipole moment. However, the actual value of the electron's magnetic moment is different from that predicted classically.This is due to an additional effect known as the "anomalous magnetic dipole". This is a contribution to the value of the electron's magnetic moment caused by virtual particles appearing in loops. The standard model makes very precise predictions for what this "anomalous" contribution should be, and so its measured value is a very important test of the theory. For this reason the electron's magnetic dipole moment is one of the most accurately measured quantities in physics, with current measurements precise to 0.76 parts per trillion.

The electron's electric dipole does not exist classically as it is considered a point charge, and hence there is no charge seperation (put in terms of equation 3.1, $r \to 0$). Similarly to the anomalous magnetic dipole, it arises through loop effects in quantum field theory. However, it only arises at the four-loop level and is thus heavily supressed and very small. Limits published in October of 2013 by the ACME Collaboration place limits on this quantity at $d_e < 8.7 \times 10^{-29}$ e cm. They measure a value of $d_e = -2.1 \pm 3.7_{stat} \pm 2.5_{syst}) \times 10^{-29})$ e cm [15].

3.2.2 Neutron dipole moments

It is easy to see from where an electron's magnetic dipole moment would arise, as it has charge and is rotating. A similar process might follow for a proton. However, the origin of a neutral particle's magnetic moment might seem mysterious. The neutron does, in fact, possess a well measured magnetic dipole. Its presence arises from the fact that the neutron is a composite particle. The neutron is made of 3 quarks. While these quarks' charge cancels overall, they have some seperation and each have some definite spin, giving rise to an overall magnetic dipole for the neutron.

Because both protons and neutrons have magnetic moments, the nuclei of atoms also possess magnetic moments. These are, in fact, key to detecting WIMP dark matter. A more detailed discussion of them can be found in chapter 6.2 *Dipole Form Factors*

3.3 Dipole operator as effective operator

The term "Effective Field Theory" describes the philosophy that a field theory can be a useful predictive descriptor of nature, and yet still be ignorant of the physics beyond some "cut-off" energy scale. This "cut-off" gives an energy above which the theory no longer acurately predicts nature, it is the energy at which phenomena not described in the theory become important. We say this theory is an effective theory in the energy range under discussion.

An excellent example of this is quantum electrodynamics of electrons. This theory describes and predicts the behaviour of electrons, positrons and photons, and can do this without any knowledge of other gauge forces, or the other fermions. This theory works up until energies equal to twice the muon mass. At this point muon pairs can be created. The theory does not contain information about this, and ceases to accurately describe nature. Quantum electrodynamics of electrons is an effective field theory with a cut-off of 310 MeV (twice the muon mass).

However, someone with knowledge of field theory might point out that even at energies below 310 MeV, virtual muons should appear in loop diagrams which contribute to processes in quantum electrodynamics. How does the theory account for these? For particles like muons, the simple answer is that we can parameterize our ignorance in a few variables which are experimentally measurable. Parameters that depend on the physics above the cut-off are measured experimentally, and that value is used. Our theory remains predictive.

There is also the possibility that behaviour exists in nature which is not predicted by the effective theory. These behaviours, like the neutrino dipole moment below, must be included in the effective theory somehow. Rather than expand the theory to higher energies and re-calculate the theory with all the added phenomena included, we can instead "integrate out" the higher energy physics, leaving an effective operator that captures this new behavior. This process involves calculating the effect the higher energy loops have on the theory, and include this effect as an operator in the new theory.

3.3.1 Neutrino Dipole Moment

In the standard model, all neutrinos are left handed, and so cannot undergo the chirality flip necessary for a dipole interaction. However, if we were to extend the standard model slightly to include right handed neutrinos, the neutrino gains a dipole moment. While this effect has not yet been observed in nature, it serves as an illustrative example to show how neutral, non-composite particles could gain a dipole moment.

Even with the introduction of a right handed neutrino, the neutrino has no tree level electromagnetic interactions (that is, it is not charged). This is equivalent to saying the the field theory of the neutrino has no operators that couple it to the electromagnetic field. However, the electron neutrino does have couplings through the weak interaction to the electron. This leads to loop level diagrams like the following [27].

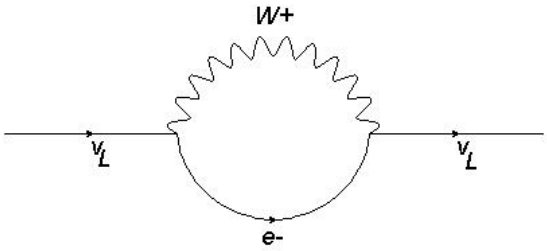

Figure 3.1: A loop level diagram present in the Standard Model

Once this diagram is drawn, it becomes obvious that we can attach a final state photon to either one of the particles inside the loop, which are both charged. This gives rise to diagrams as shown in Figure 3.2.

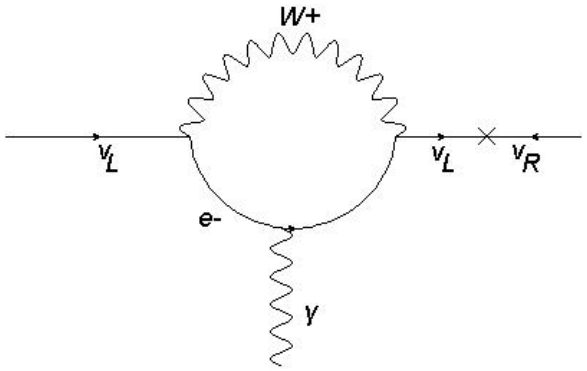

This means that there is a coupling to the photon at loop level which is not present at tree level. In our effective theory of the neutrino, in which we integrate out all loop processes, we must include this coupling in order to accurately describe nature. If we calculate this loop diagram, integrating out the electron and W-boson, we find that this loop-level contribution gives the same result as a tree-level dipole interaction, with the dipole strength determined by the properties of the W-boson, the eletron and the particular extension of the Standard Model employed to allow for the diagrams in Fig 3.2. Thus, to include this interaction in an effective field theory of the neutrino, all we need to do is insert the operator given in section 3.1 with the calculated value for μ

Before ending this section, two important points should be raised as to the above diagrams. Firstly, even with the addition of a right handed neutrino, there are difficulties in creating the diagrams above. The right handed neutrino would be completely sterile, having no couplings to either the electron or the weak bosons. For this reason, the chirality flip would have to occur on the external leg of either diagram. This essentially means that the process occurs entirely with a left

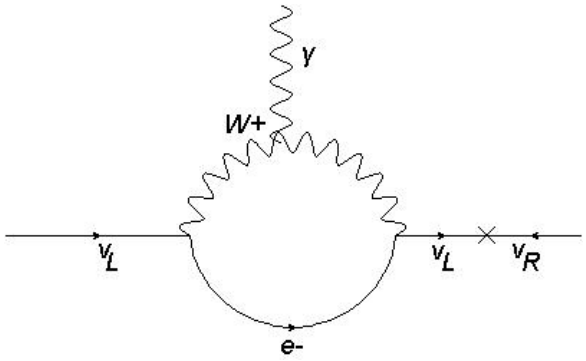

Figure 3.2: Loop diagrams giving rise to neutrino magnetic moments

handed neutrino which then oscillates into a right handed neutrino. For this to occur the left-handed and right-handed eigenstates of the neutrino must mix, and for this to occur the neutrino must have mass. Due to the fact that neutrino type oscillations have now been observed, we know that at least two of the neutrino types must have mass, and therefore this process may exist in nature [17]. .

3.4 Dipole Dark Matter

We have now seen the three ways in which particles can gain a dipole moment, by having an electric charge and a spin, like the electron, by being a composite particle like the neutron, or by coupling to something which is charged, like the neutrino. If a particle does not possess one of these properties, it cannot have a dipole moment.

Charged dark matter is heavily ruled out by both collider and direct detection experiments, ruling out the possibility of dark matter obtaining a dipole moment in the same way as an electron. The remaining two options, constituent dark matter and coupling to some heavier charged physics, are both under active investigation. Of the two, some progress has been made in limiting the parameter space of constituent dark matter by collider experiments. The constituent particles must be lighter than the Dark Matter particle itself, and must be charged, making them easy to look for in colliders. The latter option, however, is less well constrained[68] . Dark matter that has a coupling to some heavy physics which couples to the standard model can lead to a dipole interaction such as the one described for the neutrino above, shown in figure 3.3[72]. Figure 3.3 shows the dark matter particle annihilating into a photon by creating a loop of some unknown heavier particle which itself is charged. This will lead to a Lagrangian of the form

$$\mathcal{L}^{\chi}_{int} = \frac{1}{2}\mu_{\chi}\bar{\chi}^{*}\sigma_{\mu\nu}F^{\mu\nu}\chi + c.c. \tag{3.3}$$

Limits can then be put on the value of μ, and hence the heavy physics by experiment.

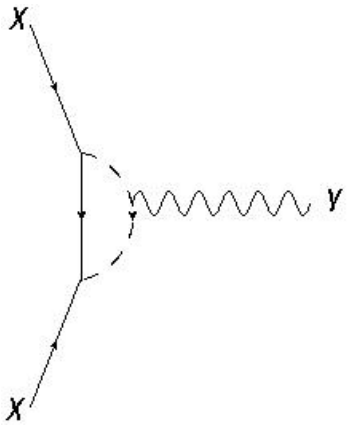

Figure 3.3: Two WIMPs Annihilating via a charged loop of an unknown heavier particle to a photon.

3.5 Inelastic Dark Matter

As discussed in Chapter 2, altering the kinematics of dark matter scattering can have a powerful effect on the phenomenology of direct detection. Interestingly, the off-diagonal properties of the dipole operator make it perfect for this purpose. We can construct a model in which there are two dark matter states, one of higher mass, and one of lower mass [23]. The dipole interaction can then mediate between them. In other words the dipole interaction exists only between two particles in different states. Provided the difference in mass (or mass splitting) between these two states is sufficiently high, the low temperature of the current universe will mean that only the lower mass state will currently be abundant (the WIMPs simply don't have enough energy to excite the higher state). The combination of this fact, and the requirement that scattering exists only between two different states will mean that any scattering will necessarily lose energy to exciting the higher dark matter state, and therefore be an inelastic process. If we label the unexcited state χ and the excited state χ^* a scattering process will look like this: $\chi N \rightarrow \chi^* N$, with the elastic case ($\chi N \rightarrow \chi N$ highly supressed or forbidden by our model).

We therefore have 3 parameters in our model to explore. First we have μ_χ, the dipole strength, which dictates the strength of the interaction and hence the ease with which we will be able to detect dark matter. Secondly we have m_χ, the mass of the WIMP, which will dictate the WIMPs' number abundance, and also part of the kinematics of the equation. Finally we have δ, the mass splitting (that is, the difference between the mass of χ and χ^*. This will dictate how inelastic the scattering process is, and therefore how the kinematics of the interaction change with energy.

Chapter 4

Capture In The Sun

As discussed in chapter 2, one of our most powerful windows into the nature of Dark Matter is through its annihilation products. Detecting these products would provide great insight into not only the mass of the Dark Matter particles, but also the nature of their coupling to the Standard Model particles.

The power of indirect detection lies in the information that can be obtained from a WIMP's annihilation products. A detection of standard model particles (the type of which will be discussed below) would not only confirm the existance of WIMPs' coupling to the standard model but would also, via the type of particles detected, give an indication as to its nature, and via the particles' energy, allow us to determine the WIMP mass.

This chapter will outline in detail one process by which this kind of detection could occur in our solar system, namely by means of WIMP capture in the sun. We first discuss the proposal of the idea and the motivation behind it, before covering the mathematical model we will be using to calculate our expected detection rate.

4.1 Increasing the annihilation rate

As discussed in Chapter 2, the density of WIMPs was fixed in the early universe when 'freeze-out' occured. The density is unchanging due to the fact that WIMPs are sufficiently uncommon that annihilations occur very rarely, and thus the number of WIMPs is not decreased significantly by annihilation. Unfortunately, this also makes indirect detection very difficult. In order to detect a flux of standard model particles from WIMP annihilation, such an annihilation must be sufficiently common to distinguish it from the background flux of those same standard model particles. We must therefore consider one of two options, namely, scenarios in which the annihilation rate is greatly increased, or scenarios where the background is low, or can be reduced.

In 1985, two American scientists William Press & David Spergel were struggling with the then

unsolved problem of solar neutrinos. The issue was that the neutrino number detected from the Sun was considerably lower than predicted by models of solar fusion. Without these neutrinos it seemed as though fusion wasn't occuring at sufficient levels to power the Sun, and hence the energy source for the sun was a mystery. Today, we know that the actual reason for this seeming lack of neutrinos is neutrino oscillation. The Sun emits the predicted flux of electron neutrinos, but through interactions in the interior of the sun and ambient oscillations on the journey between the Sun and Earth, a proportion of them have oscillated into the harder to detect muon and tau neutrinos by the time they reach Earth.

Press & Spergel's solution was to posit the existence of new particles which interact at approximately the weak scale, of a mass between 5 and 60 GeV. These particles would be captured by the sun by accretion. Once captured, they will thermalize and become concentrated in the core of the Sun [63]. This process is the subject of this chapter. Once within the Sun's core, these particles interact with the baryons there, transporting heat away from the center, and thus the core temperature gradient. This would have the effect of reducing the neutrino count (see Littleton, Van Horn and Helfer, 1972[53].)

Press & Spergel initially didn't link these so-called 'cosmions' (as they named them) with WIMP dark matter, but made the connection later[49] . While the solar neutrino problem was solved in the manner described above, Press & Spergel's work retains its relevance due to subsequent work by Silk et al. 1985; Gaisser et al. 1986b; Srednicki et al. 1987; Griest and Seckel 1987[69, 58, 40] . They realized that the capture of WIMPs in the Sun was an inevitability provided the WIMPs interacted with standard model particles, and that this capture could potentially enhance the WIMP annihilation rate enough to facilitate indirect detection.

As the annihilation rate is proportional to the number density squared, any process which increases the abundence of WIMPs locally has this effect. If this gravitational capture occurs in our Sun, it will result in an overabundance of WIMPs located in a region around the center of the Sun. These annihilate into Standard Model particles. Without assuming too much about the annihilation products, we can predict which of these particles we can detect, and which we would not see. The Sun is opaque to charged matter, so annihilations into electrons or positrons interact quickly with the material of the sun, and cannot escape. Muons lose energy very quickly before decaying at rest, producing low energy neutrinos which can escape from the Sun. Similarly, π^+ particles will be stopped and will decay at rest, producing neutrinos. In contrast, a π^- will be captured and absorbed by nuclei without decaying. The neutrinos from the stopped muons and pions can, in principal be detected on Earth (see chapter 7). However, the fact that the decaying particles have been stopped means that the resulting neutrinos are low energy ($\sim$ MeV). In this region, the signal region is dominated by radiation caused by interactions with cosmic ray muons and also by atmospheric neutrinos. This background is high, and hard to remove[26]. For this reason, a higher energy neutrino signal would be easier to detect. This type of signal can be generated by the decays of τ particles and Z

and W^+ bosons[56].

The decay of τ leptons via the W^- produces high energy electron antineutrinos with a distinctive energy spectrum. The decay also produces the easier-to-detect muon neutrinos twice as often, thus increasing the potential number of detectable events. The boson decay channel can produce neutrinos directly. Each neutrino will have an energy equal to the mass of the dark matter, and hence these decays will produce a clear neutrino signal in detectors. These neutrinos can have much higher energies than the neutrinos produced by fusion in the Sun, as these latter neutrinos have energies O(MeV), and dark matter can have energies up to O(1000 TeV).

4.2 How Capture Occurs

The density of WIMPs locally to the Sun is known to be $\sim 0.3 GeV/cm^3$[22] . This number comes from assuming a standard dark matter halo, and is similar among various N-Body simulations. Please see Bovy & Tremaine, 2012 for more details [22]. WIMPs are assumed to have a mass between 1 GeV and 1 TeV [55]. For the purposes of illustration, let us posit a WIMP with a mass of 100 GeV. Let us also assume that the dark matter is stationary with respect to the glactic center. Our Sun is therefore moving at $\sim$ 220 km/s with respect to the dark matter rest frame. In this scenario there will be 6×10^9 WIMPs passing through an area of one meter squared every second. The Sun has a circular area of $\sim 10^{18} m^2$. The Sun therefore has $\sim 10^{28}$ WIMPs passing through it every second. If these WIMPs have some coupling to matter, a fraction of the particles passing through the Sun will scatter off solar nuclei. Each time a scattering like this occurs, the WIMP will lose some energy, and hence some speed. If the WIMP loses enough speed to drop below escape velocity, it will no longer have sufficient velocity it will be gravitationally bound to the Sun. Following Gould [36], we can calculate the frequency of this event as follows.

Let us label the WIMPs velocity at an infinite distance by u. This velocity is given by some velocity distribution dependent on the Dark Matter distribution local to our solar system, which we discuss in Chapter 8, section 2. As it moves closer to the Sun, the WIMP will be accelerated by the gravitational force of the Sun. Its velocity at some finite distance r from the center of the Sun is then given by

$$\omega = \sqrt{(u^2 + v_e(r)^2)} \tag{4.1}$$

Where $v_e(r)$ is the escape velocity at r, which is given by $v_e = \sqrt{\frac{2GM(r)}{r}}$. Here G is the gravitational constant and M(r) is the mass contained within a radius r. When the WIMP is outside the radius of the Sun this is the total mass of the Sun. Once the WIMP enters the Sun, this mass becomes the mass contained within a sphere of radius r. Note, this assumes that the Sun is spherically symmetric.

As the WIMP passes through the Sun, it sweeps out an effective volume of $\omega \sigma t$ Where σ is the scattering cross-section, that is, the effective area that a WIMP appears to have to a nuclei in the Sun. t is the amount of time the WIMP spends within the Sun. If the density of nuclei in the sun

is n, a given volume V will contain nV nuclei. The volume swept out the by the WIMP therefore contains $\omega\sigma nt$ nuclei. This number is equal to the probability of a scattering event occuring.

Scattering events can be categorized by a recoil energy E_R, this is the energy imparted to the nuclei by the WIMP during the collision. In an elastic collision the energy is conserved, so this recoil energy imparted to the nuclei is the same as the energy lost by the WIMP. This energy can range from a minimum value Q_{Min} to a maximum labelled Q_{Max}. Scattering events are spread evenly over this range of energies. In order for a WIMP to be captured by the Sun, it must lose enough energy such that its velocity is less than the escape velocity. We label the minimum recoil energy for this to occur as Q_{cap}. Any event whose recoil energy is larger than this results in capture. Therefore, the fraction of scattering events that result in capture is given by the ratio of the range of events that result in capture and the total range of recoil energies available to the scattering events, mathematically, this is

$$\frac{Q_{Max} - Q_{Cap}}{Q_{Max} - Q_{Min}}. \tag{4.2}$$

Combining these two equations gives an expression for the probability of a capture occuring for a WIMP of velocity ω.

$$\Omega(\omega) = n\sigma\omega t \frac{Q_{Max} - Q_{Cap}}{Q_{Max} - Q_{Min}} \tag{4.3}$$

In order to find the number of WIMPs captured by the sun, this must be combined with two other factors. First, the number of WIMPs with a velocity ω and second, the amount of time a WIMP spends within the Sun, t.

The first of these factors is fairly straightforward. As stated above, the initial velocity is given by a function determined by the distribution of DM in the local neighbourhood. Let us assume this distribution is isotropic in the Dark Matter halo's rest frame and label it $f(u)$. In order to find the distribution in the rest frame of the Sun, we must boost the distribution by the Sun's velocity in this frame, which we call V_0. This gives us a distribution $f'(u)$. Now, consider a sphere of radius R centered on the Sun. We are interested in the initial velocity of the WIMPs, before they come under the influence of the Sun's gravity, so we will let $R \to \infty$. The number of WIMPs with a velocity between u and $u + du$ with an angle from the normal between θ and $\theta + d\theta$ is given by $\frac{1}{2}f'(u)dud\,(cos\theta)$. The WIMPs' velocity in the direction of the normal (that is, in the direction perpendicular to the surface element defined by the angle between θ and $\theta + d\theta$) is $ucos\theta$. Therefore the flux of WIMPs through such a surface element with velocity between u and $u + du$ is

$$f'(u)udud\cos^2\theta \tag{4.4}$$

. The transition from u to ω is then simple, as the escape velocity is the same for all WIMPs, regardless of initial velocity, and is determined by the density profile of the Sun, via the equation given at the beginning of this section.

The second of these factors is a little more complex. In order to calculate it, we must first change

variables. Define the angular momentum per unit mass as follows: $J = Ru\sin\theta$. The Jacobian for converting $d(\cos^2\theta)$ to dJ^2 is therefore given by $d\cos^2\theta = \frac{dJ^2}{R^2u^2}$. If we then integrate over our sphere, we gain a factor of $4\pi R^2$. This gives the expression for the total number of WIMPs entering the region per unit time: $4\pi\frac{1}{4}f'(u)\frac{1}{u}dudJ^2$. [36]

As the WIMP is moving at a non-relativistic speed, the time it spends moving across a distance r is given by this distance divided by the WIMP's speed. For a thin shell of solar matter at radius r with a width dr, the WIMP spends therefore a time given by

$$\frac{2}{\omega\cos\theta}X_s\left[1-\cos\theta\right]dr, \tag{4.5}$$

Here, X_s represents the Heaviside step function, ω is the total speed of the WIMP (including both initial velocity and velocity gained from gravitational acceleration) and hence $\omega\cos\theta$ is the velocity parallel to the vector $\mathbf{r}$. The factor of 2 comes from the fact that the WIMP will pass through the Sun twice during the course of one orbit and the theta function limits the equation to only those WIMPs which pass through the sun. Switching again to using angular momentum varaiables, with the definition of J given above, we see that this expression becomes

$$\frac{2}{\omega}\left[1-\frac{J^2}{r^2\omega^2}\right]^{1/2}dr\theta\left(r\omega-J\right) \tag{4.6}$$

. Combining the above calculations and integrating over the angular momentum gives an expression for the differential capture rate per unit volume (see Gould, 1987 for more details [36].))

$$\frac{dC}{dV} = \int\frac{f(u)}{u}n\omega^2\sigma\frac{Q_{max}-Q_{cap}}{Q_{max}-Q_{min}}du. \tag{4.7}$$

In order to find the total capture rate, one must integrate over the volume of the Sun.

4.3 Recoil Energy-Elastic and Inelastic Case

It is worth noting that this expression can be split into four distinct, but intertwined sections, each dependent on a different physical process. First there is the part dependent on the solar composition, namely the density of target nuclei, n and the volume differential. Secondly there is the velocity distribution, which is dependent soley on the large scale distribution of WIMPs. Third, there is the particle physics model dependent part, the cross section. Finally there is the energy fraction, which is determined by the dynamics of the scattering. As outlined above, the quantity of relevance for the capture rate is the energy lost by the WIMP. For elastic scattering this is equal to the recoil energy of the nucleus and for inelastic it differs only by the inelastic parameter.

This quantity is easily determined by examining the kinematics of the scattering, and it is done below for inelastic scattering. The elastic case is trivial to derive, and can also be found by taking

δ to zero in equations 4.8-4.11.

4.3.1 Inelastic Scattering

As discussed in Chapter 2, another important way that dark matter models can be modified is by introducing a second state with a higher mass. If, as shown in Chapter 3, the WIMPs interaction with standard model particles mediates between these two states, the collisions which lead to solar capture will be an inelastic one. This means that some of the energy initially present in the interaction will be lost to the excited state, modifying the kinematics of the collision.

This modifies the expressions above in two ways. Firstly it changes the cross-section for scattering, please see Chapter 5 for a discussion of this. The second modification appears in the expressions for Q_{Max}, Q_{Min} and Q_{Cap}. In the elastic case (that is, the case where no energy is lost in the collision) the minimum energy available for a scattering event is 0. However, in the inelastic case the interaction requires a center of mass energy equal to or larger than the inelastic splitting. Without at least enough energy to excite the higher mass state the interaction cannot take place, and so any WIMPs whose velocity is too low do not scatter. This means that the minimum energy which can result in scattering is given by[57]

$$Q_{Min} = \frac{1}{2} m_\chi \omega^2 \left(1 - \frac{\mu^2}{m_N^2} \left(1 + \frac{m_N}{m_\chi} \sqrt{1 - \frac{\delta}{\mu\omega^2/2}} \right)^2 \right) - \delta. \tag{4.8}$$

Here, δ is the inelastic paramter, or mass splitting. This is the difference in mass between the two dark matter states. The two factors of δ present in the expression come from the increase in mass of the WIMP during the collision and the loss of available energy in the process respectively. μ is the reduced mass of the system, given by $\frac{m_N m_\chi}{m_N + m_\chi}$, where, as before, m_N is the nuclei's mass and m_χ is the WIMP's. The above equation also holds in the elastic case; as $\delta \to 0$, $Q_{Min} \to 0$ also.

Similarly, the maximum energy available to the scattering is reduced, as the scattering event is now inelastic, and loses some energy to exciting the state. This is given by[57]

$$Q_{Max} = \frac{1}{2} m_\chi \omega^2 \left(1 - \frac{\mu^2}{m_N^2} \left(1 - \frac{m_N}{m_\chi} \sqrt{1 - \frac{\delta}{\mu\omega^2/2}} \right)^2 \right) - \delta. \tag{4.9}$$

This also holds for the elastic case, as taking δ to zero here gives the center of mass energy of the system. Finally, the recoil energy required for capture is changed. In the elastic case, Q_{Cap} is given by the lowest possible energy with which the nuclei can recoil and still reduce the WIMP's velocity to below v_{esc} (the escape velocity). As the WIMP's total velocity is given by $\omega = \sqrt{u^2 + v_{esc}^2}$, the WIMPs initial energy is given by $\frac{1}{2} m_\chi \left(u^2 + v_{esc}^2 \right)$. In order to be captured, the WIMP must have a velocity of less than the escape velocity, or an energy of less than $\frac{1}{2} m_\chi v_{esc}^2$ and hence must lose $\frac{1}{2} m_\chi u^2$ or $\frac{1}{2} m_\chi (\omega^2 - v_{esc}^2$. In the elastic case, no energy is lost, so that the energy that the WIMP

loses is equal to the energy the nuclei gains:

$$Q_{Cap}^{Elastic} = \frac{1}{2} m_\chi \left(\omega^2 - v_{esc}^2\right). \tag{4.10}$$

However, in the inelastic case, these two energies are not equal. While the energy loss required for the WIMP to be captured is the same, the amount of energy absorbed by the nucleus is reduced by the mass splitting between the two states, giving a capture energy of

$$Q_{Cap} = \frac{1}{2} m_\chi \left(\omega^2 - v_{esc}^2\right) - \delta. \tag{4.11}$$

These modifications have an important effect on the capture rate. The easiest way of seeing this is by looking at the expressions for the mimimum, maximum and capture energy and the centre of mass energy. By looking at the relations between them and their physical importance, we can gain some insight into the way the inelastic scattering effects the capture rate.

The most obvious way in which the inelastic parameter effects the physical properties of the scattering is via the centre of mass energy of the WIMP-nucleus system. This is given by $\frac{1}{2}\mu\omega^2$ (where μ is the reduced mass as given above) and describes the total energy available to the scattering event. Therefore, as discussed above, it must be larger than the inelastic parameter in order to overcome the mass splitting and for scattering to occur. Its effect on scattering can be seen by looking at an example model for which the dark matter mass, $m_\chi = 100GeV$ and the mass splitting (or inelastic parameter), $\delta = 200KeV$. We can then look at the cases for which $E_{CM} - \delta < 0$. For hydrogen ($m_n \sim 1GeV$), the centre of mass energy is less than the inelastic parameter for any WIMP speed $\omega \lesssim 0.02c$. $0.02c$ is approximately 6000 km/s, a factor of 10 larger than the escape velocity (v_{esc}) at the surface of the Sun ($\sim$ 600 km/s) and 30 times larger than the typical initial WIMP velocity ($\sim$ 220 km/s). Assuming a Maxwell-Boltzmann distribution for the WIMP velocity (see Chapter 8 for a discussion of velocity distributions), gives the probability of finding a WIMP of a velocity $\sim$ 6000 km/s is approximately 10^{-388} of the probability of finding a WIMP at $\sim$ 220 km/s. This means that hydrogen, which makes up $\sim$ 70% of the nuclei in the Sun,[38] is incapable of scattering WIMPs in this model. This is a very important effect. In the elastic model no such limitation exists and hydrogen's large abundance (coupled with its relatively high magnetic moment) contributes a great deal to the capture rate. Here, it is rendered completely irrelevant because of its low mass, which causes the centre of mass energy of the WIMP-nucleus system to be too low at the WIMP velocities in question to overcome the mass splitting.

In order to have a large enough energy to overcome the mass splitting in our toy model, we require a larger mass nucleus. Condsidering the next most abundant element, helium, whose mass is $\sim$ 3.7 GeV, we find that the centre of mass energy is larger than the mass splitting for velocities above $\sim$ 3000 km/s. While this velocity is more likely, we still need an initial WIMP velocity a factor of 10 larger than the mean velocity. For every $\sim 10^{40}$ WIMPs with an initial velocity equal

to the mean velocity, there is only one WIMP at this velocity meaning that helium's contribution is also greatly reduced.

The next most abundant element is carbon. This has a mass of ~ 11 GeV but only makes up $\sim 0.02\%$ of the atoms in the Sun. It requires an initial WIMP velocity of ~ 1800 km/s in order for scattering to occur. For every $\sim 10^{10}$ WIMPs at the mean velocity, only 1 WIMP exists at this velocity.

The overall effect of this is, therefore, to reduce the importance of lighter elements relative to heavier ones. Lighter elements are more abundant, so by reducing their effect or making them entirely irrelevant (as with hydrogen in our toy model), the capture rate will be greatly reduced. It is easy to see that by decreasing the mass splitting, we increase the imporance of lighter elements, as the system has a smaller energy barrier to overcome, and by increasing the mass splitting, we reduce the effect of the lighter elements. As we continue to increase the mass splitting, we can expect to see elements stop contributing entirely to the capture process in order of mass. For hydrogen, this occurs before $\delta \sim 200keV$, as seen in our model. For helium, it occurs at a higher energy, for carbon, higher still. This process will continue to occur until even nickel (at a mass of ~ 55 GeV) will be unable to scatter any WIMPs, and solar capture will completely cease.

A secondary effect of this property is due to the fact that the inelastic scattering prevents lower velocity WIMPs from scattering. This means that the shape of the high energy tail of the WIMP distribution becomes very important. This effect will be further analyzed in Chapter 8.

Another effect that serves to decrease the total capture rate is the relationship between Q_{Max} and Q_{cap}. In order for capture to occur, the recoil energy of the nucleus must be at least Q_{cap}. However, kinematic considerations limit the recoil energy, so that it must be less than Q_{Max}. Therefore, if there is a region of parameter space in which $Q_{Cap} > Q_{Max}$, capture cannot occur. In both the inelastic and the elastic case this occurs at high velocity. This is to be expected; if a WIMP has a very high initial energy, it is unlikely that a collision with nuclei of equal or lower mass will rob it of almost all of that energy. In the inelastic case, however, the velocity at which this cut-off occurs is lower. This is because, while the amount of energy that the WIMP needs to lose is independent of the kinematics of the scattering, the inelastic nature of the scattering means that the maximum amount of energy that the nuclei can absorb is reduced.

Once again, this is a reduction that effects lower mass elements more strongly, as their ability to absorb energy in a scattering event is reduced due to their lower mass. To see this effect we can look at hydrogen in our example model. Here, $Q_{Cap} > Q_{Max}$ for WIMP velocities larger than $\sim 0.0037c$ or ~ 1000 km/s. This is only about 5 times the average WIMP initial velocity, and only about twice the maximum escape velocity. However, for helium the cut off does not occur until ~ 2400 km/s. This serves to balance the effect discussed above whereby the capture rate for high velocity is enhanced by the balance between the centre of mass energy and the inelastic parameter. However, it is another factor that reduces the importance of low mass scatterers, making the mass splitting at

which each becomes irrelevant even lower.

Increasing the inelastic parameter makes the nuclei even less efficient at absorbing the WIMPs' energy. This reduces the velocity at which Q_{Cap} becomes less than Q_{Max}. Therefore this high-velocity cut off becomes more important at higher mass splittings for all elements. For a high enough mass splitting, Q_{Max} becomes so small that no capture can occur.

Finally there are several lesser effects that serve to enhance capture rate. Firstly, we must consider the parameter space in which $Q_{Cap} \leq Q_{Min}$. In this regime, the minimum energy gained by the nucleus (and hence lost by the WIMP) is greater than the energy loss needed for capture. Thus all scattering events in this regime lead to capture. This occurs in the low velocity region, where Q_{Cap} is small. Increasing the mass of the target nucleus decreases the minimum scattering energy, therefore the parameter space in which $Q_{Cap} \leq Q_{Min}$ is true becomes smaller (as Q_{Cap} is independent of m_N). This means that this effect serves to enhance capture rate for lower mass elements. However, we will show in chapter 8 via simulation that this effect is a small one compared to those discussed above.

The final parameter range we will discuss is that in which the energy required for capture is less than the mass splitting, that is $Q_{Cap} < 0$. This means that losing the energy required for scattering to occur is sufficient to capture the WIMP. As Q_{Cap} and δ are independent of nuclear mass, this affects all elements identically. This means that the overall effect of this parameter space is to enhance the capture rate for low velocity WIMPs for which $E_{CM} > \delta$ but $Q_{Cap} < 0$. This effect is largest for a high value of the mass splitting, but a low WIMP mass.

4.4 Thermalization

Thermalization is the process in which WIMPs lose energy via collisions with solar nuclei until such a time as they are in thermal equilibrium in the center of the star. In order for annihilation to occur at a significant rate, the WIMPs must be densly concentrated in a small region. This happens once the WIMPs are thermalized, as, after thermalization, WIMPs are concentrated inside a small radius given by $r_{th} = \left(\frac{9T}{8\pi G \rho_c m}\right)^{1/2}$. Where T is the temperarture in the core of the Sun, and ρ_c is the core density. For the Sun, $T \sim 10^7 K$ and $\rho \sim 150 g/cm^3$. This gives a thermal radius of approximately $r_{th} \sim 2 \times 10^8 cm \left(\frac{m}{TeV}\right)^{-1/2}$.

Once the WIMP has thermalized, we can use arguments of equilibrium (see next section) to calculate the annihilation rate. However, before we do this we must ensure that the WIMPs thermalize sufficiently rapidly in order for these arguments to hold. We follow Kouvaris and Tinykov[48] and estimate WIMP thermalization time by splitting the process into two parts. During the first part the WIMP's orbit takes it outside the Sun. During this time, collisions with nuclei during the section of the orbit which takes the WIMP inside the Sun cause it to lose energy, reducing the radius of the WIMP's orbit until the orbit is entirely contained within the Sun.

During the second section, the WIMP's orbit is entirely inside the Sun. Here, continuous collisions cause the WIMP to continue losing energy until it thermalizes with its surroundings. We can estimate the length of time taken for each of these sections to occur as follows:

The time between collisions (δt) is given by half of the length of one period of the WIMPs orbit, multiplied by the ratio of the WIMP-nuclei cross-section divided by the critical cross-section, which is defined as $\sigma_{crit} = \frac{m_N R^2}{M}$ where R is the solar radius and M is the mass of the sun. Each time a collision occurs the WIMP loses an average of $\frac{2m_N}{m_\chi}$. Averaging over the WIMP trajectory assuming the WIMP passes through the center of the star, the typical energy loss is $\delta E = 2GMm_N\left(\frac{4}{3R} - \frac{1}{r}\right)$ where r is the radius of the WIMP orbit. Divide by δt to get an expression for change in energy over time.

$$\frac{dE}{dt} = -\frac{2\sqrt{2}m_N\sigma}{\pi GMm_\chi^{5/2}}\left(\frac{4}{3}E_* + E\right)|E|^{3/2} \tag{4.12}$$

Where $E_* = GMm_\chi/R$ is the binding energy of the WIMP to the Sun's surface and E is the WIMP's energy.

Integrating from initial WIMP energy to binding energy at the Sun's surface gives

$$t_1 \sim \frac{3\pi m_\chi R^{3/2}\sigma_{crit}}{4m_N\sqrt{2GM\sigma}}\sqrt{\frac{E_*}{|E_0|}} \tag{4.13}$$

Using $E_0/E_* \sim m_N/m_\chi$ and a solar mass star, gives

$$t_1 \sim 3\text{ yr}\left(\frac{m}{TeV}\right)^{3/2}\left(\frac{\sigma}{10^{-35}cm^2}\right)^{-1} \tag{4.14}$$

For the second stage, the time between collisions is given by $\delta t = \frac{1}{n\sigma v}$ where $v = \sqrt{2E/m}$. Therefore

$$\frac{dE}{dt} = -n\sigma v\delta E = -2\sqrt{2}\rho\sigma\left(\frac{E}{m}\right)^{3/2} \tag{4.15}$$

and

$$t_2 = \frac{m^{3/2}}{\sqrt{2}\rho\sigma}\left(\frac{1}{\sqrt{E_f}} - \frac{1}{\sqrt{E_i}}\right) \tag{4.16}$$

$E_i \sim GM/R$ and $E_f = (3/2)kT$ so E_i is much greater than E_f. This means that the second term can be safely ignored for the calculation of t_2. Assuming typical solar parameters gives [48].

$$t_2 = 0.15\text{yr}\left(\frac{m_\chi}{TeV}\right)\left(\frac{\sigma}{10^{-35}cm^2}\right)^{-1} \tag{4.17}$$

Note that during the course of this discussion we have assumed elastic collisions and a constant cross-section. As shown in our discussion of inelastic scattering above, a typical inelastic collision causes the WIMP to lose more energy than a similar elastic collision. This means that the WIMP

will actually thermalize more quickly in the inelastic case, at it is easier for it to lose energy via these collisions.

The effect of a non-constant cross-section on thermalization will be discussed in Chapter 5.

4.5 Annhililation

Capture obviously increases the number of WIMPs inside the Sun. As this number goes up, annihlations also increase. Specifically, they increase with the square of the density. The rate of change in the number of WIMPs in the Sun is therefore governed by the following equation:

$$\dot{N} = C_C - C_A N^2, \tag{4.18}$$

where C_C is the capture rate and C_A is dependent on the annihilation rate as $\Gamma_A = \frac{1}{2} C_A N^2$ where Γ_A is the annihilation rate. This equation has a solution given by [57]

$$\Gamma_A = \frac{1}{2} C_C \tanh^2 \left(t/\tau_{eq} \right). \tag{4.19}$$

where τ_{eq} is the time needed for the system to reach equilibrium between annihilation and capture. It is given by $(C_C C_A)^{-1/2}$. When the time, t is much less than the age of the Sun, equilibrium has not yet been reached, and annihilation is severely supressed. However, if $t_{Sun} >> \tau_{eq}$ the annihilation rate saturates at

$$\Gamma_A = \frac{1}{2} C_C. \tag{4.20}$$

Nussinov et al. [57] show that this condition was met long ago, even for low cross-sections, and hence the annihilation rate is saturated. For the rest of this paper we assume that $\Gamma_A = \frac{1}{2} C_C$.

Chapter 5

Scattering Cross-section

As outlined above, the solar neutrino rate provides a direct probe of the scattering cross-section, which allows us insight into the strength of the Dark Matter-Standard Model interaction. However, the scattering cross-section for the magnetic dipole case is not as simple as, for example, the microcharge case. The form of this cross-section determines exactly how much scattering occurs, at what velocities, and against which elements, making it the most crucial part of the indirect detection picture. It therefore has to be carefully derived from the interaction lagranigian.

5.1 Derivation of the cross-section

In chapter 3.4 we showed that the effective interaction lagrangian for a magnetic dipole interaction is given by

$$\mathcal{L}^{\chi}_{int} = \frac{1}{2}\mu_{\chi}\bar{\chi}^{*}\sigma_{\mu\nu}F^{\mu\nu}\chi + c.c. \tag{5.1}$$

For more details on this interaction, please see Chapter 3.

Taking the nucleus' interaction as a standard spin-1/2 particle interacting with the electromagnetic field, ie.$\mathcal{L}^{N}_{int} = i\bar{\psi}_{N}\gamma^{\mu}D_{\mu}\psi_{N}$ gives rise to a scattering diagram as shown in figure 5.1:

Reading the matrix element off from the Feynamn rules gives

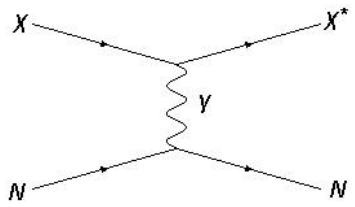

Figure 5.1: A WIMP scattering against a nucleus via an intermediate photon, moving into the excited χ^{*} state in the process

$$i\mathcal{M} = iQ\mu_\chi \bar{\chi}^*(p')\gamma^\mu \mathcal{U}(p)\frac{g^{\mu\nu}}{q^2 + i\epsilon}\bar{\mathcal{U}}(k)\sigma^{\nu\xi}\left(k'_\xi - k_\xi\right)\chi(k'), \tag{5.2}$$

where Q is the charge of the nuclei,p', p, k, k' are the momenta of the particles in the interaction and q is the photon momentum. γ^μ are the Dirac matrices and $g^{\mu\nu}$ is the metric.

In order to find the scattering cross section, first the Gordon Decomposition Identity must be used [61]. This is typically given in the form.

$$\bar{u}(p')\gamma^\mu u(p) = \bar{u}(p')\left[\frac{(p'+p)^\mu}{2M} + \frac{i\sigma^{\mu\nu}(p'-p)_\nu}{2M}\right]u(p), \tag{5.3}$$

where M is the mass of the particle described by the spinors $u(p)$ and $\bar{u}(p')$.

Note that this can be applied in two ways: First, we can apply it directly to the part of the scattering involving the nuceleus. This transforms the matrix element into the following form:

$$i\mathcal{M} = Q\mu_\chi \bar{\mathcal{U}}(p)\left[\frac{(p'+p)_\mu}{2M} + \frac{i\sigma_{\mu\rho}(p'-p)^\rho}{2M}\right]\mathcal{U}(p)\frac{g^{\mu\nu}}{q^2 + i\epsilon}\bar{\mathcal{V}}(k)\sigma^{\nu\zeta}(k'_\zeta - k_\zeta)\mathcal{V}(k'). \tag{5.4}$$

We can then split the matrix element into two parts. One which couples the nuclear momentum to the photon through a current-like interaction, given by taking only the first term in the square bracekts in (5.4), and one which couples them in a dipole-like interaction, given by taking only the second term. The reasons for this are simple: the nucleus has not only a dipole moment from this term, but also a dipole moment arising from the fact that it is made up of charged constituents (See chapter 3 for more details). Both of these parts contribute to the matrix element via a term proportional to $\sigma^{\mu\nu}(p'-p)_\nu$. The total magnetic dipole of each nuclei is made up of a combination of these two effects, and can be experimentally determined. However, the scattering process has no way of distinguishing between the two contributions, so it makes sense to group them together. This is done by defining a new quantity μ_N, which is exactly analogous to μ_χ as it represents the total magnetic moment of the nucleus, including all contributions. Using this knowledge to rewrite the matrix element above gives us

$$\mathcal{M} = \mathcal{M}_{DZ} + \mathcal{M}_{DD} \tag{5.5}$$

where $\mathcal{M}_{DZ}$ is the 'Dipole-Current' matrix piece, given by

$$i\mathcal{M}_{DZ} = \frac{Q\mu_\chi}{2m_N}\bar{\mathcal{U}}(p')(p'+p)_\mu \mathcal{U}(p)\frac{g^{\mu\nu}}{q^2 + i\epsilon}\bar{\mathcal{V}}(k)\sigma^{\nu\eta}(k'_\eta - k_\eta)\mathcal{V}(k') \tag{5.6}$$

and $\mathcal{M}_{DD}$ is the 'Dipole-Dipole' matrix piece given by

$$i\mathcal{M}_{DD} = i\frac{\mu_N\mu_\chi}{2m_N}\bar{\mathcal{U}}(p)\sigma_{\mu\rho}(p'-p)^\rho \mathcal{U}p\frac{g^{\mu\nu}}{q^2 + i\epsilon}\bar{\mathcal{V}}(k)\sigma^{\nu\eta}(k'_\eta - k_\eta)\mathcal{V}(k'). \tag{5.7}$$

It is instructive to deal with the two pieces seperately, as they exhibit very different behaviours, and the final scattering rate depends on the balance between the two behaviours for each elements'

values of Q and μ_N.

5.1.1 Dipole Current Piece

In order to calculate the total scattering rate due to the dipole-current piece, we need to employ the Gordon Identity once more. Here we apply it to the dipole operator which comes from the WIMP's magnetic dipole in equation (5.6)

$$\mathcal{M}_{DZ} = \frac{Q\mu_\chi}{2M_N q^2}\bar{\mathcal{U}}_N(p')(p'+p)^\nu \mathcal{U}_N(p)\bar{\mathcal{V}}_\chi(k)\left[(k'+k)_\nu - 2M\gamma_\nu\right]\mathcal{V}_\chi(k') \tag{5.8}$$

The differential cross-section is then given by

$$\frac{d\sigma}{d\Omega} = \frac{1}{2E_{cm}^2}\frac{|\mathbf{k}|}{16\pi^2 E_{cm}}\frac{1}{4}\sum_{spins}|\mathcal{M}|^2 \tag{5.9}$$

Boosting into the rest frame of the nucleus we can derive a relationship between the recoil energy of the nucleus E_r and $\cos\theta$ where θ is the recoil angle. This gives $E_r = \frac{2\mu^2\omega^2}{m_N}\cos^2\theta$ where μ is the reduced mass of the WIMP-nucleus system, m_N is the mass of the nucleus and ω is the WIMP's initial velocity. As the interaction is isotropic in the azimuthial angle, we can easily shift the variable of integration from the solid angle Ω, to the recoil energy, E_r, by using the relationship above and the fact that $\frac{d\sigma}{d\Omega} = \frac{d\sigma}{d\cos\theta} = \frac{d\sigma}{dE_r}\frac{dE_r}{d\cos\theta}$. Substituting this into equation (5.5)and performing the averaging over spins (which gives rise to terms dependent on the WIMP spin S_χ) gives a differential cross-section of the form:

$$\frac{d\sigma_{DZ}}{dE_r} = \frac{4\pi Z^2\alpha^2}{E_r}\left(\frac{\mu_\chi}{e}\right)^2\left(1 - \frac{E_r}{v^2}\left(\frac{1}{2m_N}+\frac{1}{m_\chi}\right) - \frac{\delta}{v^2}\left(\frac{1}{\mu_{N,\chi}}+\frac{\delta}{2m_N E_r}\right)\right)\left(\frac{S_\chi+1}{3S_\chi}\right) \tag{5.10}$$

5.1.2 Dipole Dipole Piece

Now that we have an expression for the cross-section contribution due to the dipole-current piece, we will move on to the dipole-dipole piece. Recall, that the matrix element for this piece is given by

$$i\mathcal{M}_{DD} = i\frac{\mu_N\mu_\chi}{2m_N}\bar{\mathcal{U}}(p)\sigma_{\mu\rho}(p'-p)^\rho \mathcal{U}p\frac{g^{\mu\nu}}{q^2+i\epsilon}\bar{\mathcal{V}}(k)\sigma^{\nu\eta}(k'_\eta - k_\eta)\mathcal{V}(k'). \tag{5.11}$$

As we saw in the previous section, the cross-section depends on $|\mathcal{M}|^2$. It would seem therefore, that in addition to the dipole-current and dipole-dipole pieces, there should be a term mixing these two pieces as $|\mathcal{M}|^2 = |\mathcal{M}_{DZ}|^2 + |\mathcal{M}_{DD}|^2 + \mathcal{M}^*_{DZ}\mathcal{M}_{DD} + \mathcal{M}^*_{DD}\mathcal{M}_{DZ}$. However, averaging over the spin of the particles involved gives that $\mathcal{M}^*_{DD}\mathcal{M}_{DZ} = -\mathcal{M}_{DD}\mathcal{M}^*_{DZ}$ so the final two terms cancel with each other, leaving only the first two terms, $|\mathcal{M}_{DZ}|^2$ and $|\mathcal{M}_{DD}|^2$.

Performing the same operations on equation (5.11) as in the previous section (namely employing the Gordon Identity, converting to the nuclear rest frame, averaging over spins and employing equation (5.5) gives a differential Dipole-Dipole cross-section of

$$\frac{d\sigma_{DD}}{dE_r} = \frac{16\pi\alpha^2 m_N}{v^2}\left(\frac{\mu_\chi}{e}\right)^2\left(\frac{\mu_N}{e}\right)^2\left(\frac{S_\chi+1}{3S_\chi}\right)\left(\frac{S_N+1}{3S_N}\right) \tag{5.12}$$

These cross-sections match those in Chang et al., 2010 [23] .

To obtain total cross-sections the integral over energy is performed. The energies of relevance to the problem (as outlined in Section 4) are bounded above by the maximum scattering energy Q_{max} and bounded below by the energy transfer required for gravitational capture Q_{cap}. Integrating between these limits gives

$$\sigma_{DZ} = \left[\frac{2\pi Z^2\alpha^2\mu_\chi^2\left(-2E_r\left(m_\chi\delta + m_N\left(-m_\chi v^2+\delta\right)\right)Log\left[Er\right] - \left(E_r^2(2m_n+m_\chi) - m_\chi\delta^2\right)\right)}{e^2 E_r m_N m_\chi v^2}\right]_{Q_{cap}}^{Q_{max}} \tag{5.13}$$

$$\sigma_{DD} = \left[\frac{16\pi\alpha^2 m_N}{v^2}\left(\frac{\mu_\chi}{e}\right)^2\left(\frac{\mu_N}{e}\right)^2\left(\frac{S_N+1}{3S_N}\right)E_r\right]_{Q_{cap}}^{Q_{max}} \tag{5.14}$$

Where we have set the spin of the WIMP to $\frac{1}{2}$.

The key paramater determining the dipole-dipole capture rate is the nuclear dipole moment of each element. The standard theoretical model for this dipole moment is the single-particle model. In this model, nucleons form pairs of the same type, but opposite spin, effectively cancelling one another out. Only unpaired nucleons contribute to the spin. This means that nuclei with even numbers of both protons and neutrons have no nuclear magnetic moment [75]. Calculating the expected nuclear moment in this theory gives two values known as Schmidt values (for the unpaired nucleon spin $l = j \pm 1$). In order to determine which of these values should be taken experiments are performed. Typically, the experimentally determined value lies between the two Schmidt values. This is due to the fact that the "paired" nucleons actually have a non-zero contribution to the moment. These pairs have $J > 0$ but do not contribute constructively to the dipole, causing the true value to be bounded by the single-particle model prediction. It therefore remains true that those nuclei with no unpaired nucleons have no nuclear dipole moment.[75]

For the reasons outlined above, the nuclear dipole moment has to be determined experimentally. We use the The 8th edition of the Table of Isotopes, John & Sons (1999) for experimental values of μ_N^2. (The relevant appendix is availble online here: http://ie.lbl.gov/toipdf/mometbl.pdf)

5.2 Important Features of the Cross-Sections

Using the expressions for Q_{max} and Q_{cap} given in chapter 4, and the cross-sections derived in this chapter we find that, for a typical 100 GeV WIMP scattering off a hydrogen atom, the dipole-current cross-section dominates capture by a factor of approximately 2 over the dipole-dipole cross-section at low energies. As the enery increases, the two parts become more equal. In the final calculations, both pieces will also be surpressed by form factors, which effect the behaviour of the cross-section at high energies. Therefore the final capture rate will come from the effects of inelastic kinematics as discussed in chapter 4, form factor effects, which will be discussed in chapter 6, and the behaviour of the cross section at the relavent energies.

This interplay is very complex and can only really be probed using the full expressions for the capture rate. This is the end goal of this thesis. However, it is instructive to look at the form of the cross-sections and make some qualititative deductions about the behaviour of scattering. This will help us not only in verifying our results later, but also in understanding exactly which aspects of our model are causing the effects we see in our results.

5.2.1 Common features of both cross-sections

Before making any in-depth calculations, we can already discuss some important properties of the cross-sections, and how they will effect the constraints on this model from capture in the sun.

First, it is important that both cross-sections are proportional to μ_χ^2 meaning that all results derived from them can simply be scaled by this coupling. Any constraints, therefore, will be placed on a product of this factor and the branching ratio into neutrinos. This is to be expected, as μ_χ parameterizes the coupling of the dark sector to the standard model.

Another important feature of both cross-sections is their dependence on E_r, which, after integration becomes the expression $Q_{Max} - Q_{Cap}$. These quantities are defined in Chapter 4. The dependence on these energies is important for a number of reasons. Firstly, it controls the velocity (and hence energy) dependence of the cross sections. Secondly, it also controls the energy regions in which the cross-sections are valid. As discussed in chapter 4, kinematic concerns constrain the range of velocities in which scattering can occur. These cross-sections are only valid within those regions. If we try to explore beyond those regions we will see imaginary or negative cross-sections, representing an unphysical event. Apart from this, the two cross-sections have very different behaviours. In the next two sections we will look at their behavior with energy, nuclear mass and mass splitting and also WIMP mass. This will give a good prediction of the final capture rates.

5.2.2 Features of the Dipole-Dipole cross-section

The dipole-dipole cross-section, σ_{DD}, is a simple cross-section, but it has an interesting structure. At first glance, it appears that (5.14) is suppressed by velocity. However, inserting the expressions

given in chapter 4 shows that this is not the case. Inititally, we will look at the case for $\delta \to 0$.

In this case, the cross-section splits into two parts, a positive part which is $\propto \frac{Q_{Max}}{v^2}$ and a negative part which is $\propto \frac{Q_{Cap}}{v^2}$. Looking at equations (4.9) and (4.11) shows that, in the case where $\delta = 0$, $Q_{Max} \propto v^2$ and $Q_{Cap} \propto v^2 - v_{esc}^2$. Recall that $V^2 = v_{esc}^2 + u^2$ where u is the initial velocity of the WIMP. As the escape velocity typically dominates the total WIMP velocity, the capture velocity is largely independent of the total velocity, dependent only on initial velocity. This means that the two terms reduce to a positive one which is constant with velocity and a negative one which is proportional to $\frac{1}{v^2}$. This means that the cross section increases with velocity, asymptotically approaching a value defined by the first term. As $v \to \infty$, $\sigma_{DD}(\delta = 0) \to \frac{2}{\pi}\mu^2\mu_N^2$ where μ is the reduced mass of the WIMP-nucleus system and μ_N is the nuclear dipole moment. The rate at which the cross section approaches the asymptotic value is given by the negative term, which is $\frac{m_N m_\chi \mu_N^2 u^2}{2\pi v^2}$ for $\delta = 0$. Defining the point at which the cross-section is close enough to the asymptotic value as to be indistinguishable from this value as

$$\frac{\sigma_{DZ}(v \to \infty) - \sigma_{DZ}(v_{crit})}{\sigma_{DZ}(v \to \infty)} = 0.01 \tag{5.15}$$

we can find the velocity at which the cross-section reaches its upper limit for the important elements and a range of WIMP masses.

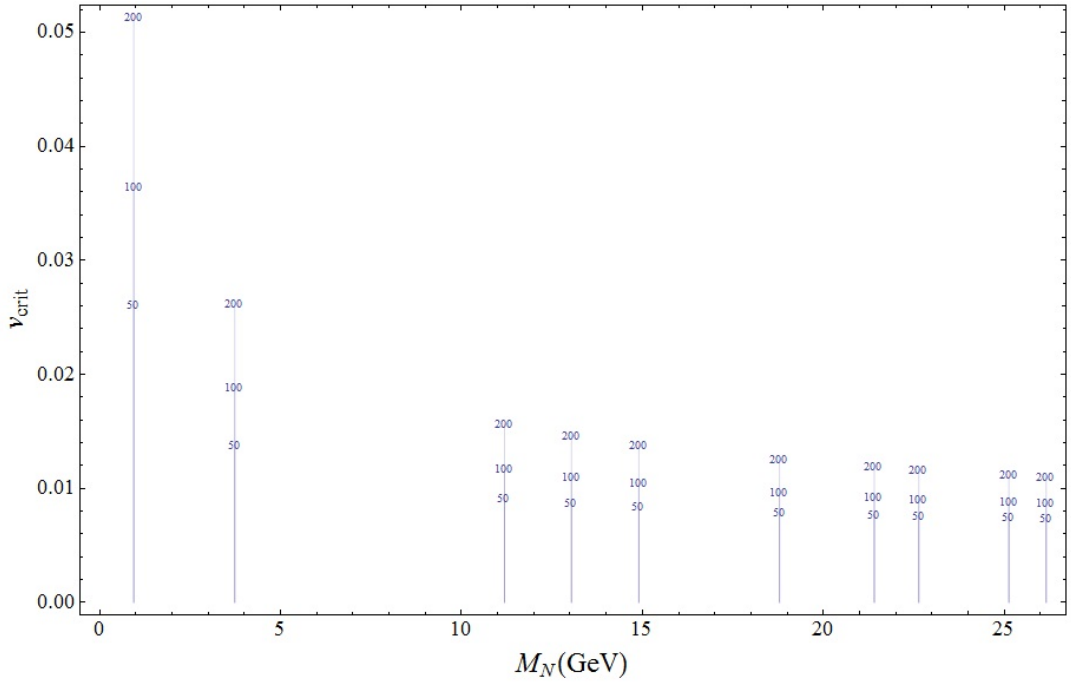

Figure 5.2: The critical velocity plotted against the target nucleus mass, with WIMP mass indicated at each data point.

Here the WIMP mass is indicated at each data point, at the data is plotted for hydrogen,

helium, carbon, nitrogen, oxygen, neon, sodium, magnesium, aluminium and silicon with a constant initial WIMP velocity of 220 km/s. It is easy to see that the maximum cross-section is reached more quickly for higher mass elements. The effect of this is to supress the capture of low velocity WIMPs, and to give an enhancement to heavier elements.

The effect is more complex again in the case where scattering is inelastic. Here, in addition to the velocity-dependent term coming from the Q_{Cap} term, there are additional terms coming from the inelastic parameter. These come in two forms; a group of terms proportional to $\frac{\delta}{v^2}$ and a term proportional to $\sqrt{1-\frac{2\delta}{\mu v^2}}$. The terms proportional to $\frac{\delta}{v^2}$ can be grouped as follows

$$\frac{\delta}{v^2}\frac{m_N\mu_N^2}{\pi}\left[\left(\frac{m_N^2+m_Nm_\chi}{(m_N+m_\chi)^2}\right)-2\right] \tag{5.16}$$

and the term proportional to the square-root given above is

$$\frac{\mu^2\mu_N^2}{\pi}\sqrt{1-\frac{2\delta}{\mu v^2}}. \tag{5.17}$$

Note that (5.17) is always positive, and increasing with velocity, whereas term (5.16) is positive when $m_N(m_N+m_\chi) > 2(m_N+m_\chi)^2$. However, rearranging this relationship shows that this only holds true if $m_N^2+2m_\chi^2+3m_Nm_\chi < 0$, which is impossible for real, positive WIMP masses. Therefore equation (5.16) corresponds to a new negative term in $\frac{1}{v^2}$. The new negative term will serve to slow down the cross-section's asymptotic approach with velocity while the positive square-root term will serve to speed it up. The rate at which this occurs is not as simple to estimate as the square term does not reduce to 0 as $v \to \infty$. However, it is typically several orders of magnitude smaller than the terms given in (5.16) for the mass splittings and velocities under consideration here we can assume that it does not considerably slow the progress of σ_{DD} towards its asymptotic state. For the purposes of showing the effect of the inelastic parameter on this cross-section therefore, we will assume it has zero effect. As can be seen in Figure 5.3, the critical velocity (at which the cross-section can be approximated as its asymptotic state), increases almost linearly with δ. At a value of only $\delta = 100$ keV, it is already as high as $0.1c$, a much larger value than those typical in the scattering. In this case, the capture rate due to dipole-dipole scattering is greatly surpressed by this inelastic parameter, as only extremely high-energy WIMPs have enough velocity to reach the maximal cross-section.

The second important term to point out is the combination of the mass enhancement and dependence on μ_N^2. Alone, the factor of μ_N^2 is important due to the fact that not every element has a nuclear dipole moment. In fact, of the 15 most abundant elements in the Sun, only 4 have stable isotopes with magnetic dipole moments: Hydrogen, Nitrogen, Sodium and Aluminium. This can be seen in the table of elemental properties given in the appendix. This means that all dipole-dipole scattering is off one of these four elements. In the elastic limit hydrogen dominates the scattering by virtue of the fact that is the most abundant by a factor of $\simeq 300$, but the others receive slight

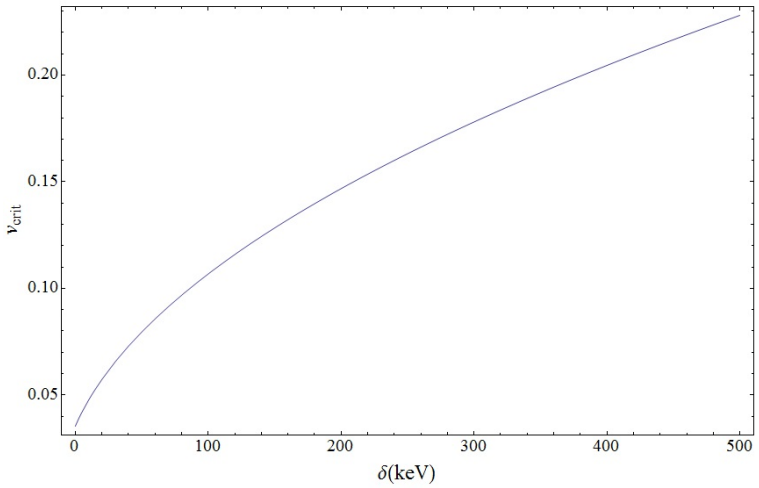

Figure 5.3: The critical velocity plotted against the mass-splitting for a 100 GeV WIMP scattering off a hydrogen atom.

enhancements due to the fact that they are more massive by a factor of at least 10 compared to hydrogen. This factor of mass combined with its large dipole moment means that aluminium is the next most important scattering element, despite it being less abundant than nitrogen by a factor of 40. These effects grow as the inelastic parameter is increased. A larger nuclear mass gives a larger center of mass energy for each scattering event, so the scattering requirement above favors heavier elements. Hydrogen is very quickly deposed from its position as dominant element. For a 100 GeV WIMP the contribution of hydrogen is effectively zero for $\delta \geq 25$keV, with aluminium taking its place and contributing a factor of $\simeq 10$ more than both nitrogen and sodium.

5.2.3 Features of the Dipole-Current cross-section

The dipole-current cross section is more complicated, and has several features of interest from which we can predict the behaviour of the final rates. First, and most simply, the factor of Z^2 gives an enhancement to heavier, less abundant elements. This is especially true of iron, whose large atomic number entirely compensates for its relatively low abundance.

The complex dependence on both recoil energy, which is dependent on velocity, nucleon mass and the inelastic parameter, and the inelastic parameter itself gives rise to several interesting effects in the final rates. To begin with, the overall cross-section is enhanced for higher values of δ. This enhancement competes with the kinematic suppression discussed above. While this enhancement is not sufficient to overpower the kinematic suppression, it slows down the fall-off with increasing δ considerably relative to the dipole-dipole rate.

Finally, a mass-enhancement factor is also present. Although not as strong for high-mass elements as the dipole-dipole mass enhancement, this also serves to increase the importance of the

low-abundance, high-mass elements like iron. The sum of these factors means that all of the elements for whom scattering is allowed by the kinematic requirements contribute roughly equally to the total capture rate (to within an order of magnitude.)

Chapter 6

Form Factors

So far, we have been modelling WIMP-nuclear scattering by assuming the nucleus is a single point particle with a charge and a dipole moment, much like the electron. This assumption holds for low energy scattering, as a low energy process does not "see" the inner structure of the nucleus. The WIMP therefore scatters coherently against the entire nucleus. However, as higher energy WIMPs interact with the nucleus they begin to probe length scales at which the nucleon distribution within the nucleus becomes important.

While scattering off single nucleons is simple to calculate, the scattering off stable composites of nucleons is much more difficult to model theoretically. The solution to this problem is to use experimentally determined "form factors" which parameterize the effect of the inner structure on the scattering[43] . These are normally written as $F^2[E_r]$ and modify the differential cross-section, for example:

$$\begin{aligned}\frac{d\sigma_{DZ}}{dE_r} = \frac{4\pi Z^2\alpha^2}{E_r}\left(\frac{\mu_\chi}{e}\right)^2\left(1-\frac{E_r}{v^2}\left(\frac{1}{2m_N}+\frac{1}{m_\chi}\right)\right.\\ \left.-\frac{\delta}{v^2}\left(\frac{1}{\mu_{N,\chi}}+\frac{\delta}{2m_N E_r}\right)\right)\left(\frac{S_\chi+1}{3S_\chi}\right)F^2[E_r]\end{aligned} \tag{6.1}$$

As outlined in section 5.2, this is also theoretically well-motivated: The nucleus is a composite object, and has some charge and spin distribution due to this fact. This inner structure of the nucleus also effects the total scattering rate, and so we must model this in order to fully simulate scattering. The spin-structure is very different from the charge-structure, and so the dipole-dipole scattering terms require a different form factor to account for this structure.

6.1 Charge Form Factors

If we assume the charge density distribution follows the mass density as $\rho_{charge}(r) = \frac{Ze}{M}\rho(r)$ (for a nucleus with charge Ze and mass M), it is then possible to show that the charge form factor, $F(q)$ is given by

$$F(q) = \frac{1}{M}\int \rho(r) e^{-i\mathbf{q}.\mathbf{r}} d^3r \tag{6.2}$$

[75].

Given this fact, the task of finding the form factor is equivalent to finding the mass density of the nucleus. We compare 4 different mass density profiles here, the simplest example, given by a constant mass density, an exponential form given by Gould, a more complex form derived from the Fermi Gas model of the nucleus, known as the Woods-Saxon model, and the commonly-used Helm Form Factor. The models will be introduced and briefly discussed, then their effects on elastic and inelastic scattering will be demonstrated.

6.1.1 Constant Density Profile

The simplest density model for a nucleus is a solid sphere type model in which the charge density is constant up to some radius, R representing the radius of the nucleus. This gives a form factor given by:

$$|F_{constant}|^2 = \left(\frac{3}{qR} j_1(qR)\right)^2 \tag{6.3}$$

[25].

This model is not very well motivated, as both theory and experiment agree that the nucleus should have some internal structure. In addition, the model has a completely unphysically sharp cut-off at r=R. It will, however, provide a useful benchmark as to the importance of form factors to the indirect detection rate.

6.1.2 Exponential Density Profile

In his original paper on dark matter capture and indirect detection, Gould assumed that the mass density fell of exponentially around the center of mass, giving a form factor as follows[36]:

$$|F_{Gould}|^2 = e^{-\mathbf{q}^2/\mathbf{q}_0^2} \tag{6.4}$$

where q_0 is the characteristic coherence energy, given by $q_0^2 = 3/R^2$, where R is the characteristic charge radius. It is convenient for our simulations to convert these momentum-dependent form factors to recoil energy dependent ones. This is simple to do, as we can just set $E_r = \frac{q^2}{2m_N}$ and $E_0 = \frac{q_0^2}{2m_N}$. [36]

R is different for each element, and is found experimentally [28]. We use the following expression to determine the value for each element:

$$R = 10^{-13}(0.91A^{1/3} + 0.3)\text{cm} \tag{6.5}$$

[57].
While the simplicity of this model is appealing, it is not very well motivated theoretically as theoretical models of the nucleus do not predict an exponential mass distribution. It has also been shown to exhibit features not seen experimentally, and to do poorly at modelling the scattering for heavier elements.[43].

6.1.3 Woods-Saxon distribution

A more theoretically well-motivated model is the Woods-Saxon distribution. This distribution is derived from the Fermi-Gas model, which gives a mass distribution of

$$\rho(r) \propto \frac{1}{e^{(r-c)/a} + 1} \tag{6.6}$$

where c is the "half density radius" and a is proportional to the surface thickness t.[25] This distribution is problematic first because it is not analytically solvable, and must instead be numerically derived for each element. We follow Ozawa et al.[59] and use

$$\begin{aligned} c &= 1.1A^{1/3} \\ a &= 0.54\text{fm} \\ \rho_0 &= 0.17 \text{ nucleon fm}^{-3} \end{aligned} \tag{6.7}$$

where ρ_0 is the constant of proportionality left out of eq. (22).
This has been found to give a good fit to experiments[59] and deviates considerably from the Gaussian distribution at high recoil energies. However, this form is extremely well approximated by the Helm form-factor [29], which has the added benefit of being analytically solvable.

6.1.4 Helm form factor

The Helm form factor was proposed in 1956 as a simpler alternative to the Woods-Saxon form factor. It is derived by combining the mass-density of a uniform sphere with a Gaussian to allow for "softer" edges to the distribution. This gives a form factor as follows:

$$|F_{Helm}(q)|^2 = \left(\frac{3j_1(qR)}{qR}\right)^2 e^{-q^2t^2} \tag{6.8}$$

where R is the effective nuclear radius, and t is the nuclear skin thickness. We follow Lewin & Smith [51] and use

$$R = \sqrt{c^2 + \frac{7}{3}\pi^2 a^2 - 5t^2} \tag{6.9}$$

As in 6.1.3, $c = 1.1A^{1/3}$, $a = 0.54$ fm, which gives $t = 2.4$ fm. We also compare with the values of Lewin & Smith, namely $c = 1.23A^{1/3} - 0.6$, $a = 0.25$ fm, which gives $t = 0.9$ fm[51].

6.1.5 Form Factor Comparison

In order to compare the form factors, they were inserted into the capture calculations (for more information, see chapter 8), and their effect on the capture rate was calculated for WIMP masses of 10, 100, and 1000 GeV for a range of mass-splittings between 0 and 187.5 keV. The result can be seen below in figure 6.1.

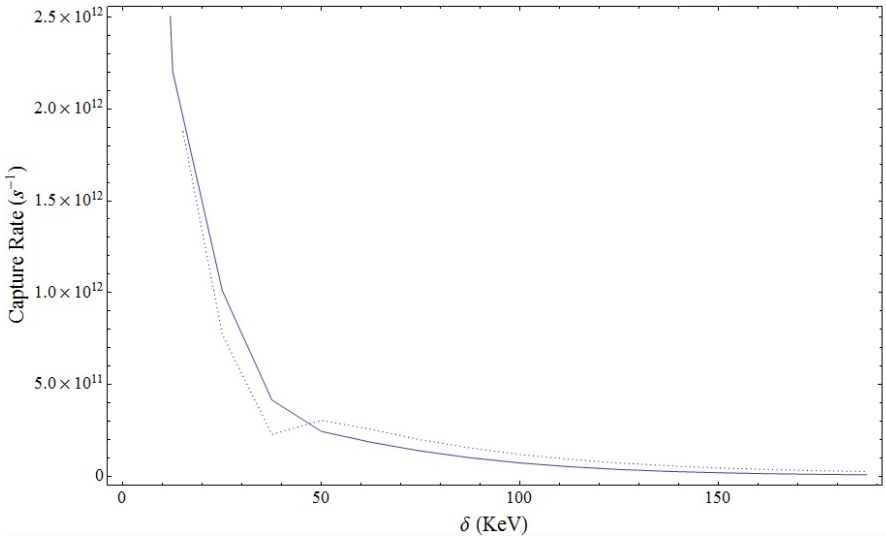

Figure 6.1: The capture rate for a 100GeV WIMP utilizing the Helm form factor (black, dotted) and the exponential form factor (blue, solid).

Chapter 7

Annihilation Channels & Observables

In order for the effects outlined above to be detectable, the WIMPs must annihilate after being captured. As discussed in Chapter 2, the annihilation rate increases as the square of the density of WIMPs increases until an equilibrium is reached. At this point the annihilation rate is equal to half the capture rate, maintaining the number of captured WIMPs at a constant value. This chapter takes this equilibrium as a starting point.

Any given model of WIMP with interactions with the standard model will have annihilations into a variety of standard model particles. In this chapter we discuss in a model-independent way the possible interaction products, their behaviour in the Sun and the possibility of detecting them from Earth. In this chapter we will start by discussing annihilations of the form shown below in figure 7.1, which involves two WIMPs annihilating into two decay products of equivalent energy to the WIMP mass via a virtual photon or a virtual Z-boson.

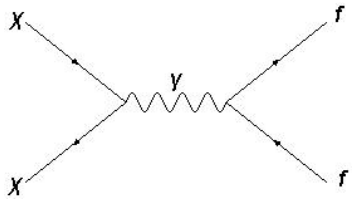

Figure 7.1: Two WIMPs annihilating via a virtual photon or a virtual Z-boson. The two fs represent decay products, the nature of which is discussed below.

7.1 Annihlation Into Leptons

When a matter-antimatter collision occurs, whether between two Standard Model particles or two WIMPs, the annihilation products (that is, the particles that are produced in the annihilation) carry the entire rest mass energy of the original particles with them. Detecting these annihilations therefore, seems like it would be as simple as looking for a mono-energetic signal of the annihilation products. However, it is not so simple. As the annihilation products travel through the medium of the Sun, they will have other interactions. They will scatter and lose energy, they may also annihilate into some new particles, they may decay. Before we can know what a WIMP signal will look like, we have to explore how the passage from the center of the Sun, through the solar material and, finally, to the Earth, will effect the annihilation products. Understanding these processes is key to understanding how to search for WIMP annihilations in the Sun.

7.1.1 Electron-Positron pair production

Any interaction involving the weak charge or the electromagnetic charge will produce (at least some of the time) fermionic annihilation products. Of these, electron-positron pairs are the least useful for our purposes. The Sun's core is filled with ionized electrons and so the positrons completely annihilate, producing photons which scatter off or are absorbed by the nuclei making up the solar core, destroying any signal. Similarly, the core of the Sun is opaque to electrons, capturing or scattering them before any can escape. So the annihilation products themselves cannot be detected.

However, as the electrons move through the Sun it is possible that their interactions produce pions via an interaction with the nucleus. These could either be π^+ via scattering against a proton or π^- via scattering against the neutron. The negatively charged pion, π^-, will get captured very soon after its creation, before it has had a chance to decay, by the nuclei. However, the π^+ will not be absorbed. Instead, it will be slowed and eventually stopped by scattering events and will then decay at rest[19] . Charged pion decay is a very well known process. Its decay is mediated by the weak force and has two dominant channels which account for nearly 100% of decays,

$$\pi^+ \rightarrow \mu^+ + \nu_\mu \tag{7.1}$$

and

$$\pi^+ \rightarrow e^+ + \nu_e. \tag{7.2}$$

The first of these is the dominant channel, occuring 99.988% of the time, with the second channel making up almost all of the rest of the decays [17].

These decays are interesting from the point of view of indirect detcetion for several reasons. Firstly they decay at rest, giving an energy spectrum for the annihilation products which is very well known. Secondly, both decay channels contain neutrinos. Because neutrinos have a very low

interaction cross-section with baryonic matter, almost all neutrinos created in the Sun can escape it without any interactions at all. Therefore Earth-bound detectors can, in principal, detect this well-known spectrum in neutrino searches. Finally, over 99% of the decays result in muon neutrinos. The dominant detection method for solar neutrinos involves the production of muons in the rock of Earth's crust (see chapter 8), which requires the neutrino detected to be of muon type. A decay which produces muon neutrinos is therefore an important source of signal for these detectors. Despite these advantages, pion production is not expected to be an important source of indirect detection data as several factors serve to reduce the usability of this decay. The real setback faced when trying to detect pion decays in the Sun is the energy range. The charged pion has a mass of 139.57 MeV, meaning that the neutrinos produced are in the MeV range. In this range there are several issues to deal with in terms of background noise, which can be somewhat reduced using cuts. However, there is still background to the signal after cuts caused by atmospheric neutrinos and also decays of atmospheric muons. In addition, the range of the resultant muon in the detector is dependent on energy, causing detectors to become less efficient at very low energies. These issues serve to make pion decays hard to search for. However, some work has been done in this area[74] .

7.1.2 Muons and Antimuons

Similarly to pions, muons, μ^-, and antimuons, μ^+ are stopped by scattering in the Sun and decay at rest. Muon decays are simple and take the form[17]

$$\mu^- \rightarrow e^- + \bar{\nu}_e + \nu_\mu \tag{7.3}$$

and

$$\mu^+ \rightarrow e^+ + \nu_e + \bar{\nu}_\mu. \tag{7.4}$$

Again, these decays occur at rest, and so produce a neutrino spectrum in the MeV range, facing the same problems as the pion decay discussed above, but has the advantage of producing muon neutrinos in all decays, raising the potential signal. Interestingly, the muon-decay signal might receive a further enhancement due to the presence of muons in the dominant pion decay channel. These muons will also be stopped and decay at rest. So if pions are produced indirectly by WIMP annihilations, these decays will add to the signal of direct annihilation into muon-antimuon pairs, enhancing this signal. Again, this is not expected to be a particularly fruitful search channel, although some work has gone into placing limits due to this annihilation.[19]

7.1.3 Tau particles

A more promising channel for discovery is annihilation into $\tau^+\tau^-$. The τ particle is a lepton, a heavier cousin of the electron. Due to their higher mass, they are not stopped or slowed as they

travel through the Sun, and decay at their original energy. This means the decay products have energies of order $\sim m_\chi$ rather than the (typically much lower) MeV scale (in this work we consider primarily WIMPs of mass $\sim GeV$). The decay of a τ-lepton is more complicated than the muon's decay as it has enough mass to decay into quarks, and so hadrons can be formed. The dominant four decays of the τ-lepton are listed below with their branching ratio[17] .

$$\tau^- \rightarrow \pi^-\pi^0\nu_\tau \ (25.52\%) \tag{7.5}$$

$$\tau^- \rightarrow e^-\bar{\nu}_e\nu_\tau \ (17.83\%) \tag{7.6}$$

$$\tau^- \rightarrow \mu^-\bar{\nu}_\mu\nu_\tau \ (17.41\%) \tag{7.7}$$

$$\tau^- \rightarrow \pi^-\nu_\tau \ (10.83\%). \tag{7.8}$$

These branching ratios are known to $\sim 0.5\%$ which is sufficiently accurate for our purposes.

These four decays all contain high energy neutrinos, which will reach Earth-bound detectors unnaffected apart from some flavor oscillation. There will also be neutrinos coming from π-meson decay of all three types and also from muon decay. These latter will be stopped in the sun before decay, and so will only produce low energy neutrinos. The main signal will come from the muon neutrinos produced in (7.7) and the tau- and electron-neutrinos which oscillate to muon type en-route to the Earth. This gives a well known energy spectrum of neutrinos to search for, at higher energies than those previously looked at in the chapter.[44] At these higher energies, the sources of background are smaller, and the signal easier to detect as detectors efficiency is partially dependent on energy[70] Please see Chapter 9 for more information on the operations of the detectors.

7.2 Annihilation into Quarks

The possibilities for a WIMP annihilating into quarks depends on its mass. WIMPs under consideration here, that is, with masses of $>$ 1GeV can annihilate into up, down, charm and strange quarks, and those with masses of $>$ 4.2 GeV (that is, the bottom quark mass) can annihilate into bottom quarks. If the WIMP mass is higher than the top mass ($\sim$ 173.07 GeV), it can also create a top anti-top pair. Of these possible annihlation channels, only the charm, bottom and top quarks provide potential detection windows. The lighter quarks (u,d,s) are stopped in the Sun and decay at their rest energies, which are lower than the muon mass and produce very low energy decay products. The charm, bottom and top quarks all hadronize soon after being created. It is predicted that the particles resulting from charm and bottom quark hadronization will be slowed by collisions before decaying, losing a fraction of their energy to this process, while those created by top quarks will have sufficient mass to decay before losing much energy[44].

The important decay for b-quark hadrons is the weak semi-leptonic decay[17],

$$b \to c\mu\nu_\mu. \tag{7.9}$$

While the important decay for c-quark hadrons is

$$c \to s\mu\nu_\mu \tag{7.10}$$

There will therefore be additional neutrinos produced in the bottom-channel by the secondary decay of charm quarks. However, these typically have energy $\sim \frac{1}{3}$ of the energy of the primary decay neutrino, so these are at a lower energy, making their contribution at a lower energy.

The effect of stopping in the Sun can be taken into account using the following approximations (given by Kamionkowski[45])

$$\langle E \rangle \simeq E_c \left[\ln(E_0/E_c) - \gamma_E\right] \text{ for } E_0 >> E_c \tag{7.11}$$

and

$$\langle E \rangle \simeq E_0 \left(1 - E_0/E_c\right) \text{ for } E_0 << E_c \tag{7.12}$$

where E_0 is the hadron's initial energy, E_c is a characteristic energy dependent on the initial quark decay products, and γ_E is Euler's constant . Kamionkowski gives the following estimates for the energy $E_c \simeq 250$ GeV for charm quarks and $\simeq 470$ GeV for bottom quarks. Examining the expressions above, it is easy to see that the energy of the hadrons never gets much higher than E_c. If the WIMP has a sufficiently high mass, it can create top quarks in its annihlations. The only top quark decay known currently is to a W-boson and a down-type quark (that is, a bottom, strange or down quark). The predominant decay of this type is into a bottom quark. The neutrinos produced by the top quark come therefore from the decays of these decay products. The bottom quark decay is discussed above, and the W-decay will be discussed in the next section.

7.3 Annihlation into Gauge Bosons and Asymmetry

7.3.1 W and Z-boson pairs.

Another important channel of the form shown in figure 7.1 occurs for WIMPs with $m_\chi > 80.4$ GeV, that is, with a mass higher than the W-boson mass. In this annihilation channel the products are a W^+W^- pair. These W-bosons will decay into a muon and a muon anti-neutrino (or an anti-muon and a muon neutrino), approximately 10.5% of the time[17].) This produces high energy muons. It can also decay into bottom and charm quarks or τ-leptons, who's secondary decays can produce muon neutrinos as described above. As the initial neutrinos come to us from a direct decay,

with only a relatively low-mass partner, they retain high energies, making this channel an extremely important one for searches[45]. A similar channel is the one which creates Z-boson pairs. Being uncharged, the Z-boson can decay directly into a neutrino anti-neutrino pair, producing two high energy neutrinos. This occurs at slightly higher WIMP mass (as the Z-mass is 91.188 GeV), but produces a similar spectrum to the W^+W^- pair. The Z boson can also decay directly into muon-antimuon and tau-antitau pairs, and also into quark pairs (but not top pairs, as the boson is not sufficiently massive), all of which behave as described above. Of these channels, the direct decay into neutrinos is the most important, producing high energy neutrinos of all three types. At sufficiently high energies, the bosons are not slowed in the Sun, meaning they decay while still having appreciable energy from the annihilation, so the neutrinos are at high energy, especially for high mass WIMPs.

7.3.2 Asymmetry, Photons and Z-Bosons

A factor that has been glossed over so far in discussions of annihilations of the type shown in figure 7.1 is that of asymmetry. For many models, it is the case that the WIMP is either as abundant as its anti-particle, or is its own anti-particle. In these cases, the discussion above is valid. However, in the case where (like normal matter) there is some imbalance between particle and anti-particle these cannot be the dominant annihilations. In the case where the anti-particle is much less abundant and the model allows for no other annihliation channels, the annihilation rate will not yet be large enough to equilibriate with the capture rate, and WIMPs will continue to build up.

In our model, we have a similar problem. In Chapter 3 we stated that our model's interactions were dominantly inelastic, with either a greatly supressed or entirely absent elastic interaction. This means that, in order for the annihilation in fig 7.1 to occur in our model, one of the particles must be in its excited state. The temperature at the center of the Sun is approximately 1.5×10^7 K. This means that a thermalized particle in this region has $E \sim k_B T$, which at this temperature is ~ 1 keV. Unless, therefore, our mass-splitting is smaller than KeV scale, only the highest energy WIMPs will have sufficiently large energy to be in the excited state. The annihilations of the type shown in figure 7.1 are therefore supressed greatly. Instead, the dominant channel becomes the one shown below in figure 7.2

Here, two non-excited WIMPs are annihlating into either two Z-bosons or two photons via a virtual WIMP in the excited state. The Z-bosons then decay as described above, and the photons are absorbed by the Sun. These annihilations into Z-bosons are the most important for putting limits on our model, as they fast become the dominant form of annihilation as δ (the mass splitting) is increased.

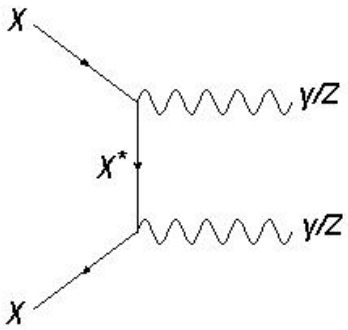

Figure 7.2: Two unexcited WIMPs annihilating into two photons or two Z-bosons via a virtual WIMP in the excited state.

Chapter 8

Calculations and Uncertainties.

8.1 Capture Rate Calculation

Using the methods outlined in Chapter 4, the solar capture rate for inelastic dipole dark matter was calculated for a range of masses and inelastic splittings. The calculations were checked in the case of a constant cross-section against similar calculations performed by Nussinov et al. (Arxiv: 1333v2) and were found to be in agreement. In order to perform these calculations, some assumptions had to be made about scattering within the Sun. The assumptions are outlined below, along with an indication of their effect on the total capture rate (and hence on the limits we place on the model).

8.1.1 Element Abundance

As the scattering cross-section depends on nuclear mass and atomic numbers, scattering against each element must be modelled seperately, with the total capture rate being equal to the sum of the capture rate against each element. In order to simplify our calculations, it was assumed that each element's abundence followed the mass density profile. The individual elemental capture rate was then only dependent on the element's properties and the fractional abundance within the Sun[38].

The effect that this assumption has on the capture rate has not been directly modelled, but it is clear we can safely ignore any uncertainties, for two reasons. Firstly, as outlined below, the uncertainty in the overall mass distribution is non-negligible. Any alteration of an individual elements' distribution would effect the final capture rate a fractional amount compared to this. The uncertainties caused by the difficulty in determining the solar potential render irrelevant the uncertainties caused by this assumption. Secondly, as can be seen in fig 8.1, the majority of capture occurs in the core of the sun. Here, the mass distribution is assumed by almost all models[13] to be flat for all elements. In the dominant volume for capture therefore, the approximation is valid. The elemental abundences are taken from The 8th edition of the 'Table of Isotopes'[30] .

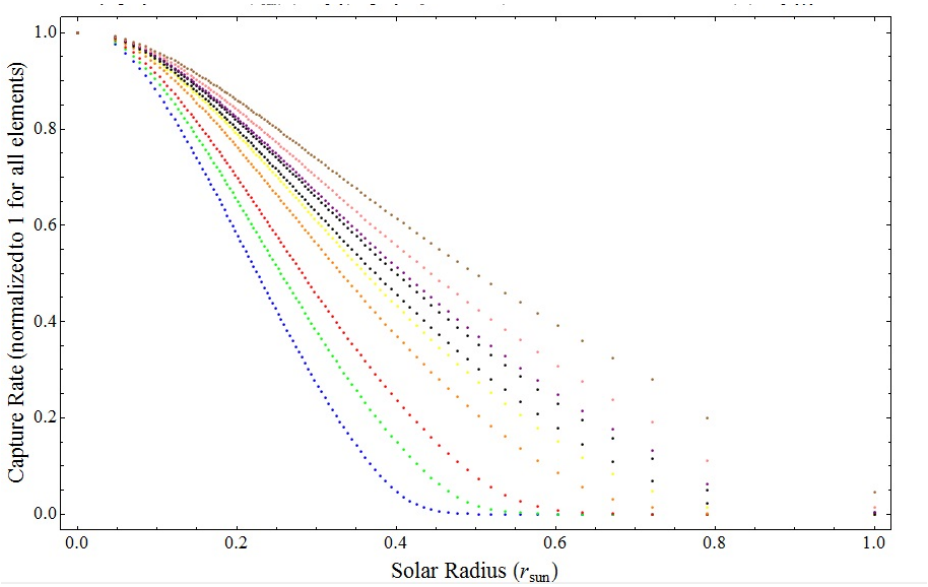

Figure 8.1: Normalized Dark Matter capture rate for each element against energy apart from the two most abundent, helium and hydrogen. The following elements are plotted: Carbon (blue), Nitrogen (green), Oxygen(red), Neon(orange), Sodium (yellow), Magnesium (black), Silicon (Purple), Sulfur (Pink), Argon (brown) Note: Each element has been scaled individually so that it is 1 at the center of the sun. Here m_χ is taken to be 100 GeV and $\delta = 100$.

Figure 8.1 shows that capture for all elements occurs primarily in the core ($r < 0.4$) of the Sun, and therefore the distribution within the core of the Sun is the most important for our calculations. It is interesting to note that the heavier elements (for example Argon) continue to capture at larger r compared to lighter ones. This means that the distribution outside the core will tend to effect capture rates for these nuclei more than for lighter elements. However, these elements are far less abundant than their heavier counterparts, reducing the effect of non-core capture on the total rate.

8.2 Local Velocity Distribution

Several factors combine, including the velocity dependence on the form factor and the need to overcome the inelastic splitting, to make capture rate somewhat sensitive to the local velocity distribution dark matter. In order to make calculations, a form for this distribution must be assumed. In order to discover the dependence of our results on the nature of this assumption, several different popular profiles were tested. These are listed below.

8.2.1 Gaussian Distribution

The simplest assumption to make is that the Dark Matter is a collisionless gas, gravitationally bound in a halo to the galaxy. This gives a Gaussian distribution given by

$$F_{gauss}(v) = \left(\pi v_0^2\right)^{3/2} e^{-v^2/v_0^2} \tag{8.1}$$

where v_0 is the average velocity of the Dark Matter, here given by the sun's velocity relative to the galactic center, which is ~ 200 km/s[67].

Observations, including that of the Bullet Cluster, suggest that Dark Matter is collisionless (http://dianajuncher.dk/files/ba.pdf), however, in order to have a Gaussian distribution as given above, the Dark Matter must also be thermalized. Without collisions, thermalization is difficult, as there are no interactions to distribute energy. However, simulations show that the distribution is roughly similar to the one given in equation 8.1. It is the profile used by both Gould in his original paper and Nussinov et al. in their inelastic dark matter paper[57].

N-Body Simulations

The most useful theoretical tool in determining the Dark Matter distribution is N-body simulations. Here the constituent matter (baryonic and dark) that is thought to make up the galaxy are simulated with as high a resolution as possible. This resolution is normally on the order of $\sim 10^6 M_{Sun}$. The simulation is then run until such a time as it represents the current age of our galaxy, and the resulting distribution of matter is studied. Although dependent on unknown initial conditions and reactions, these simulations have greatly aided in our understanding of local dark matter behaviour[50] .

However, there is disagreement between different simulations. Below we list two profiles found to be in agreement with several simulations each. They have been specifically chosen to be very different from one another, so as to maximize their effect on our capture rate.

8.2.2 Tsallis Distribution

The Tsallis Distribution was found by Ling et al. [52] to fit their Dark Matter + Baryon N-body simulations well. Specifically, a Tsallis q-Gaussian distribution with q=0.77 was found to fit their data. With appropriate normalization, it was shown to be an acceptable velocity distribution for our calculations.

The Tsallis distribution is described by

$$N\left[1 + (1-q)\frac{v^2}{v_0^2}\right]^{\frac{1}{1-q}}, \tag{8.2}$$

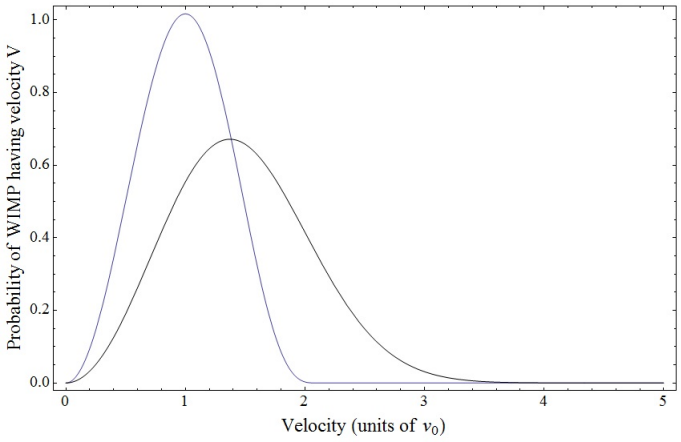

Figure 8.2: The Tsallis distribution (blue) plotted against the standard Gaussian distribution (black). The probability is normalized to one and the velocity is normalized to the mean velocity V_0. Note that the Tsallis distribution is curtailled at a fairly low velocity relative to the Gaussian.

where N is a normalization factor and q is a parameter describing the shape of the curve, set to 0.77 to match Ling et al. It is important to recognise however, that the Tsallis distribution only works for values of $\frac{v^2}{v_0^2}$ which are between the values

$$\pm\frac{1}{\sqrt{1-q.}} \tag{8.3}$$

Outside these limits, the Tsallis distribution is no longer analytic. In our case,$v_0 = 200 - 280km/s$. For the value of q given above, the distribution is only valid up until $|v| = 317.7$ km/s. At this point the Tsallis distribution has reached zero anyway, but it important to note that this distribution cuts off all velocities higher than $\sim 2V_0$, as scattering at high δ depends strongly on the high-velocity tail of the WIMP distribution.

8.2.3 Modified Gaussian Distribution

Green [37] lists several N-body simulations which find that the velocity distribution is well fit by two modified gaussians, one for radial and one for tangential velocities. These distributions are given as follows:

$$f(v_r) = \frac{1}{N_r} Exp[-\langle\frac{v_r}{v_{r0}}\rangle^{\alpha_r}] \tag{8.4}$$

$$f(v_t) = \frac{v_t}{N_t} Exp[-\langle \frac{v_t}{v_{t0}} \rangle^{\alpha_t}] \tag{8.5}$$

As our simple calculations are unable to calculate anisotropic velocity distributions, the tangential velocity distribution was taken and used as an isotropic distribution.

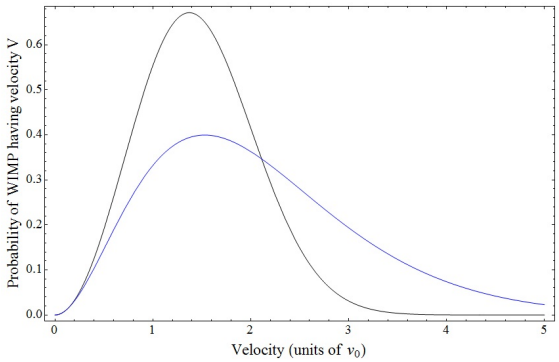

Figure 8.3: The Modified Gaussian distribution (blue) plotted against the standard Maxwellian distribution (black). The probability has been normalized to 1 and the velocity has been nomralized to v_0. Note that the modified Gaussian distribution has a considerably longer high velocity tail.

The distribution was normalized so that it matched the normalization of the Maxwellian distribution. It is clear from *Fig. 2* that this distribution has a significant high velocity tail. It is therefore expected that this distribution will highly overestimate the amount of scattering that occurs. It was simulated both with and without escape velocity cut-off, as a means of demonstrating the importance of this cut-off for certain distributions.

8.2.4 Velocity Comparison

Based on the forms of the distributions seen in figures 8.2 and 8.3, we can assume that the gaussian and modified gaussian distributions will give more similar capture rates than the Tsallis distribution. The Tsallis distribution over-estimates the amount of low velocity WIMPs relative to the standard gaussian distribution, while the modified gaussian has a similar shape to the gaussian distribution, but with an extended high-velocity tail. As discussed in chapter 4, we expect low velocity WIMPs to dominate the capture in the elastic case, but to become quickly irrelevant as the inelastic parameter is increased. We can therefore expect the Tsallis distribution to overestimate capture for the elastic case, but underestimate it for the inelastic case. Conversely, we should expect the modified gaussian to predict less capture than the gaussian in the elastic case, due to the relative under-abundance of low energy WIMPs, but predict more in the highly inelastic cases due to the larger high-velocity tail.

In addition it is clear from the discussion in Chapter 4 that the effects of the inelastic parameter will depend on the mass of the WIMP. Therefore there exist four distinct regimes: low mass & small

mass splitting, low mass & large mass splitting, high mass & small mass splitting, high mass & large mass splitting. We can use the arguments in chapter 4 to predict how changing the velocity distribution will effect the total capture rate. The important effects here will be the following: low-velocity cut-off due to the center of mass (CM) energy of the event dropping below the energy necessary to overcome the mass splitting, which can be written as a condition as follows:

$$\frac{1}{2}\mu\left(u^2+v_e^2\right)>\delta, \tag{8.6}$$

and the high-velocity supression caused by the maximum scattering energy not being sufficiently large to cause capture:

$$\frac{1}{2}m_\chi\left(u^2+v_e^2\right)\left(1-\frac{\mu^2}{m_N^2}\left(1-\frac{m_N}{m_\chi}\sqrt{1-\frac{2\delta}{\mu\left(u^2+v_e^2\right)}}\right)^2\right)<\frac{1}{2}m_\chi u^2. \tag{8.7}$$

The condition outlined in equation 8.4 is easiest to fulfil at high mass. Here, μ (the reduced mass) is large and δ comparitively small, meaning that a wide range of velocities fulfil the condition. We therefore expect that this condition will have little effect for high mass WIMPs. As this condition supresses capture of low velocity WIMPs we expect it to effect the Tsallis distribution more stongly. We can therefore conclude that the Tsallis distribution will over-estimate capture for WIMPs in the elastic limit and for low mass splitting. As the mass splitting increases, the amount by which this over-estimation is supressed is governed by the mass of the WIMP. There will be a higher level of supression for low mass WIMPs and less for high mass WIMPs. This can be seen below in figures 8.4 and 8.5, showing the capture rate for the Tsallis distribution against the standard gaussian at 10GeV (8.4) and at 500GeV (8.5). For the 10 GeV case, condition 8.4 quickly supresses the capture rate for low velocity WIMPs, with the Tsallis distribution causing no capture at all for a mass splitting greater than 125 keV. In contrast, the 500 GeV case shows little drop off with larger splitting. Here, condition 8.4 is unimportant due to the high mass. The Tsallis distribution therefore overestimates the capture rate realtive to the Gaussian distribution for all mass splittings.

Condition 8.4 is also important for the Modified Gaussian distribution. However, in this case its role is to supress the Gaussian distribution's capture relative to the Modified Gaussian's. Once again, this effect is less important in the higher mass case. Condition 8.5 is only noticable at higher mass and higher splitting, as can be seen in the graphs below (figures 8.6 & 8.7) plotting the capture rate for the Gaussian and Modified Gaussian for a 10 GeV and 500 GeV WIMP mass.

8.3 Solar Density

Another important source of uncertainty in our calculations comes from the calculations' dependence on the solar density profile, which is unknown enough such that it introduces some uncertainty

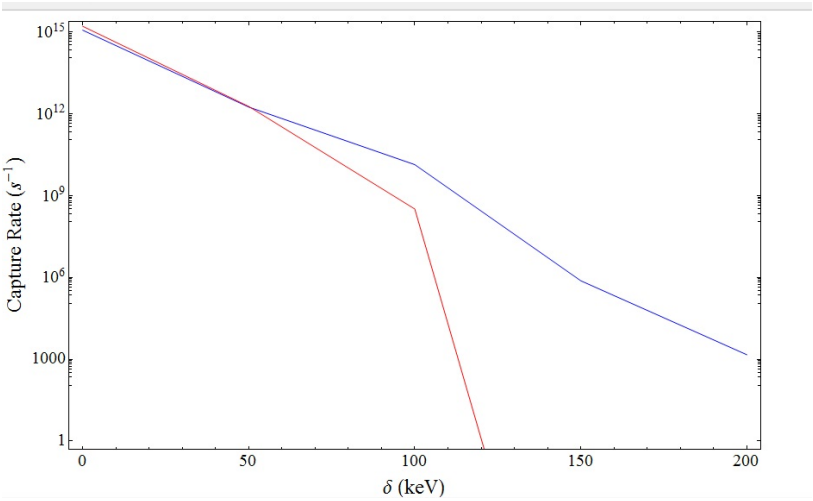

Figure 8.4: [
The capture rate given by the Gaussian distribution (blue) compared to that given for the Tsallis distribution (red) against the mass splitting (δ) for a 10 GeV mass WIMP. Note the drop-off at $\delta = 125$ KeV

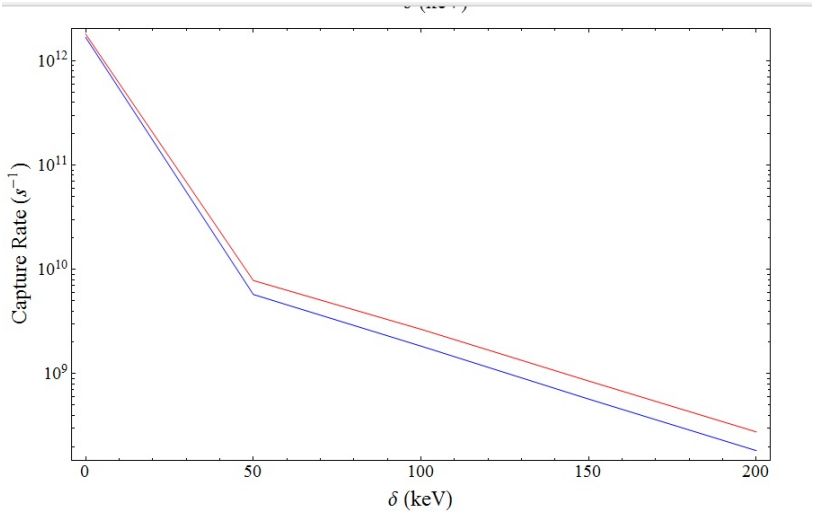

Figure 8.5: The capture rate given by the Gaussian distribution (blue) compared to that given for the Tsallis distribution (red) against the mass splitting (δ) for a 500 GeV mass WIMP.

to the final yield.

In order to estimate the amount of uncertainty introduced by the solar density profile, we used two differing mass profiles for the Sun. One is a numerical profile, used by Nussinov et al.[57]. The second is an analytic profile, given by Henon [42]. The two profiles each describe how the mass interior to a radius r varies with r in a way which is consistent with the Standard Solar Model. We calculated the capture rate of WIMPs given by assuming each of the two profiles and compared them.

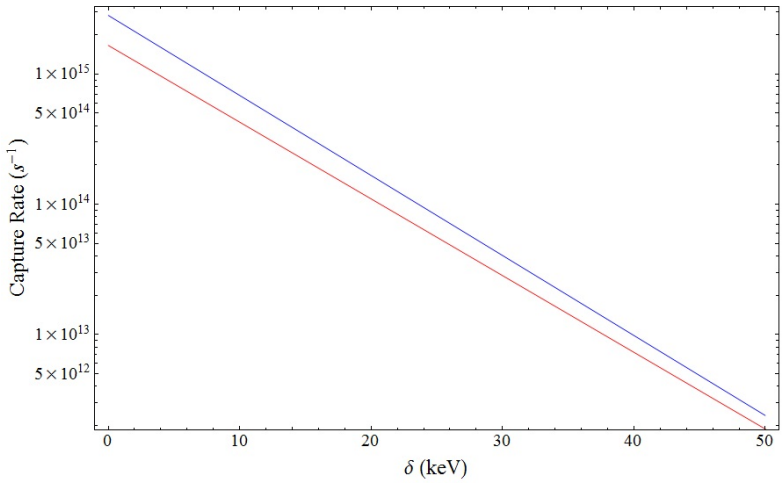

Figure 8.6: The capture rate given by the Gaussian distribution (blue) compared to that given for the Modified Gaussian distribution (red) against the mass splitting (δ) for a 10 GeV mass WIMP.

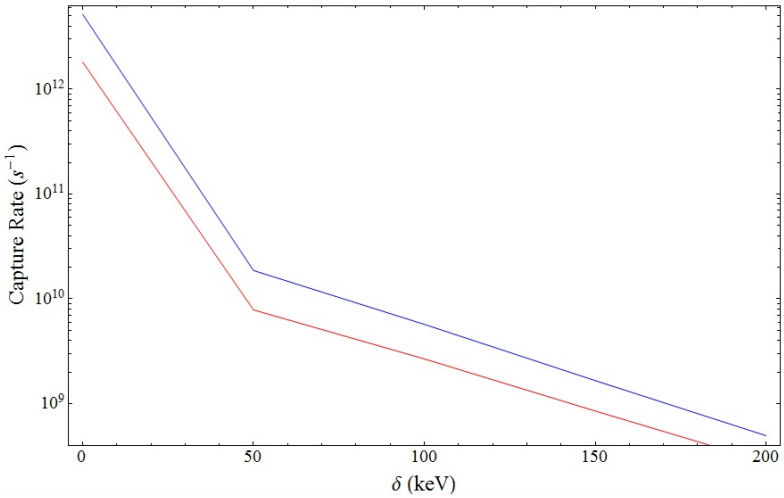

Figure 8.7: The capture rate given by the Gaussian distribution (blue) compared to that given for the Modigied Gaussian distribution (red) against the mass splitting (δ) for a 500 GeV mass WIMP.

The two profiles are plotted in Figure 8.8. While they have the same basic shape, the analytic profile overestimates the core desnity and underestimates the outer density relative to the numerical profile as can be seen in figure 8.8.

The simulation was run for WIMPs of m_χ 110 GeV and 500 GeV in order to quantify the amount of uncertainty in our results caused by this difference.

The results for both masses can be seen below.

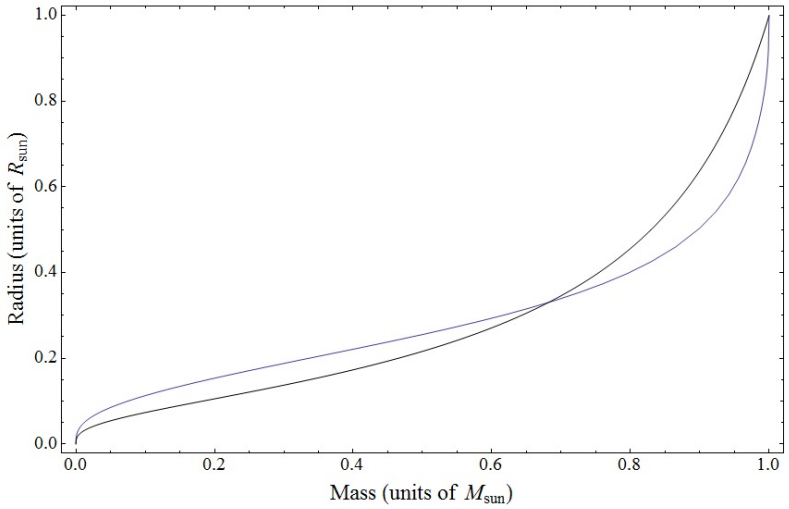

Figure 8.8: The radial distribution of mass in the Sun according to the analytic profile[42] (black) and the numeric profile[57] (blue)

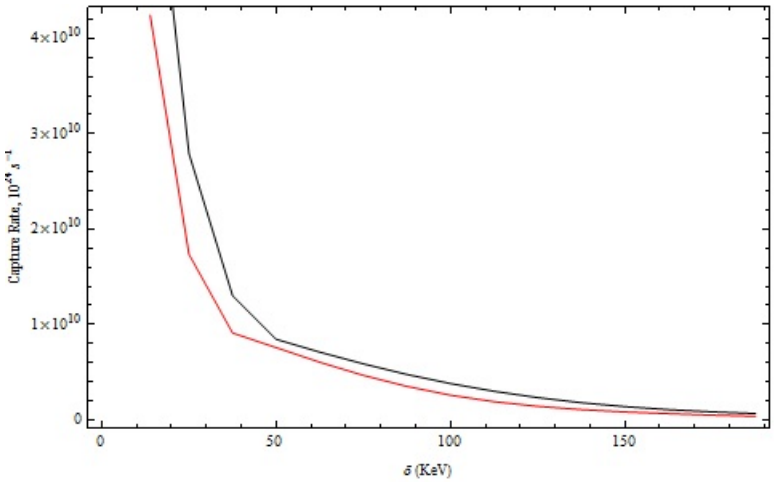

Figure 8.9: Capture rate given the analytic profile (black), and the numeric profile (red) for a WIMP of mass, $m_\chi = 500$ GeV

It is clear from both plots that the analytic profile gives a slightly higher capture rate. This can be traced down to the fact that the analytic profile overestimates the core density, which is where the majority of the capture takes place.

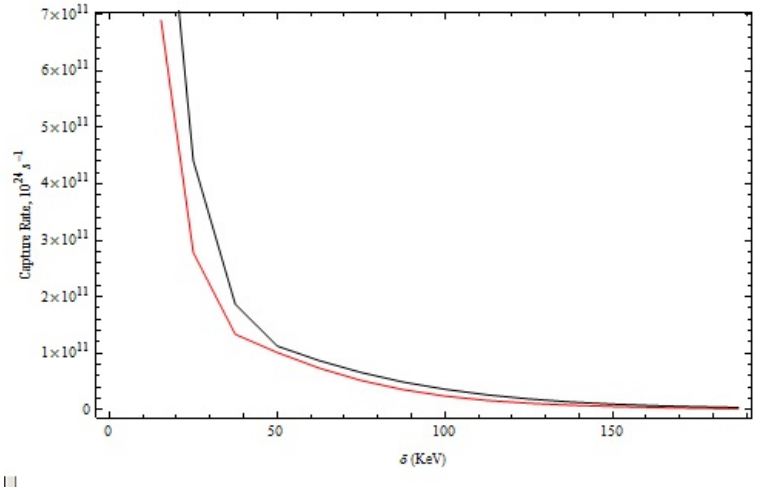

Figure 8.10: Capture rate given the analytic profile (black), and the numeric profile (red) for a WIMP of mass, $m_\chi = 100$ GeV

Chapter 9

DarkSUSY & the Muon Yield

9.1 Detectors

As discussed in chapter 2, there are many methods of direct detection. For the case of capture in the Sun, we are primarily interested in looking for a neutrino excess in the direction of the Sun. For this purpose, we primarily consider the following two experiments: Super-Kamiokande and IceCube/Amanda. Both of these experiments detect muon neutrinos from the products of their charged current interaction in the medium surrounding the detector. In this chapter we discuss the operation of these detectors and the way we calculate the flux of muons due to the WIMP annihilation.

Due to the low interaction cross-sections with ordinary matter, detecting the neutrinos from the dark matter annihilation is a difficult proposition. Detecting them directly would produce such a low count as to be completely impractical for detection in feasible timescales. Several methods, therefore are used to detect these neutrinos, with the most stringent limits given by those detectors configured to detect muons.

The muon-detection method works as follows- The neutrinos are created in the center of the Sun through various channels (see Chapter 7), some of these are electron-neutrinos, some tau- and some muon-, with the fraction of each given by the annihilation channel. The neutrinos propagate towards Earth. As the neutrinos pass through the Earth's crust, some of the muon neutrinos convert into muons through the process depicted in figure 9.1, below.

Muons created in the rock directly surrounding a detector can be detected using their Cerenkov radiation. By tracking these muon's energy the energy of the neutrino can be reconstructed by reconstructing their interaction[67].

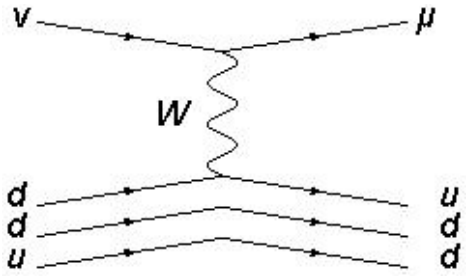

Figure 9.1: Muon production via charged current interaction with a nucleus

9.1.1 Super-Kamiokande

The Super-Kamiokande detector (Super-K) is located in the Kamioka mine in Japan. It consists of 50-ktons of ultra-pure water surrounded by photomultiplier tubes (PMTs) facing both into and out of the detector. Interactions with the rock surrounding the detector (see section below 'Muon Yield' for more details) produce muons at high energies which travel through the detector. This produces Cherenkov light, which is detected by the PMTs. The detector is able to distinguish between electron events and muon events using the shape of the Cherenkov radiation. The direction of the muons can also be determined, and the muon direction is determined by the parent neutrino's direction and the neutrino's energy. This can therefore be used to reduce background as a large source of background is from cosmic ray muons, which are downward going, and so by only considering upward going muons a great deal of these background events are eliminated. This can also be used to determine which muons are coming from the Sun[71].

The experiment can, in principle, detect any muon with enough energy to create Cherenkov radiation. This limit is approximately given by $E_{th} \sim 1.5mc^2$ and so is $E_{th} \sim 157.4$ MeV for muons. In addition to seperating the muons in to up-going and down-going, they also group them into three categories based on their behaviour within the detector: stopping, showering through-going and non-showering through-going. The first category describes those muons which are stopped by interactions in the detector. These are the lowest energy muons detected. The muons in the other two categories both pass all the way through the detector. They are categorized as showering if the event has accompanying radiation, due to radiative energy loss, and non-showering if not. Broadly speaking, showering through-going muons are those with the highest energy. The collaboration then uses filters on each category to reduce the background noise and false-positive data.

While the muon direction is dependent on the parent neutrino direction (strongly so at high energy), it is not an exact indicator. For this reason, in searching for events from the Sun, Super-K do not limit their search to merely the angle subtended by the Sun in the sky. Rather, they use the package WIMPsim, discussed below, to simulate the annihlation of WIMPs into neutrinos, and the subsequent interactions which produce muons. This allows them to calculate the cone half-angle in which they expect more than 90% of WIMP-resultant muons would be found, and search

in there. This is different for each annihilation channel and for each WIMP mass. After removing all those events that do not pass the cuts, then all those events outside of the 90% cone, they analyse the remaining data points in order to quote a 90% CL upper limit on the muon flux from two sample annihilation channels: a "hard" channel, consisting of annihilations into W^+W^- and a "soft" channel, consisting of annilhilations into $b\bar{b}$[70]. As we are primarily interested in other annihilation channels, we will use WIMPSim to somewhat reverse-engineer this process, in order to get limits on our model's cross-section. Please see the section 9.22 for more details.

9.1.2 IceCube/Amanda.

Similarly to Super-K, the IceCube collaboration (and their predecessors AMANDA) rely on Cherenkov radiation to detect muons from neutrino interactions. In this case, however, the medium for both the muon-producing interactions and also the Cherenkov emission is the ice of Antarctica. The IceCube experiment consists of 86 holes, drilled deep into the ice. While the ice close to the surface is opaque, at a depth of $\sim$ 2000 m, it becomes almost as transparent as Super-K's ultra-pure water. It is therefore an excellent medium for creating and transmitting Cherenkov radiation. Into the drilled holes, "strings" of sixty photomultiplier tubes and accompanying data acquisition hardware are deployed. The sheer number of PMTs deployed makes IceCube the largest neutrino telescope in the world. IceCube is predominantly sensitive to high-energy neutrinos.

Again, the IceCube collaboration rejects all downward-going events to try to elimnate cosmic ray muons. They use Monte-Carlo simulation to simulate the background from atomspheric neutrinos. Finally they cut for direction and hit quality. They then use WIMPSim to translate their upper muon flux limit into an upper limit on solar WIMP annihilation rate. As discussed in Chapter 4, this will directly place limits on the capture rate, and hence the WIMP's dipole moment. They quote results from both of their experiments: IceCube, and AMANDA (AMANDA is an earlier version of IceCube, operating on the same pricincipals, but with fewer strings), and also results from both experimental runs combined[2].

9.2 Muon Yield

As discussed above, the data measured by detectors is not in the form of neutrinos directly, but in terms of a resultant muon yield. In order to convert the results quoted by experiments into limits on our model, we require a way of converting from muon yield to neutrino flux. We can then, by looking at the channels described in chapter 7, relate neutrino yield at a given energy to an annihilation rate into a given channel. The process of converting from neutrino to muon yield and back is described below. In practice this calculation is carried out by the set of routines known as WIMPSim.

9.2.1 Muon Yield Calculations

The muon yield in a detector is dependent on the number of muon neutrinos entering the rock, their energy, and the cross-section of the neutrino-rock reaction. This dependence can be categorized as follows:

$$\frac{dN_\mu}{dE_\mu} = A \int_{E_\mu^{th}}^{\infty} dE_\nu \int_0^{\infty} d\lambda \int_{E\mu}^{E\nu} dE'_\mu P\left(E_\mu, E'_\mu, \lambda\right) \frac{d\sigma_\nu(E_\nu, E'_\mu)}{dE'_\mu} \frac{dN_\nu}{dE_\nu} \tag{9.1}$$

Where A is the annihilation rate, E_ν is the energy of the parent neutrino, E'_μ is the initial energy of the created muon, E_μ is the energy of the muon when it is detected; λ is the range of the muon in the medium surrounding the detector (rock or sometimes ice depending on the detector;. P is the probability of a muon of energy E' ending up with energy E after traversing a distance λ; $\frac{d\sigma_\nu}{dE_\mu}$ is the differential cross-section for the reaction described above; and finally, $\frac{dN_\nu}{dE_\nu}$ describes the energy profile of the neutrinos produced in the initial annihilation[17].

Note that this equation only mentions one type of neutrino as only muon neutrinos can create muons in the way described above. However, there is also the possibility of electron or tau neutrinos being created and oscillating into muon neutrinos between the Sun and the detector. To take into account these neutrinos we can write down two similar equations with different annihilation rates and energy profiles and with the addition of a factor $P'_{A\to B}(E_\nu)$ which describes the probability of a neutrino of type A oscilating to a neutrino of type B.

We can conveniently split this equation into those parts depending on the Dark Matter model and those parts depending only on neutrino physics. So far our main effort has been directed towards calculating the annihilation rate A, and it is clear that this parameter is completely controlled by the particular dark matter model in question. In addition the quantity $\frac{dN_\nu}{dE_\nu}$ is also partially controlled by this model. This quanitity is really controlled by the kind of interaction producing the neutrinos. If they are produced directly by annihilation into a Z-boson which decays into $\nu\bar{\nu}$ they will have an energy spectrum determined by the dark matter mass and the kinematics of the annihilation. If, however, they are the result of the decay of a stopped muon they will follow the well known Michel spectrum. The spectrum is determined by the annihilation channel, and the annihilation channels available to a WIMP pair are determined by the Dark Matter model. However, once the annihilation channels have been selected, the quantity is only dependent on the WIMP mass and well-known neutrino physics.

This means that for a given (allowed) annihilation channel, the only quantity in equation 9.1 that is determined by the model is the annihilation rate A. We can therefore calculate the resultant yield for a given channel for a single annihilation, then simply multiply that number by our annihilation rate to get a total muon yield.

The modular nature of this calculation allows us to use DarkSusy to calculate the integrals in (9.1) completely independently of our MiDM model.

9.2.2 DarkSusy and WIMPSim

DarkSusy is a set of fortran routines designed by a collaboration from Utah, Stockholm, Triest and Stanford Universities (DarkSUSY.org). It is desgined to calculate the viability of the supersymmetric dark matter candidate in user-specified models. It contains routines which calculate the production cross-section for WIMPs in colliders, routines which estimate the amount of capture in the sun, etc. Apart from the routines we use to compare to our own calculations, we only use one of DarkSusy's routines, namely the routine designed to calculate the muon yield measured by an Earth-based detector due to solar neutrinos, known as WIMPsim[21].

This routine was modified to accept a dark matter mass and an integer which selects an annihilation channel. For this channel it then returns a number which represents the muon yield per annihilation into this channel, above a certain threshold energy, that is:

$$\frac{N_\mu}{Br_\alpha A} \tag{9.2}$$

where Br is the branching fraction into this channel, and once again A represents the total WIMP annihilation rate. The quantity $Br_\alpha A$ therefore represents the total number of annihilations via the channel α. The energy threshold is determined by the experiments being used to detect the muons.

As shown in chapter 4, the annihilation rate (A) is simply half of the capture rate as the system is in equilibrium. We can therefore use the number calculated by DarkSusy to convert the simulated capture rate into an expected muon yield. By comparing this value to the upper limits on muon yields given by experimental collaborations we can derive a limit on the branching ratio into the channel α for our model.

WIMPsim takes into account both vacuum and matter-driven neutrino oscillations, taking into account the Mikheyer-Smirnov-Wolfenstein (MSW) effect as well as the absorption and regeneration of neutrinos in both the Sun and the Earth. It also takes into account the possibility of neutrinos interacting via charged as both a source of depletion of the number of neutrinos and a source of secondary neutrinos (mainly due to τ production). Finally, it considers the possibility of neutral current interactions as a source of neutrino energy change[21].

Figures 9.2, 9.3 and 9.4 show the muon yield per annihilation, $\frac{N_\mu}{Br_\alpha A}$ for a variety of channels. These are the numbers used to convert from an annihilation rate into a muon yield in order to place constraints on the branching ratio. We assume that the source of uncertainty due to DarkSUSY's calculations is negligible compared to the sources of uncertainty mentioned in Chapter 8.

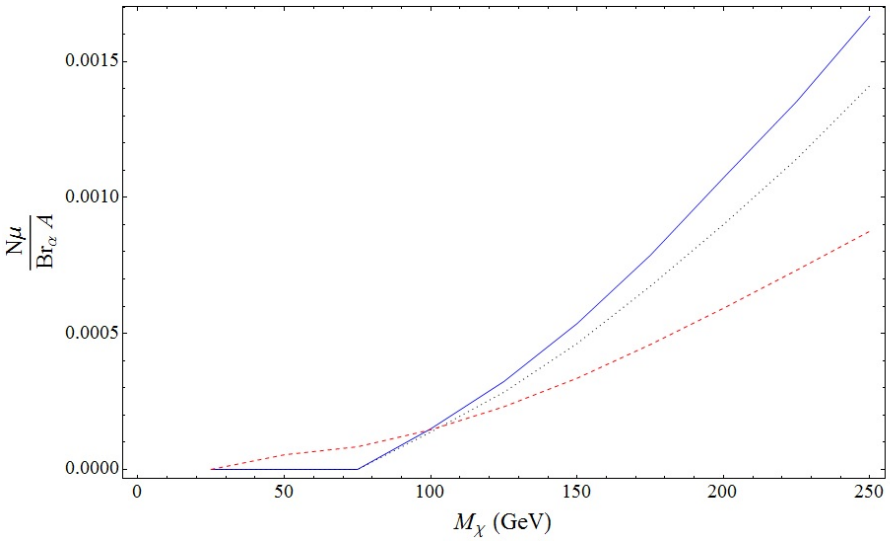

Figure 9.2: The muon yield per annihilation for 3 different annihilation channels, namely ZZ production (blue), W^+W^- production (black, dotted) and γZ production (red, dotted)

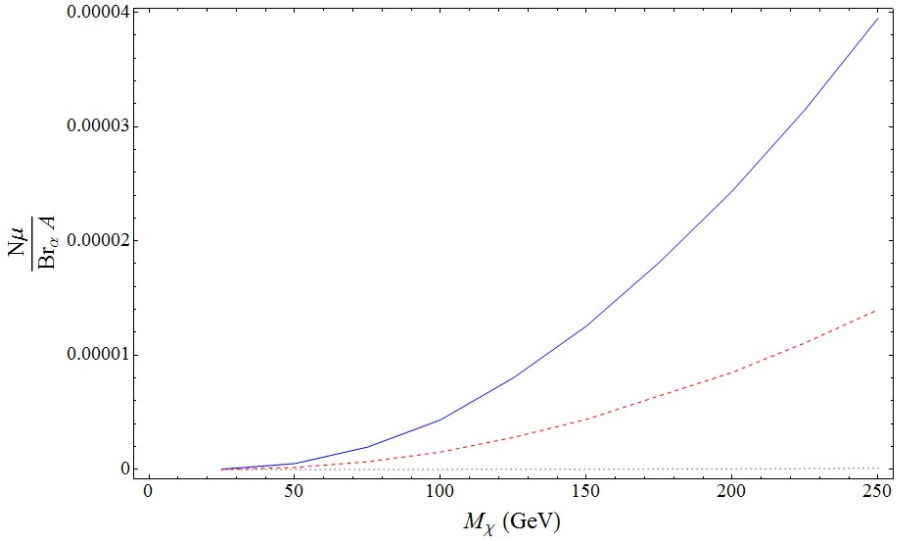

Figure 9.3: The muon yield per annihilation for 3 different annihilation channels, namely $b\bar{b}$ production (blue), $t\bar{t}$ production (black, dotted) and $c\bar{c}$ production (red, dotted)

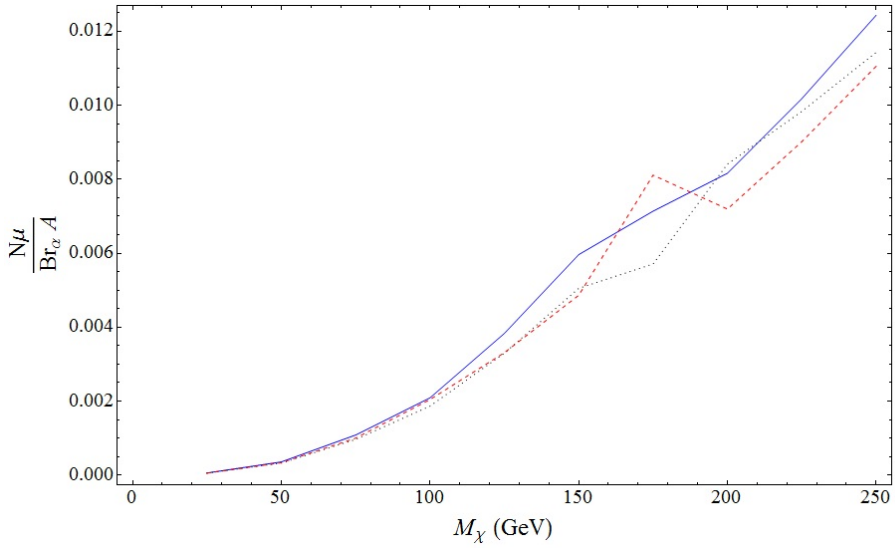

Figure 9.4: The muon yield per annihilation for 3 different annihilation channels, namely $\nu_e\bar{\nu}_e$ production (blue), $\nu_\mu\bar{\nu}_\mu$ production (black, dotted) and $\nu_\tau\bar{\nu}_\tau$ production (red, dotted)

Chapter 10

Results

10.1 Capture Rate

The first and most important thing which was calculated was the expected capture rate in the Sun. This was completed for a range of WIMP masses between 50 and 10,000 GeV, for both the elastic case and the inelastic case with a variety of mass-splittings, ranging from 10 to 250 KeV. This was completed using the methods outlined in chapter 4. These results were then used, with data from the Super-K and IceCube experiments [70, 2] , to place limits on the branching fraction for a given value of dipole moment μ_χ.

For a fixed value of μ_χ, our calculations resulted in the capture rates shown in figures 10.1 and 10.2.

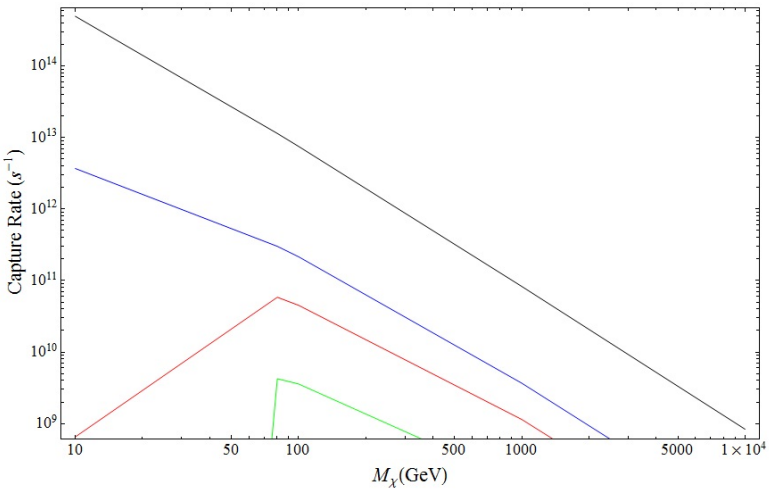

Figure 10.1: The capture rate for a fixed value of μ_χ (=1) against the WIMP Mass for various values of the mass splitting, δ, namely 0 (Black), 50 keV (Blue), 100 keV (Red) and 187.5 keV (Green)

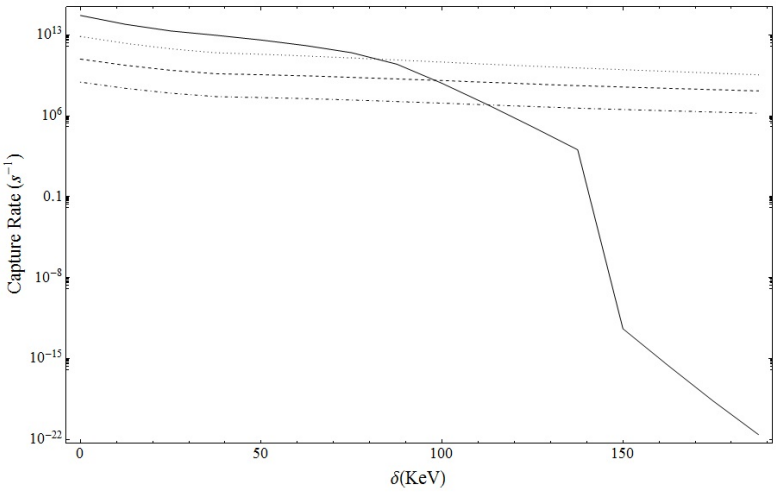

Figure 10.2: The capture rate for a fixed value of μ_χ (=1) against the inelastic paramteter (δ) for various values of WIMP mass, namely 10 GeV (Solid), 100 GeV (Dotted), 1000 GeV (Dashed) and 10,000 GeV (Dot-Dashed)

As can be seen in these figures, both a higher mass and a higher mass-splitting result in a lower capture rate as predicted by the scattering dynamics discussed in Chapter 4. The effect of the inelastic parameter is considerably more drastic at low mass, cutting off the capture almost completely. For higher mass WIMPs, the inelastic parameter effects the rate by several orders of magnitude for a change in δ of only 200 KeV. We can therefore expect to be able to put more stringent limits on the low mass, low mass-splitting case than the high mass or high mass-splitting cases. As outlined in chapter 4, the capture rate saturates before the present era meaning that the annihilation rate is given by $\frac{1}{2}C$ where C is the capture rate. Once a capture rate is calculated therefore, limits can be placed on the model using the data from indirect detection experiments and using the methods outlined in chapter 9.

10.2 Limits from Super-K and IceCube, WW and bb

Note that in the following discussion, a dark matter magnetic moment of $\mu_\chi = 10^{-3}\mu_N$ is assumed. This is obviously not generally true, but as the capture rate scales with μ_χ^2 regardless of mass or inelastic parameter, it is trivial to scale any of the following results to apply to any value of the dark matter moment. Therefore, one should think of the results given below as a limit placed on the combination of branching fraction and dipole given by $Br\left(\frac{\mu_\chi^2}{10^{-6}\mu_N^2}\right)$. Where the branching fraction Br comes from the specific particle physics model chosen.

In order to place general limits on SUSY models, Super-K and IceCube experimental groups both choose two benchmark annihilation products, W^+W^- and $b\bar{b}$ They then perform cuts such that they can quote limits on the branching ratios into these two channels. Using DarkSusy we

can equate this limit to a limit on annihilation rate, and hence capture rate. This limit was then compared to the calculated capture rate to produce a limit on branching ratio for our model. For the elastic case, this places direct constraints on the model. However, in the inelastic case, this matter is complicated by the presence of two states. Annihilation directly into W^+W^- or $b\bar{b}$ requires the interaction shown in figure 10.3.

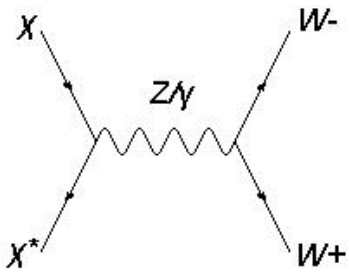

Figure 10.3: Annihilation of a non-excited and an excited WIMP into a pair of gauge bosons.

The dipole interaction requires the presence of both states in order to occur. Thus this kind of interaction is already surpressed for values of the inelastic parameter much larger than $\sim T_{sun}$ which is ~ 2 KeV, due to the fact that the temperature of the thermalized Dark Matter will not be large enough to excite the higher-mass state.

If we assume that the Dark Matter interaction has no elastic component, this interaction will be supressed enough to evade any possible limits we could put on it. For a mass-splitting of just 10 KeV, only $\sim 2\%$ of the thermalized WIMPs would have enough energy to excite the higher-mass state. For 100 KeV, this fraction is effectively zero. In this case therefore, we expect a small branching ratio into these states due to this surpression.

However, if we assume a small elastic component to the interaction, allowing for two lower-mass state WIMPs to annihilate at a supressed rate, the case is different. There is still a supression, but instead of coming from the energy of the particles, it is coming from the fact that the elastic interaction is, itself, supressed. By putting limits on these channels for non-negligible values of the mass-splitting we are really putting limits on the supression of the elastic annihilation of Dark Matter particles. In terms of a purely inelastic dark matter model, the above channels are not the most interesting channels to study. However, they do provide insight into the extent to which the state asymmetry must be present within the Sun.

As can be seen from figures 10.4 and 10.5, the limits put on the inealstic case are less stringent by more than 4 orders of magnitude, meaning the parameter space available for MiDM is much larger than that available to dipole dark matter. Also, as discussed above, heavier WIMPs are less constrained by this method than lighter ones. While these limits are quite stringent, they are really only constraining the highly-supressed elastic component of the interaction in the inelastic case.

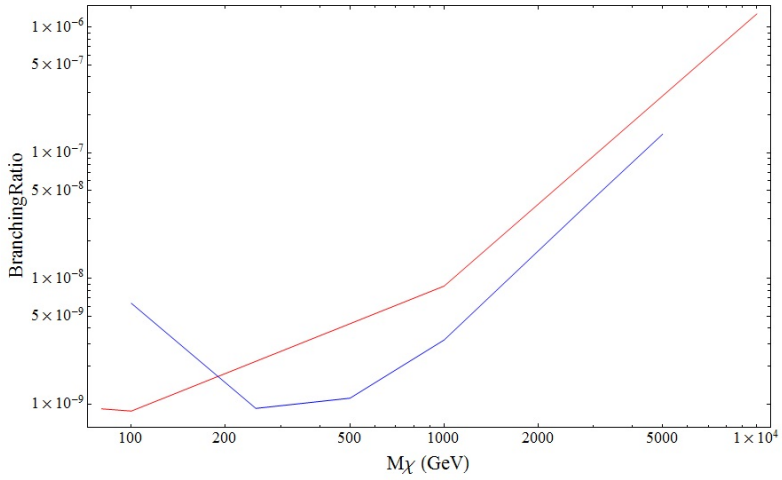

Figure 10.4: Limits on branching ratio for annihilation into W^+W^- bosons from Super-Kamiokande (red) and IceCube (blue) in the elastic case. The total annihilation rate here is assumed to be equal to $\frac{1}{2}$ of the capture rate. As can be seen in figure 10.1 above, the capture rate is much smaller at higher masses. This gives a smaller annihilation rate, and hence a less strong bound on the branching ratio with increasing mass.

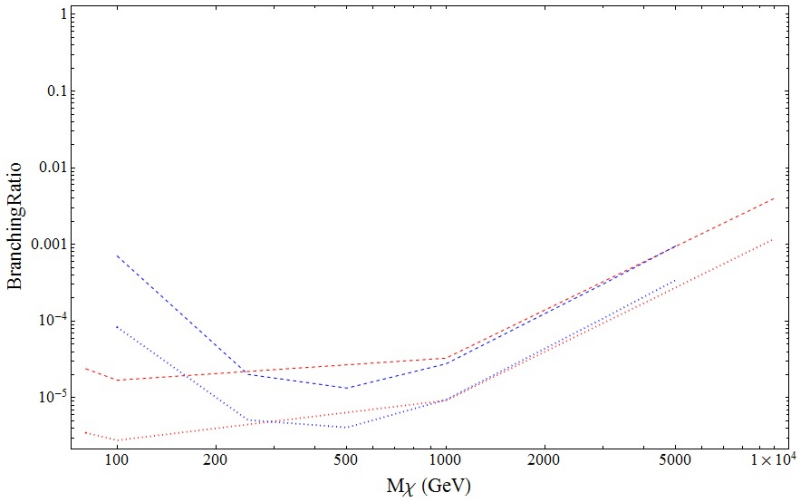

Figure 10.5: Limits on branching ratio for annihilation into W^+W^- bosons from Super-Kamiokande (red) and IceCube (blue) for a mass splitting of $\delta = 125$ KeV (dotted line) and $\delta = 187.5$ KeV (dashed line). These limits are considerably less strong than for the elastic case, due to the previously mentioned supression of the capture rate in the elasic case. This effect can be seen in figure 10.2

10.3 Limits from Super-K and IceCube, Z/γ

As we discuss above, WIMPs are not present in the excited state if the mass-splitting is higher than a few keV. For the inelastic case, therefore, an annihilation channel is needed which allows for two non-excited WIMPs to annihilate with one another. The most important such channel is the

one shown below in figure 10.6 in which two non-excited WIMPS annihilate via a virtual excited state into either a photon and a Z-boson or two photons. As discussed in Chapter 7, the channel containing two photons is undetectable as the Sun is completely opaque to photons, the γZ channel, therefore, is the most important for setting limits on our model. While the ZZ channel will also produce detectable neutrinos, its branching fraction will be $\sim 5\%$ compared to the γZ channel's $\sim 40\%$ (see below for more information), so bounds from this channel will not be as strong.

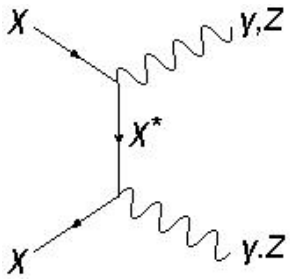

Figure 10.6: The annihilation of two low mass-state WIMPs into a photon and a Z-boson via a virtual high mass-state WIMP

We can use the same method as previously to set limits on this annihilation channel. The following three graphs (figures 10.7, 10.8 and 10.9) show the limits placed on this channel for three different values of the WIMP mass by results from IceCube and Super-K. (Note, IceCube's results to not extend as high as Super-K's, so there is no limit set by IceCube for a $10,000$ GeV WIMP.)

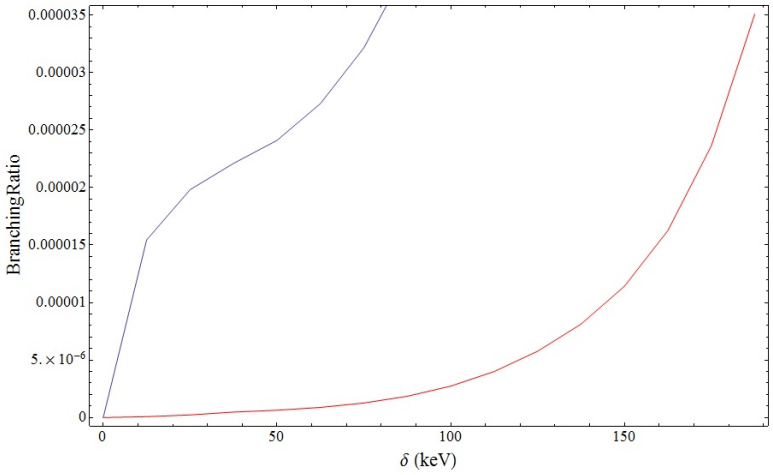

Figure 10.7: Limits placed by Super-K (red) and IceCube (blue) on the branching fraction of annihilation into a photon and a Z boson for a WIMP mass of 100 GeV. Note that, at lower WIMP masses, IceCube does not quote as strong limits, meaning they constrain the parameter space less.

These results place stringent upper limits on the branching ratio into γZ for MiDM dark matter,

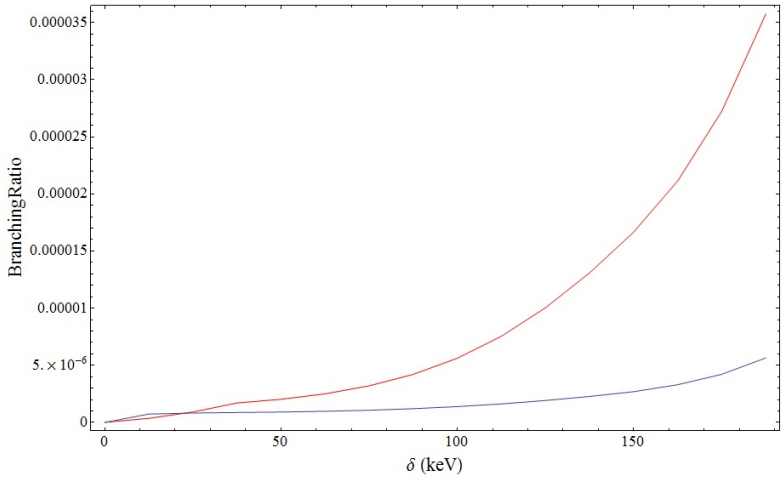

Figure 10.8: Limits placed by Super-K (red) and IceCube (blue) on the branching fraction of annihilation into a photon and a Z boson for a WIMP mass of 1000 GeV.

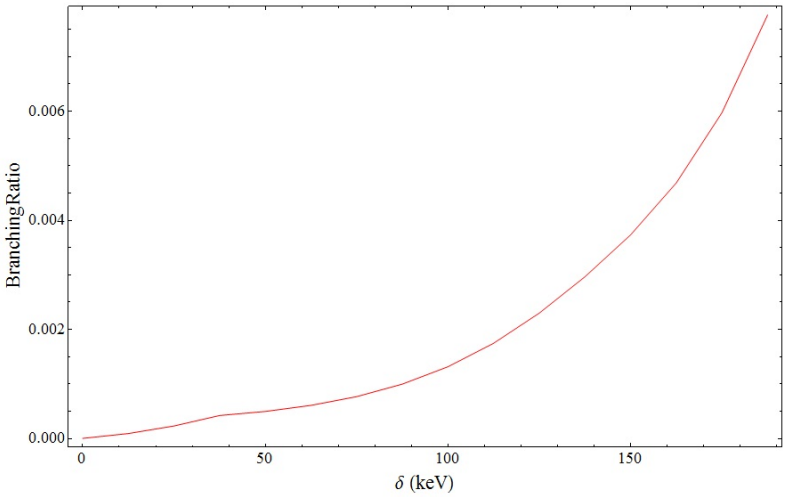

Figure 10.9: Limits placed by Super-K on the branching fraction of annihilation into a photon and a Z boson for a WIMP mass of 10,000 GeV.

with a dipole moment of $\mu_\chi = 10^{-3}\mu_N$. However, in building a model, these limits can always be avoided by simply lowering the value of μ_χ as this is a free parameter, and the capture rate scales with μ_χ^2. Ideally then, we would like to be able to put limits on the parameter space available to μ_χ. In order to do this we need to fix a value for the branching ratio into γZ, given by $\frac{\langle\sigma_{\gamma Z}v\rangle}{\langle\sigma_{tot}v\rangle}$

As discussed above, for values of δ much larger than $\sim$ 2 keV, the excited WIMP state is completely absent in the Sun. This means that only interactions involving two unexcited WIMPs can contribute to the annihilation rate. At first order in the couplings, the only such annihilations available are those of the form shown in figure 10.6. This means that $\langle\sigma_{tot}v\rangle = \langle\sigma_{\gamma\gamma}v\rangle + \langle\sigma_{\gamma Z}v\rangle + \langle\sigma_{ZZ}v\rangle$. Following Weiner and Yavin. (2012)[72] , we assume that the coupling to the Z-boson comes

entirely from electroweak mixing, and hence is simply given by

$$-\frac{1}{2}t_W \mu_\chi \bar{\chi}\sigma_{\mu\nu}\chi^* Z^{\mu\nu}. \tag{10.1}$$

This gives the following expressions for the annihilation cross-sections:

$$\langle\sigma_{\gamma\gamma}v\rangle = \frac{(m_\chi+\delta)^2\,\mu_\chi^4}{\pi\left(1+\frac{(m_\chi+\delta)^2}{m_\chi^2}\right)^2}, \tag{10.2}$$

$$\langle\sigma_{ZZ}v\rangle = \frac{m_\chi^2\left(1-\frac{m_z^2}{m_\chi^2}\right)^{3/2}\tan^4\theta_W\left(\frac{m_z^2}{2m_\chi^2}-\frac{m_\chi+\delta}{m_\chi}\right)^2\mu_\chi^4}{4\pi\left(\frac{1}{2}\left(1+\frac{(m_\chi+\delta)^2}{m_\chi^2}\right)-\frac{m_Z^2}{2m_\chi^2}\right)}, \tag{10.3}$$

$$\langle\sigma_{Z\gamma}v\rangle = \frac{m_\chi^2\left(1-\frac{m_z^2}{4m_\chi^2}\right)^{3}\tan^2\theta_W\left(\frac{m_z^2}{4m_\chi^2}-\frac{m_\chi+\delta}{m_\chi}\right)^2\mu_\chi^4}{2\pi\left(\frac{1}{2}\left(1+\frac{(m_\chi+\delta)^2}{m_\chi^2}\right)-\frac{m_Z^2}{4m_\chi^2}\right)}. \tag{10.4}$$

where θ_W is the Weinberg angle and m_Z is the mass of the Z boson. We use the following values $\theta_W = 0.511621$ (radians), $m_Z = 91.1876$ GeV[17] . Using these expressions, we determine an expression for $\frac{\langle\sigma_{ZZ}v\rangle}{\langle\sigma_{tot}v\rangle}$. This gives us a value for the branching fraction at each mass point and value of the mass splitting, δ. For a 100 GeV WIMP with a mass splitting of 100 keV, the fraction is 0.411914. Multiplying our capture rate by the fraction at each data point gives us the annihilation rate into γZ in terms of the dipole coupling μ_χ exclusively. This means that limits placed above on the Branching Ratio can be converted into limits on the dipole coupling for our model. These results can be seen below in figures 10.10,10.11 and 10.12.

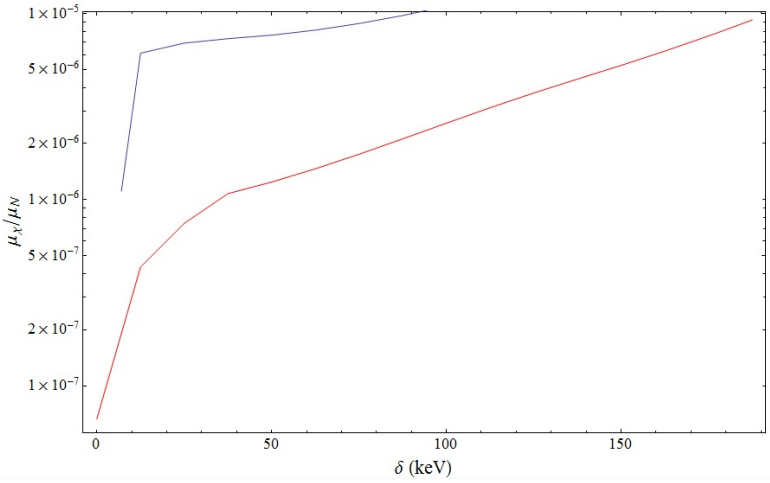

Figure 10.10: Limits placed by Super-K (red) and IceCube (blue) on the dipole moment of a 100 GeV WIMP.

These limits are several orders of magnitude stronger than those placed on the model from direct

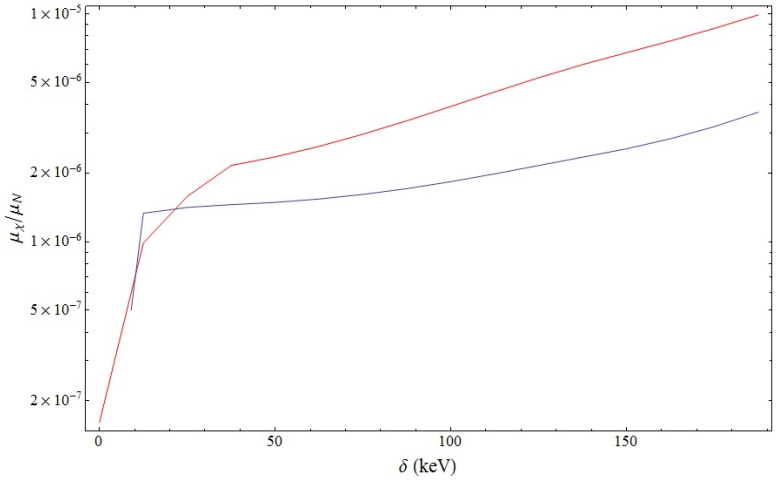

Figure 10.11: Limits placed by Super-K (red) and IceCube (blue) on the dipole moment of a 1000 GeV WIMP.

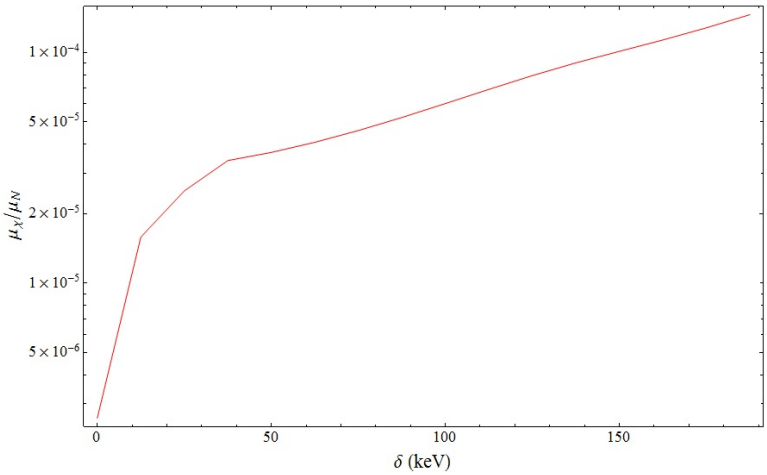

Figure 10.12: Limits placed by Super-K on the dipole moment of a 10,000 GeV WIMP.

detection, which are typically of order $\sim 10^{-3}$.

10.3.1 Equilibrium with reduced annihilation

As stated in chapter 4, all the results above assume that the annihilation rate has saturated at $\frac{1}{2}C$ (see equations 4.18-4.20). However, this is only the case if the equilibrium time, given by $\tau_{eq} = (C_c C_A)^{-1/2}$ is smaller than the age of the Sun. However, once we reduce the number of annihilation channels available to the WIMP, as we have done in the preceeding section, we reduce the annihilation cross-section. This increases the equilibrium time. For a sufficiently large reduction of the annihilation cross-section, the annihilation rate is no longer saturated, and is instead given by $\gamma_A = \frac{1}{2}C_c \tanh^2(t/\tau_{eq})$ [57]. For the cross-sections given in equations 10.2 to 10.4, this is the

case. This means that the annihilation rates used to produce the graphs shown in figures 10.10-10.12 are actually supressed by a factor of $\tanh^2(t/\tau_{eq})$. This can be calculated by following Jungman et al.[44], using their equation

$$\frac{t}{\tau_{eq}} = 330 \left(\frac{C}{s^{-1}}\right)^{1/2} \left(\frac{\langle \sigma_A v \rangle}{cm^3 s^{-1}}\right)^{1/2} \left(\frac{m_\chi}{10GeV}\right)^{3/4}. \tag{10.5}$$

This supression factor makes it slightly complex to place limits on the value of μ_χ due to the fact that it now appears in our calculations both inside (via σ_A and C) and outside (via C) the function tanh. However, because the numerical value of the factor t/τ_{eq} is very small in the cases we are examining (< 0.01), we can use the approximation $\tanh(x) \approx x$. This makes our equation easier to handle. The predicted annihilation rate now changes from being dependent on μ_χ^2 (these two factors coming from the capture rate) to being dependent on μ_χ^8, with two factors coming, again, from the overall capture rate, and the other six factors coming from the expression in 10.5 which is inside of the tanh function and subsequently squared. This changes the shape of the exclusion plots. The new plots can be seen in Figures 10.13. These limits, although much less competitive, are more robust than those placed at the beginning of this section as they do not rely on assumptions about alternative annihilation states.

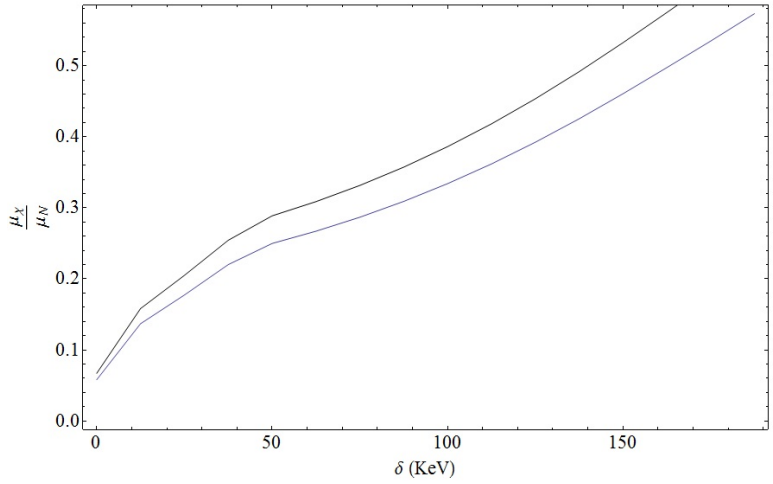

Figure 10.13: Limits placed by Super-K on the dipole moment of a 100 GeV WIMP, in the case where equilibrium is not reached.

However, it is not necessarily true that the only annihilation states available to WIMPs are those discussed in chapter 7. It is possible that the dipole moment could be due to a dark sector interaction (see chapter 3), and therefore annihilations could occur into this dark sector. If this annihilation channel has a large enough cross-section, it can lower the equilibrium time and thus the annihilation rate can saturate. We do not know what the annihilation cross-section will be in this case without

making some assumptions about the model, but we can explore the effect this scenario would have on our limits by assuming a total annihilation cross-section. In the case where the annihilation rate is saturated, the only quantity that will depend on the annihilation cross-section is the branching ratio, which depends on the total annihilation cross-section. It is therefore simple to extrapolate our calculations to any model of dark sector annihilations by simply scaling to the total cross-section given for each model.

For illustrative purposes we will use the velocity-averaged annihilation cross-section required for relic abundance (see chapter 2), namely $3 \times 10^{-26} cm^3/s$. It can be seen that this cross-section is sufficiently large to saturate the annihilation rate by substituting it into equation 10.5. Note that this cross-section is chosen for illustrative purposes only: The annihilation channels responsible for relic abundance in the early universe are unlikely to be the same as those responsible for annihilation in the Sun. In the early universe, temperatures are high enough to easily excite the higher mass state, so that processes such as that shown in figure 7.1 are allowed. However, as discussed above, the temperature in the Sun is much too low for this to occur for anything but the smallest mass-splittings.

Using this annihilation cross-section annihilation cross-section we can calculate the branching fraction into $\gamma - Z$ as before and place bounds on μ_χ using the IceCube and Super-K data. These results are shown in figure 10.14.

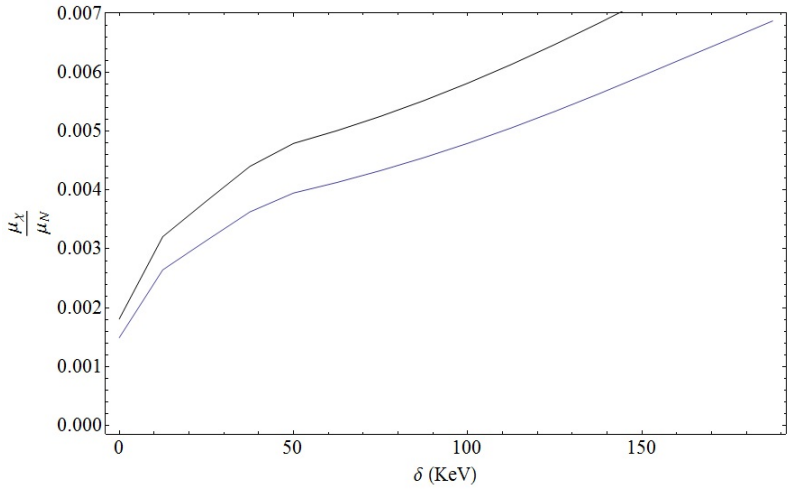

Figure 10.14: Limits placed by Super-K on the dipole moment of a 100 GeV WIMP, with a total annihilation cross-section of $\langle \sigma_A v \rangle = 3 \times 10^{-26} cm^3/s$.

10.4 Conclusions and Future Work

As can be seen from figures 10.10-10.14, solar capture can be used to place useful limits on magnetic inelastic models of dark matter under various scenarios. In the cases where equilibrium between capture and annihilation is reached, these limits are competitive with those set by direct detection [57]. In this work we have put competitive constraints on the model using annihilation into the γZ channel in the case where equilibrium is reached.

The main source of uncertainty in our calculations comes from the uncertainty in the local velocity distributions (see chapter 8), which also effects direct detection. Other calculational sources of uncertainty, such as form factors, uncertainty in neutrino oscillation and muon yield, are less important.

The work presented in this thesis can be expanded in a number of ways. The most obvious of these being examining exothermal interactions, that is, where the inelastic parameter is negative, meaning the initial state of the WIMP is at higher energy than the 'excited' state. This possibility can be explored using many of the same methods as utilized in this work. Another simple extension is discussed by Kouvaris & Tinyakov [48]. Here, capture is calculated in an identical way, but with parameters describing the progenitors of compact stars such as white dwarfs and neutron stars. Limits can then be placed on the model by calculating the upper mass limit of these stars before a black hole is formed. By comparing with observation, we can place limits on how much capture can occur given the mass of observed compact stars. This technique is most effective at higher mass.

A more complete picture of the limits placed on MiDM via these methods could also be obtained by extending the calculations down to lower WIMP masses. At lower mass, some of the scattering within the Sun (after capture), would give the scattered WIMP sufficient velocity to escape the Sun's potential well. This 'evaporation' would have to be carefully calculated, as it serves to reduce the annihilation rate significantly for low mass WIMPs [44].

Finally, a more ambitious extension of this work would be a generalization of the principals within to other models, including electric dipole models, Rayleigh dark matter and dark dipole models [72].

Appendix A

Elemental properties

Element Name	Z	A	Mass (GeV)	Fractional Abundance	Magnetic Dipole (μ_N)	Spin
H	1	1	0.938712	0.67	2.79285	$\frac{1}{2}$
He	2	4	3.72769	0.311	0	0
C	6	12	11.1858	0.00237	0	0
N	7	14	13.0447	0.00188	0.403761	1
O	8	16	14.9005	0.00878	0	0
Ne	10	20	18.7937	0.00193	0	0
Na	11	23	21.4107	0.000039	2.21752	$\frac{3}{2}$
Mg	12	24	22.6357	0.000733	0	0
Al	13	27	25.1283	0.000064	3.6415	$\frac{5}{2}$
Si	14	28	26.1565	0.000798	0	0
S	16	32	29.8627	0.00055	0	0
Ar	18	40	37.2043	0.00008	0	0
Ca	20	40	37.3253	0.000073	0	0
Fe	26	56	52.0094	0.00142	0	0
Ni	28	59	54.6622	0.000084	0	0

Bibliography

[1] C E et al. Aalseth. Results from a Search for Light-Mass Dark Matter with a p-Type Point Contact Germanium Detector. *Physical Review Letters*, 106(13):131301, March 2011.

[2] M. G. et al. (IceCube collaboration Aartsen. Search for Dark Matter Annihilations in the Sun with the 79-String IceCube Detector. *Physical Review Letters*, 110(13):131302, March 2013.

[3] P.A.R. Ade et al. Planck 2013 results. I. Overview of products and scientific results. 2013.

[4] R Agnese, SW Leman, M Pepin, and M Kiveni. Silicon Detector Results from the First Five-Tower Run of CDMS II. pages 1–5, 2013.

[5] Z. AHMED. RECENT RESULTS FROM WIMP-SEARCH ANALYSIS OF CDMS-II DATA. In *Physics Beyond the Standard Models of Particles, Cosmology and Astrophysics - Proceedings of the Fifth International Conference - Beyond 2010*, pages 530–536, Singapore, 2011. World Scientific Publishing Co. Pte. Ltd.

[6] Dmitry Akimov. Techniques and results for the direct detection of dark matter (review). *Nuclear Instruments and Methods in Physics Research Section A: Accelerators, Spectrometers, Detectors and Associated Equipment*, 628(1):50–58, February 2011.

[7] Andrea Albert. Search for Gamma - ray Spectral Lines in the Milky Way Diffuse with the Fermi Large Area Telescope Spectral Lines from WIMP annihilations. *Talk- Fourth International Fermi Symposium*, 2012.

[8] C et al. Alcock. The MACHO Project: Microlensing Results from 5.7 Years of Large Magellanic Cloud Observations. *The Astrophysical Journal*, 542(1):281–307, October 2000.

[9] G. W. Angus, B. Famaey, and H. S. Zhao. Can MOND take a bullet? Analytical comparisons of three versions of MOND beyond spherical symmetry. *MNRAS*, 371:138–146, September 2006.

[10] E. Aprile and T Doke. Liquid xenon detectors for particle physics and astrophysics. *Reviews of Modern Physics*, 82(3):2053–2097, July 2010.

[11] E. Aprile et al. Dark Matter Results from 225 Live Days of XENON100 Data. *Phys.Rev.Lett.*, 109:181301, 2012.

[12] K. Babu, R. Schaefer, and Q Shafi. Cold plus hot dark matter cosmology in the light of solar and atmospheric neutrino oscillations. *Physical Review D*, 53(2):606–617, January 1996.

[13] JN Bahcall. Solar models: Current epoch and time dependences, neutrinos, and helioseismological properties. *The Astrophysical Journal*, 555(990), 2001.

[14] X Bai, A J Bailey, J Balajthy, S Bedikian, E Bernard, A Bernstein, A Bolozdynya, A Bradley, D Byram, S B Cahn, C Chan, J J Chapman, A A Chiller, C Chiller, K Clark, T Coffey, A Currie, and A Curioni. First results from the LUX dark matter experiment at the Sanford Underground Research Facility.

[15] J Baron, WC Campbell, and D DeMille. Order of Magnitude Smaller Limit on the Electric Dipole Moment of the Electron. *arXiv preprint: 1310.7534v1*, pages 1–8, 2013.

[16] D P Bennett, C Alcock, R A Allsman, T S Axelrod, C W Stubbs, W Sutherland The, and Macho Collaboration. The MACHO Project Dark Matter Search. *arXiv preprint: 9510104*, 1995.

[17] et al. (Particle Data Group Beringer, J. Review of Particle Physics. *Physical Review D*, 86(1):010001, July 2012.

[18] R Bernabei, P Belli, A Di Marco, Tor Vergata, I Rome, Dip Fisica, Roma La, C J Dai, H L He, X H Ma, X D Sheng, and R G Wang. DAMA / LIBRA results and perspectives. pages 1–12, 2013.

[19] N Bernal, J Martin-Albo, and S Palomares-Ruiz. A novel way of constraining WIMPs annihilations in the Sun: MeV neutrinos. *arXiv preprint: 1208.0834v1*, pages 1–11, 2012.

[20] Gianfranco Bertone. The moment of truth for WIMP dark matter. *Nature*, 468(7322):389–93, November 2010.

[21] Mattias Blennow, Joakim Edsjö, and Tommy Ohlsson. Neutrinos from WIMP annihilations obtained using a full three-flavor Monte Carlo approach. *Journal of Cosmology and Astroparticle Physics*, 2008(01):021, January 2008.

[22] Jo Bovy and Scott Tremaine. ON THE LOCAL DARK MATTER DENSITY. *The Astrophysical Journal*, 756(1):89, September 2012.

[23] Spencer Chang, Neal Weiner, and Itay Yavin. Magnetic Inelastic Dark Matter. *arxiv preprint*, 95616:8, July 2010.

[24] M. Cozzi. New limits on magnetic monopoles searches from accelerator and nonaccelerator experiments. *Physics of Atomic Nuclei*, 70(1):118–122, January 2007.

[25] Gintaras D?da, Ann Kemper, and Paolo Gondolo. Model-independent form factors for spin-independent neutralino?nucleon scattering from elastic electron scattering data. *Journal of Cosmology and Astroparticle Physics*, 2007(04):012–012, April 2007.

[26] S et al. (Super-K Collaboration) Desai. Search for dark matter WIMPs using upward through-going muons in Super-Kamiokande. *Physical Review D*, 70(8):083523, October 2004.

[27] MJ Duncan, JA Grifols, A Mendez, and S Uma Sankar. Restrictions on the neutrino magnetic dipole moment. *Physics Letters B*, (June):304–308, 1987.

[28] G. Eder. *Nuclear Forces: Introduction to Theoretical Nuclear Physics*. M.I.T. Press, 1968.

[29] J. Engel. Nuclear form factors for the scattering of weakly interacting massive particles. *Physics Letters B*, 264(1-2):114–119, July 1991.

[30] R.B. Firestone. *1998 Update to the 8th Edition*. John Wiley & Sons, Inc., 1998.

[31] G. GAMOW. The Evolution of the Universe. *Nature*, 162(4122):680–682, October 1948.

[32] Katherine Garrett and G D?da. Dark matter: A primer. *Advances in Astronomy*, pages 1–27, 2010.

[33] Germán A Gómez-Vargas, Miguel A Sánchez-Conde, Ji-haeng Huh, Miguel Peiró, Francisco Prada, Aldo Morselli, Anatoly Klypin, David G Cerdeño, Yann Mambrini, and Carlos Muñoz. Constraints on WIMP annihilation for contracted dark matter in the inner Galaxy with the Fermi -LAT. *Journal of Cosmology and Astroparticle Physics*, 2013(10):029–029, October 2013.

[34] Paolo Gondolo and Joseph Silk. Dark Matter Annihilation at the Galactic Center. *Physical Review Letters*, 83(9):1719–1722, August 1999.

[35] Anthony H Gonzalez, Maxim Markevitch, and Douglas Clowe. A direct empirical proof of the existence of dark matter. 2002.

[36] Andrew Gould. Resonant enhancements in weakly interacting massive particle capture by the earth. *The Astrophysical Journal*, 321(February):571, October 1987.

[37] Anne M Green. Dependence of direct detection signals on the WIMP velocity distribution. *Journal of Cosmology and Astroparticle Physics*, 2010(10):034–034, October 2010.

[38] N Grevesse and AJ Sauval. Standard solar composition. *Space Science Reviews*, 1998.

[39] Kim Griest and P Murdin. WIMPs and MACHOs Encyclopedia of Astronomy & Astrophysics. pages 0–6, 2006.

[40] Kim Griest and David Seckel. Cosmic asymmetry, neutrinos and the sun. *Nuclear Physics B*, 283:681–705, January 1987.

[41] Steen Hannestad, Alessandro Mirizzi, Georg G Raffelt, and Yvonne Y.Y Wong. Neutrino and axion hot dark matter bounds after WMAP-7. *Journal of Cosmology and Astroparticle Physics*, 2010(08):001–001, August 2010.

[42] M. Hénon. L'amas isochrone. - III. Fonction de distribution. *Annales d'Astrophysique*, 23:474, February 1960.

[43] Robert Hofstadter. Electron Scattering and Nuclear Structure. *Reviews of Modern Physics*, 28(3):214–254, July 1956.

[44] Gerard Jungman and Marc Kamionkowski. Neutrinos from particle decay in the Sun and Earth. *Physical Review D*, 51(2):328–340, January 1995.

[45] Marc Kamionkowski. Energetic neutrinos from heavy-neutralino annihilation in the Sun. *Physical Review D*, 44(10):3021–3042, November 1991.

[46] E.W. Kolb and M.S. Turner. *The Early Universe*. Frontiers in Physics. Addison-Wesley Longman, Incorporated, 1990.

[47] Joachim Kopp. Constraints on dark matter annihilation from AMS-02 results. *Physical Review D*, 88(7):076013, October 2013.

[48] Chris Kouvaris and Peter Tinyakov. Constraining asymmetric dark matter through observations of compact stars. *Physical Review D*, 83(8):083512, April 2011.

[49] L. M. Krauss, K. Freese, D. N. Spergel, and W. H. Press. Cold dark matter candidates and the solar neutrino problem. *The Astrophysical Journal*, 299:1001, December 1985.

[50] Michael Kuhlen, Mark Vogelsberger, and Raul Angulo. Numerical simulations of the dark universe: State of the art and the next decade. *Physics of the Dark Universe*, 1(1-2):50–93, November 2012.

[51] J.D. Lewin and P.F. Smith. Review of mathematics, numerical factors, and corrections for dark matter experiments based on elastic nuclear recoil. *Astroparticle Physics*, 6(1):87–112, December 1996.

[52] FS Ling, E Nezri, E Athanassoula, and R Teyssier. Dark matter direct detection signals inferred from a cosmological N-body simulation with baryons. *Journal of Cosmology and Astroparticle Physics*, 2010(02):012–012, February 2010.

[53] J. E. Littleton, H. M. van Horn, and H. L. Helfer. Processes of Energy Transport by Longitudinal Waves and the Problem of Solar Neutrinos. *The Astrophysical Journal*, 173:677, May 1972.

[54] RUPAK MAHAPATRA. Review of dark matter direct detection experiments. *Pramana*, 79(5):1045–1057, November 2012.

[55] R.A. Meyers and S.N. Shore. *Encyclopedia of astronomy and astrophysics*. Academic Press, 1989.

[56] E Nezri. Indirect Detection of Neutralino Dark Matter with Neutrino Telescopes 1 . (November):1–9, 2002.

[57] Shmuel Nussinov, Lian-tao Wang, and Itay Yavin. Capture of inelastic Dark Matter in the sun. *Journal of Cosmology and Astroparticle Physics*, 2009(08):037–037, August 2009.

[58] Keith A Olive and Mark Srednicki. Solar neutrino searches and cold dark matter. *Physics Letters B*, 205(4):553–558, May 1988.

[59] a. Ozawa, T. Suzuki, and I. Tanihata. Nuclear size and related topics. *Nuclear Physics A*, 693(1-2):32–62, October 2001.

[60] A. A. Penzias and R. W. Wilson. A Measurement of Excess Antenna Temperature at 4080 Mc/s. *The Astrophysical Journal*, 142:419, July 1965.

[61] M.E. Peskin and D.V. Schroeder. *An Introduction to Quantum Field Theory*. Advanced book classics. Addison-Wesley Publishing Company, 1995.

[62] KALLIOPI PETRAKI and RAYMOND R. VOLKAS. REVIEW OF ASYMMETRIC DARK MATTER. *International Journal of Modern Physics A*, 28(19):1330028, July 2013.

[63] WH Press and DN Spergel. Capture by the sun of a galactic population of weakly interacting, massive particles. *The Astrophysical Journal*, 296:679, September 1985.

[64] JR Primack. Dark matter and structure formation. *Formation of Structure in the Universe*, 1999.

[65] Vera C. Rubin and Jr. Ford, W. Kent. Rotation of the Andromeda Nebula from a Spectroscopic Survey of Emission Regions. *The Astrophysical Journal*, 159:379, February 1970.

[66] T Saab. An Introduction to Dark Matter Direct Detection Searches & Techniques. pages 1–28, 2012.

[67] Pierre Salati. Indirect and direct dark matter detection. *PoS*, CARGESE200:009, 2007.

[68] Kris Sigurdson, Michael Doran, Andriy Kurylov, Robert Caldwell, and Marc Kamionkowski. Dark-matter electric and magnetic dipole moments. *Physical Review D*, 70(8):083501, October 2004.

[69] Joseph Silk, Keith Olive, and Mark Srednicki. The photino, the sun, and high-energy neutrinos. *Physical Review Letters*, 55(2):257–259, July 1985.

[70] T. et al. (Super-K Collaboration) Tanaka. AN INDIRECT SEARCH FOR WEAKLY INTERACTING MASSIVE PARTICLES IN THE SUN USING 3109.6 DAYS OF UPWARD-GOING MUONS IN SUPER-KAMIOKANDE. *The Astrophysical Journal*, 742(2):78, December 2011.

[71] Y Totsuka. First Results from Super-Kamiokande. *Eighteenth Texas Symposium on Relativistic ...*, (February 1987):1–10, 1998.

[72] Neal Weiner and Itay Yavin. UV completions of magnetic inelastic and Rayleigh dark matter for the Fermi Line(s). *Physical Review D*, 87(2):023523, January 2013.

[73] Christoph Weniger. A tentative gamma-ray line from Dark Matter annihilation at the Fermi Large Area Telescope. *Journal of Cosmology and Astroparticle Physics*, 2012(08):007–007, August 2012.

[74] Henry T Wong. Low Energy Neutrino and Dark Matter Physics with sub-keV Germanium Detectors. *Journal of Physics: Conference Series*, 309:012024, August 2011.

[75] S.S.M. Wong. *Introductory Nuclear Physics*. A Wiley-Interscience publication. Wiley, 1998.

[76] V Zacek. Dark matter. *arXiv preprint: 0707.0472v1*, pages 1–39, 2007.

[77] Erik Zackrisson. Introduction to Dark Matter. *Thesis - Uppsala University*, 2005.

[78] A. Zee. *Quantum Field Theory in a Nutshell: (Second Edition)*. In a Nutshell. Princeton University Press, 2010.

[79] F Zwicky. *Helvetica Physica Acta*, 6:110–127, 1933.